Characteristics of grid turbulence and turbulence modulation after interacting with a shock wave

Takuya KITAMURA

Department of Mechanical Science and Engineering

Nagoya University

A thesis submitted for the degree of

Doctor of Engineering

Acknowledgements

I would like to record here my gratitude to Prof. Yasuhiko Sakai, Prof. Koji Nagata, Prof. Akihiro Sasoh, Associate Prof. Yasumasa Ito and Associate Prof. Takashi Ishihara.

Prof. Sakai guides my work from wide range of views. His marvelous education and attitude for turbulence study impressed me significantly and directed my way. It was of my great pleasure and privilege to work for him.

Without Prof. Nagata, this work could not be accomplished. I deeply appreciate him for his guidance and encouragement. He is magnanimous and I would like to be a person like him in the future.

Prof. Sasoh gave me valuable advice on shock wave study. I deeply respect his talents and attitude toward researches. I also would like to thank him for reviewing this PhD thesis.

Kind advice by associate Prof. Ito was so precious to me. I could have good times particularly through discussion about turbulence at dinner. Also various experiences I shared with him are irreplaceable.

I would like to thank Associate Prof. Ishihara for reviewing this PhD thesis.

I would like to thank Assistant Prof. Koji Iwano who gave me various advices. He was also so precious to me.

Other people are also greatly appreciated. I am grateful for Mr. Takagi, Mr. Harasaki, Mr. Saito, Mr. Takeuchi and Mr. Konishi for their kind help in experiments, and I also would like to thank to all the members of the statistical fluid engineering laboratory at Nagoya University.

In addition, this work was executed under the Leading Graduate School program, Nagoya University.

I would like to note that the great works by Drs. G. K. Batchelor, P. G. Saffman, J. R. Kraichnan and a lot of researchers inspired me. I would like to be a theorist like them who impresses researchers in the future.

I would like to thank my friends, Mr. Okazaki (Nagasaki Seiryo high school) and Mr. Hashiguchi (Yakitori Hide). They had positive and significant impacts on my life. At last, I dearly would like to appreciate my father, Shigeru, my mother, Ayako, my sister, Hiroko and my brother, Wataru.

Contents

Chapter 1

Introduction

1.1 Background

Our understanding for turbulent flows remains minimal even though these equations were written down in the 19th Century. Turbulence is a complex, nonlinear multiscale phenomenon far from equilibrium and is described in terms of its ability to transfer energy among various scales. This nonlinearity arizes randomness and complexity of turbulent flows and they make the analysis of the system difficult. However, such randomness may permit us to treat the system statistically. Therefore, the derivation of the statistical theory of turbulence from the first principle such as Navier-Stokes equation is the main challenge in fluid mechanics. Renowned physicist Richard Feynman described turbulence as "the most important unsolved problem of classical physics". In fact, the progress in construction of turbulence theory seems limited compared with the progresses in the quark theory, which deals with the submicroscopic world and with that in the big-bang theory, which deals with the formation of the universe. It is due to turbulence nature: strong nonlinearity, non-equilibrium, irreversibility and a lot of freedom of degrees. Turbulence is also known as a ubiquitous phenomenon that we can see around us; for example, smoke of cigarette, external flows over all kind of vehicles such as cars, airplanes and ships, atmospheric flows at planets and universe. Thus, it is important to understand turbulent phenomena from the engineering perspective.

1.1.1 Characteristics of grid turbulence

Taylor (1935) introduced the concept of isotropic turbulence. Subsequently, the various statistical theory of turbulence have been proposed. On the other hand, in many practical engineering devices, turbulent flows are inhomogeneous and anisotropic. However, there is a possibility that small scale structures behave like isotropic and and are governed by the inherent Navier-Stokes dynamics far from the boudary condition, regardless of large scale inhomogeneity and anistropy (Kolmogorov, 1941a,b). Thus, a lot of experimental and numerical studies on isotropic turbulence have been performed to confirm the validity of theory of Kolmogorov (1941a,b). In experiments, the grid turbulence is close to homogeneous isotropic turbulence, and therefore a lot of studies have been carried out (Antonia *et al.*, 2003; Batchelor & Townsend, 1948a,b; Comte-Bellot & Corrsin, 1966; Lavoie *et al.*, 2007; Mohamedo & LaRue, 1990; Simmons & Salter, 1934). The main purpose to study grid turbulence was to investigate the small scale structures (Makita, 1991; Mydlarski & Warhaft, 1996) and large scale structures related to the decay law of turbulence kinetic energy (TKE) (Batchelor & Townsend, 1948a,b; Comte-Bellot & Corrsin, 1966; Lavoie *et al.*, 2007; Mohamedo & LaRue, 1990). As to the small scale structures, the experimental results (Makita, 1991; Mydlarski & Warhaft, 1996) and numerical results (Kaneda *et al.*, 2003) revealed that the energy spectrum in the inertial subrange is close to the Kolmogorov's -5/3 law. On the other hand, as to the large scale structures, Ishida *et al.* (2006) showed that the TKE decay law is close to the Kolmogorov's -10/7 law for homogeneous isotropic turbulence. Its decay law is believed to be related to the large scale structures, i.e. an initial energy spectrum at low wavenumbers $E(k \to 0) \sim k^m$, where k is the wavenumber (Batchelor, 1953; Davidson, 2004; Hinze, 1959; Sagaut & Cambon, 2008). Numerical simulations of homogeneous isotropic turbulence with the various initial energy spectra showed that the TKE decay law depends on the form of energy spectrum at low wavenumbers. However, little is known about the energy spectrum at low wavenumbers in a real homogeneous isotropic turbulent field such as grid turbulence. In other words, there are only a few experimental studies that investigate existence of invariants

related to the large scale in spite of the fact that the TKE decay law of grid turbulence is one of fundamental and important problems in turbulence.

1.1.2 Turbulence-shock wave interaction

In addition, turbulence-shock wave interaction is interesting from an engineering perspective. It is an important assignment in the aerospace engineering and space physics. For example, demand of the next generation supersonic transport (SST) has been increasing nowadays because of the rapid the globalization in various fields. To develop new SST, one of the primary issue that we have to overcome is the sonic boom problem. It is known that the deformation of pressure waveform of sonic boom is mainly affected by atmospheric turbulence. However, the effect of turbulence is not incorporated into the design of SST. Similarly, the effect of the shock wave is of interest from a physical perspective. Thus, as a fundamental research, it is important to investigate quantitatively how much a shock wave is modified by turbulence and vice versa. In this study, we focused on the propagating process of sonic boom, i.e. turbulence-shock wave interaction. The main purpose is to clarify the fundamental mechanism with respect to turbulence-shock wave interaction.

1.1.2.1 Experimental studies on turbulence-shock wave interaction

Keller & Merzkirch (1990) conducted experiments on the interaction between compressible grid turbulence and a reflected shock wave, and measured density fluctuations using the speckle method. They showed that the streamwise integral length scale and Taylor microscale of density fluctuations are amplified after the interaction. Honkan & Andreopoulos (1992) conducted shock-tube experiments and showed that the streamwise root mean square (r.m.s) velocity was amplified and that the energy at large scales (rather than that at small scales) was amplified; the turbulence dissipation scale was also increased. On the other hand, Briassulis *et al.* (1996) showed that the eddies are significantly compressed in the streamwise direction, whereas their extent in the transverse direction remains similar for weak interactions; the eddies are compressed in both directions for strong interactions. Agui *et al.* (2005) conducted experiments on grid turbulence

and a moving shock wave in a large shock tube facility. They investigated the statistical quantities related to vorticity using a vorticity probe and showed that the vorticity components perpendicular to the shock wavefront increase and that the streamwise integral length scale decreases after the interaction. Regarding the TKE dissipation rate, they found that the solenoidal dissipation occupies more than the dilatational dissipation throughout the interaction, and that the TKE dissipation rate was amplified after the interaction. Barre *et al.* (1996) conducted experiments on the interaction between Mach 3 quasi-isotropic turbulence and a standing shock wave, and showed that the amplification of the variance of the streamwise velocity fluctuation, the strong anisotropy behind a shock wave, and the decrease in the streamwise integral length scales by up to 1/7 after the interaction.

Thus, although all previous studies showed the amplification of TKE after the interaction with a shock wave, the question as to whether the turbulence characteristic scale increases or decreases remains unsolved because there is little agreement in previous studies. Furthermore, these studies focus on the highly compressible turbulence, and therefore it is important to study the interaction between divergence-free grid turbulence and a shock wave. For instance, the previous studies investigated turbulence flows with $M_U \gg 0.3$, where M_U is the Mach number based on the upstream mean velocity (Agui *et al.*, 2005). Thus, there is a possibility that the changes in turbulence depend on the flow properties as mentioned by Yoshizawa (1993). To the best of my knowledge, there is no study on the changes in divergence-free turbulence interacting with a shock wave. The present originality is in the first experiment on the low-Mach number grid turbulence interacting with a shock wave.

1.1.2.2 Numerical and theoretical studies on turbulence-shock wave interaction

Direct Numerical Simulations (DNSs) on the interaction between homogeneous isotropic turbulence and a standing shock wave have been conducted to deepen the fundamental understanding of these phenomena. Using DNS, Lee *et al.* (1993) and Hannappel & Friedrich (1995) showed that all turbulence characteristic lengths (i.e. longitudinal and lateral velocity integral length scale, longitudinal

and lateral velocity Taylor microscale, dissipation length scale, and the integral length scales and Taylor microscales of density fluctuations) are decreased after the interaction. Lee *et al.* (1997) showed that the turbulence dissipation scale is increased after interaction with a strong shock wave. Mahesh *et al.* (1997) showed that upstream entropy fluctuations and the velocity-temperature correlation have a strong influence on the turbulence evolution across a shock wave. They also found higher amplifications of TKE and enstrophy when the upstream turbulence has a negative velocity–temperature correlation, whereas the amplifications are lower when the upstream turbulence has a positive velocity-temperature correlation. Lee *et al.* (1993) and Donzis (2012) suggested different criteria for the structure characterized by 'broken' or 'wrinkled' shock regimes. Lee *et al.* (1993) suggested $M_t^2/\left(M_s^2-1\right)$ as the criterion that is valid when the pressure fluctuations driven by turbulence in the upstream region is larger than the pressure jump due to the shock wave. On the other hand, Donzis (2012) suggested $M_t/\left(\sqrt{Re_\lambda}\left(M_s-1\right)\right)$ as the criterion based on the dimensional and similarity analyses. However, his criterion is in contrast to linear interaction approximation (LIA) since the fluctuations must be weak in the assumption of LIA (Larsson *et al.*, 2013; Sagaut & Cambon, 2008). Instead of these criteria, Larsson & Lele (2009) and Larsson *et al.* (2013) showed that the criterion for the 'wrinkled' and 'broken' shock regimes is well characterized by $M_t/\left(M_s-1\right)$. One important consequence of the effect of M_t is that a shock wave tends to be broken with an increase of $M_t/\left(M_s-1\right)$ (Larsson & Lele, 2009; Larsson *et al.*, 2013). Larsson & Lele (2009) showed that the amplification of vorticity fluctuations strongly depends on the grid resolution. Larsson *et al.* (2013) also showed that the evolution of TKE is damped and that TKE evolves to have a peak located at $0.8L_\epsilon$ behind a shock wave, where L_ϵ is the dissipation length scale. Grube *et al.* (2011) showed that the evolution of TKE is approximately monotonic without damping and that the compressible contribution is much larger than other contributions for the transverse vorticity variance budget.

In theoretical studies of the amplification of velocity fluctuations when interacting with a shock wave, there are two main methods: LIA and rapid distortion theory (RDT). Lee *et al.* (1993) showed that the Taylor microscale is decreased after interaction with a shock wave using LIA. On the other hand, RDT is a

valid method in the case of rapid distortion of turbulent structures such as interaction with a shock wave. In RDT theory, either Cartesian coordinates or Craya-Herring coordinates is used. The former is able to compare the results directly with experiments and DNS. The latter is convenient for interpretation and is easy to calculate. Jacquin *et al.* (1993) conducted Craya-Herring decomposition into dilatational mode and solenoidal mode for a compressible Navier–Stokes equation. They showed that turbulence is amplified when compressed in a one-dimensional direction. On the other hand, Mahesh *et al.* (1994) conducted RDT numerically for Cartesian coordinates. However, they did not find the analytical solution. Furthermore, they did not obtain significant changes in the turbulence characteristic length scales.

1.2 Research purpose of this thesis

Purpose of study in this thesis is to clarify characteristics of grid turbulence and changes in turbulence after interacting with a shock wave. Before performing the experiments of turbulence-shock wave interaction, it is necessary to investigate the fundamental characteristics of grid turbulence. With regard to grid turbulence, TKE decay law is one of unsolved problems in turbulence over half a century as mentioned above. Inspired by the previous work by Krogstad & Davidson (2010), the TKE decay law and invariants were investigated for five mesh sizes in moderate Reynolds number flows. After confirming the characteristics of the grid turbulence, we carried out experiments on turbulence interacting with a shock wave and discuss the changes in turbulence after interacting with a shock wave. The purpose of this experiment is to clarify peculiar phenomenon on the interaction between divergence-free grid turbulence and the shock wave. However, in the present experiment, a spherical shock wave follows an expansion fan and therefore it is difficult to understand pure interaction between turbulence and a planar shock wave since there are additional effects on changes in turbulence due to the expansion fan. To begin with, there are a lot of open questions with regard to turbulence-shock wave interaction (Andreopoulos *et al.*, 2000). To deepen the mechanism of the interaction, the rapid distortion theory (RDT) was carried out. This theoretical approach allows us to answer the questions identified by

Andreopoulos *et al.* (2000). The purpose of this theoretical approach is to clarify the changes in turbulence after the interaction within the framework of linear theory.

1.3 Outline of this thesis

Chapter 1, this section, gives introduction and purpose. Chapter 2 briefly describes important theories in isotropic turbulence and brief explanation about RDT for the sake of later discussion. Chapter 3 describes experimental results on characteristics of grid turbulence (the TKE decay law, invariants and so forth) at moderate Reynolds number flows. Chapter 4 describes experimental results on characteristics of divergence-free grid turbulence interacting with a weak shock wave under various Reynolds numbers based on Taylor microscale. Chapter 5 describes RDT results for turbulence-shock wave interaction. Chapter 6 describes brief conlusion of this study.

Chapter 2

Statistical theory of turbulence : Brief introduction

2.1 Equations of motion of a fluid

2.1.1 Equation of continuity

The equation of continuity is

$$\frac{\partial \rho}{\partial t} + \mathrm{div}\,(\rho \boldsymbol{u}) = \frac{D\rho}{Dt} + \rho \mathrm{div} \boldsymbol{u} = 0, \tag{2.1}$$

where ρ is the fluid density, $\boldsymbol{u}$ is velocity and $D/Dt = \partial/\partial t + \boldsymbol{u} \cdot \nabla$ is material derivative, which allows us to relate the Eulerian and Lagrangian time derivatives of a dependent variable. For an incompressible fluid, $D\rho/Dt = 0$. and we then have

$$\frac{\partial u_i}{\partial x_i} = 0. \tag{2.2}$$

2.1.2 Momentum equation

The Cauchy momentum equation is a vector partial differential equation that describes the non-relativistic momentum transport in any continuum. It is written by

$$\rho \frac{Du_i}{Dt} = -\frac{\partial p}{\partial x_i} + \frac{\partial \tau_{ij}}{\partial x_j} + F_i \tag{2.3}$$

where p is the pressure, $\boldsymbol{\tau}$ is the viscous stress tensor, $\boldsymbol{F}$ is the body force per unit volume. When the stress tensor has a linear relation with the velocity gradient, the stress tensor can be written as

$$\tau_{ij} = C_{ijkl} A_{kl} = C_{ijkl} \frac{\partial u_k}{\partial x_l}, \tag{2.4}$$

where C_{ijkl} is the fourth-order tensor determined from the matter. Taking account of the fact that the velocity gradient can be decomposed into the symmetrical part $\boldsymbol{S}$ and anti–symmetrical part $-\frac{1}{2}\epsilon_{klm}\omega_m$, τ_{ij} can be written as

$$\tau_{ij} = C_{ijkl} S_{kl} - \frac{1}{2} C_{ijkl} \epsilon_{klm} \omega_m, \tag{2.5}$$

where ϵ_{ijk} is the Levi-Civita tensor and $\boldsymbol{\omega}$ is the vorticity. When the molecular structure of the fluid is statistically isotropic, the fourth–order tensor takes a simple form as follows (Batchelor, 1967):

$$C_{ijkl} = \mu \delta_{ik} \delta_{jl} + \mu' \delta_{ij} \delta_{kl} + \mu'' \delta_{il} \delta_{jk}, \tag{2.6}$$

where μ, μ' and μ'' are the scalar functions. δ_{ij} is the Kronecker delta. Using the symmetry of $\boldsymbol{S}$ with respect to the subscripts i and j, we then obtain $\mu'' = \mu$.

$$\tau_{ij} = 2\mu S_{ij} + \mu' S_{kk} \delta_{ij}. \tag{2.7}$$

Taking accont of the fact that the trace of the strain tensor in three dimensions is $S_{ii} = \mathrm{div}\boldsymbol{u}$, the trace of the stress tensor in three dimensions becomes

$$\tau_{ii} = (3\mu' + 2\mu) S_{ii}.$$

Decomposing the stress tensor into isotropic and deviatoric parts, τ_{ij} is given by

$$\tau_{ij} = \left(\mu' + \frac{2}{3}\mu\right) S_{kk} \delta_{ij} + 2\mu S_{ij} - \frac{2}{3}\mu S_{kk} \delta_{ij}.$$

Introducing the second viscosity $\zeta \left(= \mu' + \frac{2}{3}\mu\right)$, stress tensor is given by

$$\tau_{ij} = 2\mu S_{ij} + \left(\zeta - \frac{2}{3}\mu\right) S_{kk} \delta_{ij}. \tag{2.8}$$

Here, the second viscosity vanishes for monatomic gases. In such case, the fluid is said to be Stokesian with

$$\tau_{ij} = 2\mu \left(S_{ij} - \frac{1}{3} S_{kk} \delta_{ij} \right). \tag{2.9}$$

When the variation of μ is neglected, the momentum equation now becomes

$$\frac{D\boldsymbol{u}}{Dt} = -\frac{1}{\rho}\nabla p + \nu \left[\nabla^2 \boldsymbol{u} + \frac{1}{3}\nabla \left(\mathrm{div}\boldsymbol{u} \right) \right] + \frac{\boldsymbol{F}}{\rho}, \tag{2.10}$$

where $\nu = \mu/\rho$ is the kinematic viscosity. For an incompressible fluid, momentum equation is written by

$$\frac{D\boldsymbol{u}}{Dt} = -\frac{1}{\rho}\nabla p + \nu \nabla^2 \boldsymbol{u} + \frac{\boldsymbol{F}}{\rho}. \tag{2.11}$$

2.2 Homogeneous turbulence

2.2.1 Statistical description of homogeneous turbulence

We consider the correlation of the physical quantities $a\left(\boldsymbol{x}\right)$, $b\left(\boldsymbol{x}'\right)$, $c\left(\boldsymbol{x}''\right), \ldots$ at the locations $\boldsymbol{x}$, $\boldsymbol{x}'$, $\boldsymbol{x}'' \ldots$, namely,

$$A\left(\boldsymbol{x}, \boldsymbol{x}', \boldsymbol{x}'', \ldots\right) = \left\langle a\left(\boldsymbol{x}\right) b\left(\boldsymbol{x}'\right) c\left(\boldsymbol{x}''\right) \cdots \right\rangle \tag{2.12}$$

Homogeneous turbulence is a turbulence whose correlations are statistically invariant under arbitrary translation at every point in space. In other words, when following equation is satisfied, turbulent field is statistically homogeneous.

$$A\left(\boldsymbol{x} + \boldsymbol{r}, \boldsymbol{x}' + \boldsymbol{r}, \boldsymbol{x}'' + \boldsymbol{r}, \ldots\right) = A\left(\boldsymbol{x}, \boldsymbol{x}', \boldsymbol{x}'', \ldots\right) \tag{2.13}$$

Turbulent field is homogeneous for the direction $\boldsymbol{e}$, when above equation is satisfied in the direction $\boldsymbol{e}$. In fully developed region of grid turbulence, turbulent field is close to homogeneous in the transverse directions.

2.2.2 Statistical description of isotropic turbulence

If the statistics are rotationally invariant in addition to the homogeneity, the field is called isotropic. When a velocity field is isotropic, tensors become a relatively simple form. The general form of an isotropic tensor, such as being dependent on the relative position of two points, $\boldsymbol{r} = \boldsymbol{x}' - \boldsymbol{x}$, was suggested by Robertson. (1940). The two-point 1st, 2nd and 3rd isotropic tensors which satisfy reflection symmetry are given by

$$Q_i(\boldsymbol{r}) = A^{(1)} r_i, \tag{2.14a}$$

$$Q_{ij}(\boldsymbol{r}) = A^{(2)} r_i r_j + B^{(2)} \delta_{ij}, \tag{2.14b}$$

$$Q_{ijk}(\boldsymbol{r}) = A^{(3)} r_i r_j r_k + B^{(3)} r_i \delta_{jk} + C^{(3)} r_j \delta_{ki} + D^{(3)} r_k \delta_{ij}, \tag{2.14c}$$

where the scalar coefficients $A^{(1)} \sim D^{(3)}$ are all even function of r [1].

Using (2.14a)-(2.14c), we obtain a two-point velocity correlation equation called 'Karman-Howarth equation' for the incompressible isotropic turbulence (Karman & Howarth, 1938) :

$$\frac{\partial}{\partial t}\left\langle \boldsymbol{u}\cdot\boldsymbol{u}'\right\rangle = \frac{1}{r^2}\frac{\partial}{\partial r}\frac{1}{r}\frac{\partial}{\partial r}\left(u^3 r^4 K(r)\right) + 2\nu\nabla^2\left\langle \boldsymbol{u}\cdot\boldsymbol{u}'\right\rangle, \tag{2.15}$$

where $u^3 K(r) = \left\langle u_1^2(\boldsymbol{x})\, u_1(\boldsymbol{x}')\right\rangle$ and $u = \sqrt{\langle \boldsymbol{u}^2\rangle}$. Here, $\langle \boldsymbol{u}\cdot\boldsymbol{u}'\rangle$ is given by

$$\left\langle \boldsymbol{u}\cdot\boldsymbol{u}'\right\rangle = \frac{u^2}{r^2}\frac{\partial\left(r^3 f(r)\right)}{\partial r}, \tag{2.16}$$

where $f(r)$ is the longitudinal correlation function. Here the pressure term is omitted because the correlation between velocity and pressure is zero for incompressible isotropic turbulence, meanwhile it is not zero for compressible isotropic turbulence. In incompressible isotropic turbulence, $g(r) = f(r) + \frac{1}{2} r \frac{\partial f(r)}{\partial r}$ holds

[1] For the exact sense, the general isotropic tensors are given by $Q_i(\boldsymbol{r}) = A^{(1)} r_i$, $Q_{ij}(\boldsymbol{r}) = A^{(2)} r_i r_j + B^{(2)}\delta_{ij} + C^{(2)}\epsilon_{ijk} r_k$, $Q_{ijk}(\boldsymbol{r}) = A^{(3)} r_i r_j r_k + B^{(3)} r_i \delta_{jk} + C^{(3)} r_j \delta_{ki} + D^{(3)} r_k \delta_{ij} + E^{(3)}\epsilon_{ijl} r_l r_k + F^{(3)}\epsilon_{jkl} r_l r_i + G^{(3)}\epsilon_{kil} r_l r_j + H^{(3)}\epsilon_{ijk}$. When helicity exists, we have to use these forms. However, we usually use the isotropic tensor which satisfies the reflection symmetry.

between the longitudinal correlation function $f(r)$ and the lateral correlation function $g(r)$. In terms of the structure functions, (2.15) can be written as

$$\frac{1}{2}\frac{\partial}{\partial t}\left\langle \Delta u_{\parallel}^{2}(r)\right\rangle +\frac{1}{6r^{4}}\frac{\partial}{\partial r}\left[r^{4}\left\langle \Delta u_{\parallel}(r)^{3}\right\rangle \right]-\frac{\nu}{r^{4}}\frac{\partial}{\partial r}\left[r^{4}\frac{\partial}{\partial r}\left\langle \Delta u_{\parallel}(r)^{2}\right\rangle \right]=-\frac{2}{3}\epsilon, \quad (2.17)$$

where $\Delta u_{\parallel}^{2}(r) = 2u^{2}(1-f(r))$, $\Delta u_{\parallel}^{3}(r) = 6u^{3}K(r)$ and ϵ is the turbulence kinetic energy (TKE) dissipation rate.

2.3 Fourier representation of turbulence

2.3.1 Description of homogeneous turbulence in Fourier space

In here, we consider an incompressible fluid only. The Fourier transformed Navier Stokes equation (2.11) is written by

$$\begin{aligned}\left(\frac{\partial}{\partial t}+\nu k^{2}\right)\hat{u}_{i}(\boldsymbol{k},t) &= -\imath k_{j}P_{il}(\boldsymbol{k})\int_{\boldsymbol{p}+\boldsymbol{q}=\boldsymbol{k}}\hat{u}_{l}(\boldsymbol{p},t)\,\hat{u}_{j}(\boldsymbol{q},t)\,d\boldsymbol{p}\\ &= M_{ijl}(\boldsymbol{k})\int_{\boldsymbol{p}+\boldsymbol{q}=\boldsymbol{k}}\hat{u}_{l}(\boldsymbol{p},t)\,\hat{u}_{j}(\boldsymbol{q},t)\,d\boldsymbol{p},\end{aligned} \quad (2.18)$$

where $\imath=\sqrt{-1}$ and

$$M_{ijl}(\boldsymbol{k}) = -\frac{\imath}{2}\left(k_{l}P_{ij}(\boldsymbol{k})+k_{j}P_{il}(\boldsymbol{k})\right), P_{ij}(\boldsymbol{k}) = \delta_{ij}-\frac{k_{i}k_{j}}{k^{2}}. \quad (2.19)$$

After multiplying $\hat{u}_{i}^{*}(\boldsymbol{k},t)$ to (2.18) and taking the average, we have

$$\begin{aligned}\left(\frac{\partial}{\partial t}+2\nu k^{2}\right)\left\langle \hat{u}_{i}(\boldsymbol{k},t)\,\hat{u}_{i}^{*}(\boldsymbol{k},t)\right\rangle &= M_{ijl}(\boldsymbol{k})\iint d\boldsymbol{p}d\boldsymbol{q}\delta(\boldsymbol{k}-\boldsymbol{p}-\boldsymbol{q})\left[\left\langle \hat{u}_{i}(-\boldsymbol{k},t)\,\hat{u}_{j}(\boldsymbol{p},t)\,\hat{u}_{l}(\boldsymbol{q},t)\right\rangle \right.\\ &\quad \left.-\left\langle \hat{u}_{i}(\boldsymbol{k},t)\,\hat{u}_{j}(\boldsymbol{p},t)\,\hat{u}_{l}(\boldsymbol{q},t)\right\rangle \right]\\ &= \iint d\boldsymbol{p}d\boldsymbol{q}\;S(\boldsymbol{k},\boldsymbol{p},\boldsymbol{q},t),\end{aligned} \quad (2.20)$$

where

$$S(\boldsymbol{k},\boldsymbol{p},\boldsymbol{q},t) = -2\Re\left[M_{ijl}(\boldsymbol{k})\left\langle \hat{u}_{i}(\boldsymbol{k},t)\,\hat{u}_{j}(\boldsymbol{p},t)\,\hat{u}_{l}(\boldsymbol{q},t)\right\rangle \delta(\boldsymbol{k}+\boldsymbol{p}+\boldsymbol{q})\right], \quad (2.21)$$

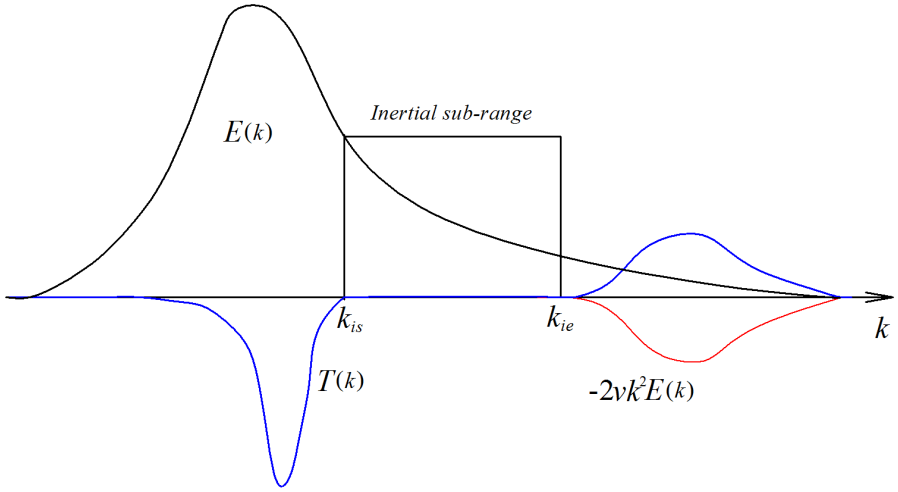

Figure 2.1: Schematic of $E(k)$ and $T(k)$.

where $\Re[\,]$ indicates the real part and $\delta(\boldsymbol{x})$ is the three-dimensional Dirac delta function. $S(\boldsymbol{k},\boldsymbol{p},\boldsymbol{q},t)$ satisfies $S(\boldsymbol{k},\boldsymbol{p},\boldsymbol{q},t)+S(\boldsymbol{p},\boldsymbol{q},\boldsymbol{k},t)+S(\boldsymbol{p},\boldsymbol{q},\boldsymbol{k},t)=0$ as a consequence of conservation of energy. After multiplying $2\pi k^2$, we have the Lin equation:

$$\left(\frac{\partial}{\partial t}+2\nu k^2\right)E(k,t)=T(k,t), \tag{2.22}$$

where $E(k,t)$ is the energy spectrum and $T(k,t)$ is the energy transfer function. Lin equation is the spectral equivalent of the Karman-Howarth equation. Schematic of $E(k)$ and $T(k)$ is shown in figure 2.1. $T(k)$ is negative for small k and positive for large k. This can be interpreted as removal of energy from large scales and deposition of energy at small scales. Integrating (2.22) from 0 to ∞, we have

$$\frac{d}{dt}\frac{\langle\boldsymbol{u}^2\rangle}{2}=-\epsilon, \tag{2.23}$$

where

$$\frac{\langle\boldsymbol{u}^2\rangle}{2}=\int_0^\infty dk\ E(k,t),\ \epsilon=2\nu\int_0^\infty dk\ k^2E(k,t),\ \int_0^\infty dk\ T(k,t)=0. \tag{2.24}$$

There are following relations between the physical space and Fourier space (Davidson, 2004):

- The relationship between $E(k)$ and $f(r)$

$$E(k) = \frac{u^2}{\pi} \int_0^\infty dr \, \frac{1}{r^2} \frac{\partial}{\partial r} \left(r^3 f(r) \right) kr \sin(kr) \tag{2.25}$$

$$u^2 f(r) = 2 \int_0^\infty \frac{E(k)}{k^2 r^2} \left(\frac{\sin kr}{kr} - \cos kr \right) dk \tag{2.26}$$

- The relationship between $T(k)$ and $K(r)$

$$T(k) = \frac{k}{\pi} \int_0^\infty dr \, \frac{1}{r} \frac{\partial}{\partial r} \frac{1}{r} \frac{\partial}{\partial r} \left[r^4 u^3 K(r) \right] \sin(kr) \tag{2.27}$$

$$K(r) = \frac{2r}{u^3} \int_0^\infty dk \, \frac{3(\sin(kr) - kr\cos(kr)) - (kr)^2 \sin(kr)}{(kr)^5} T(k) \tag{2.28}$$

2.4 Energy spectrum

In general, it is considered that energy spectrum can be divided into three ranges: the energy containing range, inertial subrange and dissipation range. A typical model spectrum to express these three ranges is given by

$$E(k) = K_0 \epsilon^{\frac{2}{3}} k^{-\frac{5}{3}} f_L(kL_{uu}) f_\eta(k\eta), \tag{2.29}$$

where K_0 is the Kolmogorov constant, L_{uu} is integral length scale and η is Kolmogorov scale. Here, $f_L(kL_{uu})$ and $f_\eta(k\eta)$ represent the energy spectra at the energy containing range and at the dissipation range, respectively. Kolmogorov's -5/3 law with wide wavenumber range has been observed in the local interstellar medium (Armstrong *et al.*, 1995), stratosphere (Nastrom & Gage, 1985) and various high Reynolds number flows as confirmed by a lot of experiments and numerical simulations. The following subsections briefly describe our agreements on energy spectrum over three ranges.

2.4.1 Energy spectrum at low wavenumbers

When equation (2.25) is expanded in series by Taylor expansion at $k = 0$, we have

$$E(k \to 0) = \frac{L}{4\pi^2} k^2 + \frac{I}{24\pi^2} k^4 + \cdots, \tag{2.30}$$

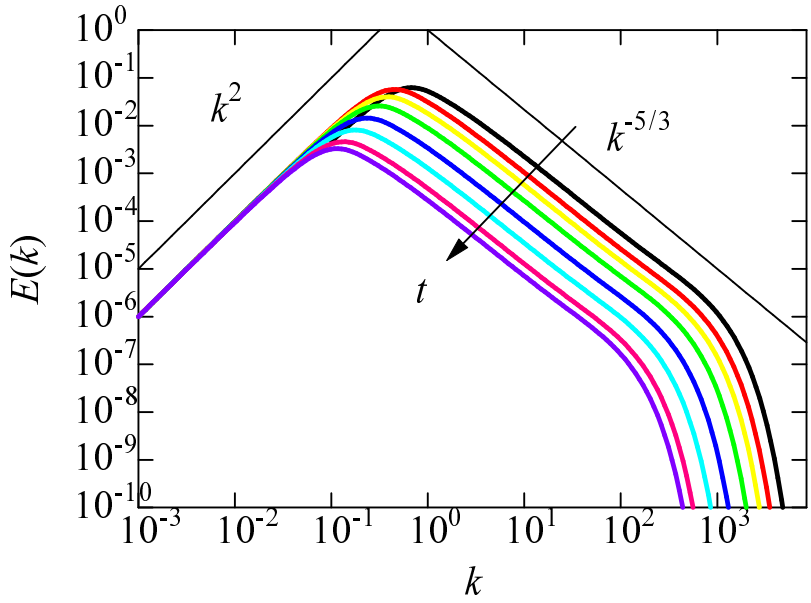

Figure 2.2: Time evolution of the energy spectrum by eddy damped quasi-normal Markovianization. The initial energy spectrum is given by Saffman type energy spectrum.

where L is called Saffman's integral and is

$$L = \int d\boldsymbol{r} \ \langle \boldsymbol{u} \cdot \boldsymbol{u}' \rangle \,, \tag{2.31}$$

while I is called Loitsianskii's integral and is

$$I = -\int d\boldsymbol{r} \ \boldsymbol{r}^2 \langle \boldsymbol{u} \cdot \boldsymbol{u}' \rangle \,. \tag{2.32}$$

These variables are known as invariants. The time evolution of the energy spectrum by eddy damped quasi-normal Markovianization (EDQNM) is shown in figure 2.2. It is clear from figure 2.2 that L is an invariant throughout the time evolution. However, there are a lot of open questions and problems as to Loitsianskii's integral I.

2.4.1.1 Loitsianskii's integral

Using (2.16) and integrating (2.15) over $r = 0$ to ∞, we have (Karman & Howarth, 1938)

$$\frac{d}{dt}\left[u^2\int_0^\infty r^4 f(r,t)\,dr\right] = \left[u^3 r^4 K(r)\right]_\infty + 2\nu\left[u^2 r^4 \frac{\partial}{\partial r} f(r)\right]_\infty, \tag{2.33}$$

where subscript ∞ denotes the limiting value of $r \to \infty$. Loitsianskii (1939) assumed that, for large r, the velocity at $\boldsymbol{x} + r\hat{\boldsymbol{e}}_1$ is statistically independent of the velocity at $\boldsymbol{x}$ in the sense that both $f(r)$ and $K(r)$ decay exponentially. Then, the right hand side of (2.33) becomes zero, and therefore, Loitsianskii's integral becomes invariant (Loitsianskii, 1939):

$$I = -\int \boldsymbol{r}^2 \langle \boldsymbol{u}\cdot\boldsymbol{u}'\rangle\, d\boldsymbol{r} = 8\pi u^2 \int_0^\infty r^4 f(r)\,dr = const. \tag{2.34}$$

Landau & Lifshitz (1959) showed that Loitsianskii's integral refers to the conservation of angular momentum by hypothesizing that $f(r)$ and $K(r)$ decay rapidly for large r and that the global linear momentum in a large control volume V is zero. Thus,

$$I = -\int \boldsymbol{r}^2 \langle \boldsymbol{u}\cdot\boldsymbol{u}'\rangle\, d\boldsymbol{r} = \frac{\langle \boldsymbol{H}^2\rangle}{V} = const. \tag{2.35}$$

Here, $\boldsymbol{H} = \int (\boldsymbol{x}\times\boldsymbol{u})\,dV$ is the global angular momentum for large V. Note that the Saffman type energy spectrum is not considered beforehand because of the assumption that the global linear momentum is zero (Loitsianskii, 1939).

Kolmogorov (1941c) predicted that the decay exponent of isotropic turbulence becomes 10/7 under the following three assumptions:

1. TKE decays according to $\frac{du^2}{dt} = -A\frac{u^3}{L_{uu}}$, where A is a constant.
2. Large-scale motions evolve in a self-similar manner when r is normalised by L_{uu}.
3. Loitsianskii's integral is constant and independent of time.

Using assumptions (2) and (3), we observe that the constancy of Loitsianskii's integral is equivalent to that of $u_{r.m.s}^2 L_{uu}^5$:

$$I = 8\pi u^2 \int_0^\infty r^4 f\left(\frac{r}{L_{uu}}\right) dr = 8\pi u^2 L_{uu}^5 \int_0^\infty \xi^4 f(\xi)\,d\xi = \alpha u^2 L_{uu}^5, \tag{2.36}$$

where α is a constant. The first assumption (1) has been confirmed by experiments (Pearson *et al.*, 2002) and numerical simulations (Kaneda *et al.*, 2003). When the above three assumptions are satisfied, the time evolutions of the TKE and integral length scale are given by $u^2 \sim t^{-\frac{10}{7}}$ and $L_{uu} \sim t^{\frac{2}{7}}$, respectively. However, the decay exponent of TKE for homogeneous isotropic turbulence is sometimes inconsistent with Kolmogorov's decay exponent. Proudman & Reid (1954) showed by the quasi-normalised theory that $\frac{d^2 I}{dt^2} > 0$, which implies that Loitsianskii's integral I is time-dependent [1]. Batchelor & Proudman (1956) pointed out that the difference between the results of Loitsianskii (1939) and Landau & Lifshitz (1959) and those of Proudman & Reid (1954) are arised from the effect of pressure. They showed that the pressure-velocity correlation is $\langle u_i u_j p' \rangle_\infty \sim r^{-3}$ for homogeneous anisotropic turbulence, because the pressure fluctuations at $\boldsymbol{x}' = \boldsymbol{x} + \boldsymbol{r}$, which arise from an eddy located at $\boldsymbol{x}$, have a relationship $p'_\infty \sim r^{-3}$. Thus, the triple velocity correlation is given by $\langle u_i u_j u'_k \rangle \sim C_{ijk} r^{-4}$. Here, the value of coefficient C_{ijk} has not been discussed in detail. Furthermore, Batchelor & Proudman (1956) have not validated this correlation for long ranges due to isotropy. Equation (2.33) implies that Loitsianskii's integral I is time-dependent if $u^3 K(r) \sim C r^{-4}$, i.e. Loitsianskii's integral I is not invariant. Thus, Kolmogorov's decay exponent 10/7 has been controversial. Here, C is an unknown coefficient. However, Ishida *et al.* (2006) showed by means of a DNS that Loitsianskii's integral I is an invariant in homogeneous isotropic turbulence. This implies that the coefficient $C = [r^4 K(r)]_\infty$ is very small. In addition, they showed that the decay exponent is 10/7. However, they set the initial energy spectrum as $E(k \to 0) \sim k^4$, in which Saffman's energy spectrum was not considered. Thus, what is shown in that Loitsianskii's integral becomes constant in homogeneous isotropic turbulence if the energy spectrum at low wavenumbers is $E(k \to 0) \sim k^4$. However, little is known about the energy spectrum at low

[1] In EDQNM, it is easily shown that (Lesieur & Schertzer, 1978)

$$T(k \to 0) = A k^4 - 2\nu_t k^2 E(k),$$

where ν_t is turbulent eddy viscosity and A is a constant. Thus, a time-varying Loitsianskii's integral is obtained in EDQNM and TKE decay law is different from Kolmogorov's -10/7 law.

wavenumbers in a real homogeneous quasi-isotropic turbulent field such as grid turbulence (Davidson, 2011).

2.4.1.2 Saffman's integral

For homogeneous isotropic turbulence, with the use of (3.4) and (2.16), Saffman's integral is given by

$$L = \int \langle \boldsymbol{u} \cdot \boldsymbol{u}' \rangle \, d\boldsymbol{r} = \int \frac{u^2}{r^2} \frac{\partial}{\partial r} \left(r^3 f\left(r\right) \right) d\boldsymbol{r} = 4\pi u^2 \left[r^3 f\left(r\right) \right]_\infty . \tag{2.37}$$

When $u^3 K\left(r\right)_\infty \sim r^{-4} + O\left(r^{-5}\right)$ for large r, we have

$$\frac{dL}{dt} = 4\pi \left[\frac{1}{r} \frac{\partial}{\partial r} \left(r^4 u^3 K\left(r\right) \right) \right]_\infty = 0. \tag{2.38}$$

Thus, L is an invariant. The characteristics of Saffman turbulence is that the autocorrelation for large r takes the form of $f\left(r \to \infty\right) \sim r^{-3}$, and large-scale eddies behave similar to dipoles. The physical interpretation of Saffman's integral was discussed by Saffman (1967) and Davidson (2004). L is expressed as

$$L = \frac{1}{V} \left\langle \left[\int_V \boldsymbol{u} dV \right]^2 \right\rangle = \frac{\left\langle \boldsymbol{P}^2 \right\rangle}{V}, \tag{2.39}$$

where V is a large control volume and the volume average is equal to the ensemble average, and $\boldsymbol{P}$ is the global linear momentum $\int_V \boldsymbol{u} dV$ in the large control volume V for homogeneous turbulence. The global angular momentum for the Saffman turbulence is expressed by the summation of the linear impulse $\boldsymbol{L}_i$ and angular momentum $\boldsymbol{H}_i$ of individual eddy (Davidson, 2004):

$$\boldsymbol{H} = \sum \boldsymbol{H}_i + \sum \boldsymbol{x}_i \times \boldsymbol{L}_i, \tag{2.40}$$

and the global linear momentum is expressed by

$$\boldsymbol{P} \sim \sum \boldsymbol{L}_i = \sum \frac{1}{2} \int_{V_i} \boldsymbol{x} \times \boldsymbol{\omega} dV, \tag{2.41}$$

where $\boldsymbol{H}_i = \frac{1}{3} \int_{V_i} \boldsymbol{r}_i \times \left(\boldsymbol{r}_i \times \boldsymbol{\omega} \right) dV$ is the angular impulse of the i-th eddy in the control volume, $\boldsymbol{x}_i$ represents a position vector and $\boldsymbol{r}_i \left(= \boldsymbol{x} - \boldsymbol{x}_i \right)$ is the position vector from the centre of the i-th eddy. In the Batchelor turbulence, because the

linear impulse $\boldsymbol{L}_i = 0$, we obtain the global angular momentum $\boldsymbol{H} = \sum \boldsymbol{H}_i$. In contrast, in the Saffman turbulence, $\boldsymbol{L}_i$ is dominant over global angular momentum $\boldsymbol{H}$.

Assuming large-scale self-similarity, Saffman's integral becomes equivalent to

$$L = \beta u^2 L_{uu}^3, \tag{2.42}$$

where β is a constant. In this case, using Kolmogorov's assumption (a), the time evolution of TKE and the integral length scale are expressed as $u^2 \sim t^{-\frac{6}{5}}$ and $L_{uu} \sim t^{\frac{2}{5}}$, respectively.

2.4.2 Inertial subrange

The Kolmogorov's -5/3 law can be observed more than 10 decades in the electron-density power spectrum of the interstellar medium resulting from various direct or indirect observation (Armstrong *et al.*, 1995). In the paper of Kolmogorov (1941a,b), the Kolmogorov's -5/3 law was derived from the dimensional analysis [1]. Thus, a lot of theoretical analyses have been carried out to derive the Kolmogorov's -5/3 law from the first principle such as Navier-Stokes equation. For details, refer to Leslie (1973), McComb (1989, 2014). To the best of my knowledge, the most sophisticated two-point two-time closure will be the Lagrangian Renormalized Approximation (LRA) constructed by Kaneda (1981). Unlike EDQNM, LRA enables us to calculate the statistical quantities theoretically without introduction of any adjustable parameters. Figure 2.3 shows the one-dimensional energy spectra obtained from experiments of grid turbulence and DNS of isotropic turbulence together with the result obtained by LRA. The spectra collapse well in the inertial subrange and dissipation range and disagreement is seen only in the energy containing range. The energy spectra almost following -5/3 power law have been found in many high-Reynolds-number fully-developed turbulent flows (Frisch, 1995).

Here, there is also the celebrated theory for the third order structure function, namely, the Kolmogorov's 4/5 law (Kolmogorov, 1941a). Under the assumption

[1] In his paper, theory has been constructed in physical space, and therefore 2/3 law for the 2nd order structure function has been derived, and -5/3 law for energy spectrum has been derived by his student Obukhov (1941).

of quasi-stationary, i.e. $\left|\frac{\partial}{\partial t}\left\langle \Delta u_{||}^2(r)\right\rangle\right| \ll \left|\frac{\partial u^2}{\partial t}\right| \leq \epsilon$ in the inertial subrange, the time derivative in (2.17) may be neglected, and therefore we have

$$\frac{\partial}{\partial r}\left[r^4\left\langle \Delta u_{||}(r)^3\right\rangle\right] - 6\nu\frac{\partial}{\partial r}\left[r^4\frac{\partial}{\partial r}\left\langle \Delta u_{||}(r)^2\right\rangle\right] = -4r^4\epsilon. \tag{2.43}$$

Integrating the above equation under the boundary conditions such as $\frac{\partial}{\partial r}\left\langle \Delta u_{||}(r)^2\right\rangle = 0$ and $\left\langle \Delta u_{||}(r)^3\right\rangle = 0$ at $r = 0$, we obtain

$$\left\langle \Delta u_{||}(r)^3\right\rangle = -\frac{4}{5}\epsilon r + 6\nu\frac{\partial}{\partial r}\left\langle \Delta u_{||}(r)^2\right\rangle. \tag{2.44}$$

In the inertial subrange, we have

$$\left\langle u_{||}(r)^3\right\rangle = -\frac{4}{5}\epsilon r \tag{2.45}$$

This is called Kolmogorov's 4/5 law. In is worth noting that this equation is directly derived from the Navier-Stokes equation. Kolmogorov (1941b) further argued that the third order structure function $S(r) = \left\langle \Delta v(r)^3\right\rangle / \left\langle \Delta v(r)^2\right\rangle^{\frac{3}{2}}$ leads to

$$\left\langle \Delta v(r)^2\right\rangle = \left(-\frac{4}{5S(r)}\right)^{\frac{2}{3}}(\epsilon r)^{\frac{2}{3}}. \tag{2.46}$$

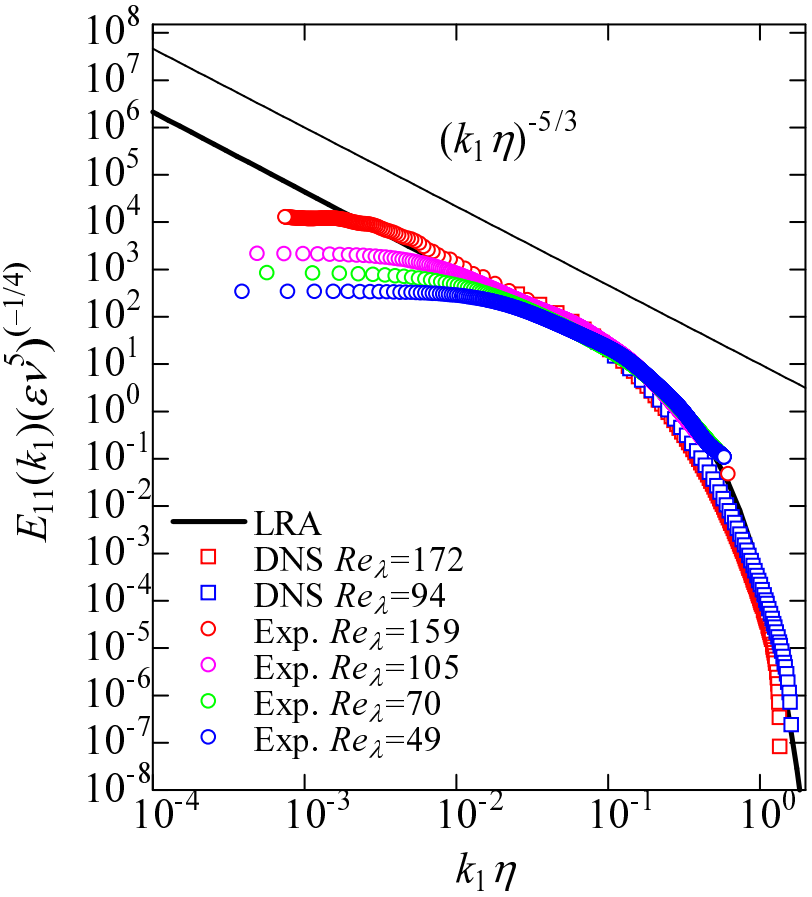

Figure 2.3: The one-dimensional energy spectra normalized by the Kolmogorov variables. The red circle is the experimental result of fractal square grid turbulence.

2.4.3 Dissipation range

From (2.26), we have

$$u^2\left[\frac{\partial^n f(r)}{\partial r^n}\right]_{r=0} = \begin{cases} (-1)^{\frac{n}{2}} \frac{2}{(n+1)(n+3)} \int_0^\infty k^n E(k)\, dk & \text{for even } n, \\ 0 & \text{for odd } n. \end{cases} \tag{2.47}$$

In homogeneous isotropic turbulence, Taylor series expansion of $f(r)$ at $r = 0$ yields (Davidson, 2004)

$$f(r) = 1 - \frac{\langle \boldsymbol{\omega}^2 \rangle}{30u^2} r^2 + \frac{\left\langle (\nabla \times \boldsymbol{\omega})^2 \right\rangle}{840u^2} r^4 - \frac{\left\langle \left(\nabla^2 \boldsymbol{\omega}\right)^2 \right\rangle}{45360u^2} r^6 + \cdots . \tag{2.48}$$

This also gives

$$\lim_{r\to 0} \left\langle \Delta u_{||}(r)^2 \right\rangle = \frac{1}{15} \frac{\epsilon r^2}{\nu}. \tag{2.49}$$

If Taylor series expansion is possible[1], the form of the energy spectrum at high-wavenumbers takes an exponential form, not a power law. In other words, $f_\eta(x)$ must be a fast-decaying function when the energy spectrum can be written by $E(k) = K_0 \epsilon^{\frac{2}{3}} k^{-\frac{5}{3}} f_\eta(k\eta)$. Townsend (1951) introduced the different model eddies and showed that $E(k) \sim k^{-1} \exp(-\alpha k^2 \nu)$ for vortex tube like structures, where α is a model parameter, while $E(k) \sim k^{-2} \exp(-\alpha k^2 \nu)$ for vortex sheet like structure. Interestingly, Kolmogorov's -5/3 law lies between the above models. Thus, it is considered that the Kolmogorov's -5/3 law may be consisted of the superposition of both vortex tubes and vortex sheets. Lundgren (1982) showed that $E(k) \sim k^{-\frac{5}{3}} \exp(-\alpha k^2 \nu)$ for the superposition of the spiralled vortex model. Although there are a lot of proposals for $f_\eta(x)$, a widely-admitted one is (Sagaut & Cambon, 2008)

$$f_\eta(x) = C x^\alpha \exp(\beta x^n). \tag{2.50}$$

Pao (1965) suggested $n = \frac{4}{3}$. Townsend (1951) suggested $n = 2$ assuming linear response at small scales. Two-point spectral closures such as EDQNM, direct interaction approximation and LRA, and the DNS by Ishihara *et al.* (2005) suggested $n = 1$. For other parameters, e.g. C and α, refer to Ishihara *et al.* (2005) and Sagaut & Cambon (2008).

[1]The differentiation possibility of the solution is not proved mathematically. In addition, whether theoretical form of exponential law is appropriate or not is still an open question.

2.5 Rapid distortion theory

RDT is used to explain the statistical properties and eddy structures in turbulence from kinematical and dynamical aspects when turbulence is deformed by mean gradient or by boundary. The advantages of RDT are that the exact solution with a functional form can be obtained and the phenomenology can be explained within the framework of the linear theory. RDT is valid for the case in which turbulence intensity is weak, so that turbulence fluctuations mainly interact with mean velocity. This assumption allows one to linearize the govering equations, and RDT is valid for $T_D \ll T_L = L_{uu}/u_{r.m.s}$, where T_D is the distortion time, T_L is eddy turnover time, L_{uu} is integral length scale and $u_{r.m.s}$ is r.m.s value of velocity fluctuations. The main difference between RDT and exact solution (DNS) can be seen mainly at high wavenumbers for $T_D \ll T_L$ and RDT is no longer valid for $T_D \sim T_L$. Here is a brief review on RDT, so see the literatures (Durbin & Pettersson Reif, 2010; Sagaut & Cambon, 2008; Townsend, 1976) as to its detail on RDT. In the previous studies, RDT has been mainly used for the following cases: (i) uniform distortion of homogeneous turbuelence (Batchelor & Proudman, 1954), (ii) non-uniform distortion of homogeneous turbulence (Hunt, 1973) and (iii) uniform distortion of inhomogeneous turbulence (Townsend, 1980). For case (ii), Hunt's RDT can be classified into the cases $d \gg L_{uu}$ and $d \ll L_{uu}$, where d is the scale of body. For the problem such as $d \gg L_{uu}$, the analysis becomes quite complicated one, whereas $d \ll L_{uu}$, the analysis becomes easy. As to later case, for example, see Nagata *et al.* (2011). As an example of RDT, we consider the famous Townsend's simple shear flow (Townsend, 1976) since the detailed comparison between RDT and DNS have been carried out by Lee *et al.* (1990), Matsumoto *et al.* (1994) and Iida *et al.* (2000). With the assumptions of local homogeneity and high Reynolds number flow, Townsend's simple shear flow is useful to understand the structures of vorticity affected by the mean velocity gradient. For instance, Fung (1990) showed by means of kinematic simulation together with RDT for Townsend's simple shear flow that the velocity structures can be expressed by the highly enlogated high- and low-speed streaks structures as seen in the turbulent boundary layer. Lee *et al.* (1990) also showed the similar behaviours of Reynolds stress $u_1 u_2$ between Townsend's simple shear flow and

turbulent boundary layer. This is typical example of the validity for assumption of local homogeneity. The incompressible inviscid linearized momentum equation is given by

$$\frac{\partial u_i}{\partial t} + U_j \frac{\partial u_i}{\partial x_j} + u_j \frac{\partial U_i}{\partial x_j} = -\frac{1}{\rho}\frac{\partial p}{\partial x_i}, \tag{2.51}$$

where $U_i = x_j \frac{\partial U_i}{\partial x_j}$ for homogeneous flow. As to the examples and constraints of homogeneous flows, refer to Kida & Yanase (1999) for homogeneous incompressible flows and Durbin & Zeman (1992) for homogeneous compressible flows. In homogeneous turbulence, velocity fluctuation can be expressed by the Fourier coefficient,

$$\boldsymbol{u}(\boldsymbol{x}, t) = \int d\boldsymbol{\chi}\ \hat{u}(\boldsymbol{\chi}(t), t) \exp(\imath \boldsymbol{\chi}(t) \cdot \boldsymbol{x}), \tag{2.52}$$

where $\imath = \sqrt{-1}$ and $\boldsymbol{\chi}$ is the wavenumber and is expressed by time. Substituting the above expression into (2.51), the first and second left terms become

$$\frac{\partial u_i}{\partial t} + U_j \frac{\partial u_i}{\partial x_j} = \int d\boldsymbol{\chi}\ \exp(\imath \boldsymbol{\chi} \cdot \boldsymbol{x}) \left[\frac{d\hat{u}_i}{dt} + \imath x_j \left(\frac{d\chi_j}{dt} + \chi_k \frac{\partial U_k}{\partial x_j} \right) \hat{u}_i \right]. \tag{2.53}$$

To ensure homogeneity in Fourier space, the space dependency must become zero, i.e. $\frac{d\chi_j}{dt} + \chi_k \frac{\partial U_k}{\partial x_j} = 0$. In the Townsend's simple shear flow, $U_1 = Sx_2$, $U_2 = U_3 = 0$, the wavenumbers are given by $\chi_1 = k_1$, $\chi_2 = k_2 - Stk_1$ and $\chi_3 = k_3$. The RDT ordinary differential equations for solenoidal modes are given by

$$\frac{d\hat{u}_i(\boldsymbol{\chi}, t)}{dt} = -\frac{\partial U_i}{\partial x_j} \hat{u}_j(\boldsymbol{\chi}, t) + 2\frac{\chi_i \chi_j}{\chi^2} \frac{\partial U_j}{\partial x_k} \hat{u}_k(\boldsymbol{\chi}, t). \tag{2.54}$$

In general, the analytical solutions can be expressed as follows:

$$\hat{u}_i(\boldsymbol{\chi}, t) = A_{ij}(\boldsymbol{\chi}, t)\, \hat{u}_j(\boldsymbol{k}, 0), \tag{2.55}$$

so that Reynolds stress can be given by

$$\langle u_i u_j \rangle = \int d\boldsymbol{\chi}\ A_{i\alpha} A_{j\beta} \Phi_{\alpha\beta}(\boldsymbol{k}, 0), \tag{2.56}$$

where $\Phi_{ij}(\boldsymbol{k}) = \langle \hat{u}_i \hat{u}_j^* \rangle$ is the energy spectral tensor. Lee *et al.* (1990) showed that a good agreement with regard to the time evolution of Reynolds stresses between DNS and RDT. Matsumoto *et al.* (1994) also compared DNS and RDT results and showed that there are no remarkable differences as to the time evolution of

Reynolds stresses and their budgets. However, as shown by Iida *et al.* (2000), RDT is invalid for the statistical quantities such as higher-order moments and small scale structures related to the strain-rate tensor. These differences are come from remarkable effects by nonlinear terms. As above-mentioned, this point is one of weak points in RDT. However, in other words, RDT is useful to understand the dynamics due to nonlinear effects by comparing DNS and RDT.

For more details on RDT, see Townsend (1976), Sagaut & Cambon (2008) and Durbin & Pettersson Reif (2010).

Chapter 3

On invariants in grid turbulence at moderate Reynolds numbers

3.1 Introduction

Comprehensive theories on homogeneous isotropic turbulence have been presented in literatures (e.g. Batchelor 1953; Hinze 1959; Monin & Yaglom 1975; Davidson 2004; Lesieur 2008; Sagaut & Cambon 2008). They consider that there exist important relationships between the decay exponent n of turbulence kinetic energy (TKE) ($=\langle \boldsymbol{u}^2 \rangle /2$; $\langle\ \rangle$ denotes the ensemble average) and the form of energy spectrum at low wavenumbers in homogeneous isotropic turbulence when large-scale self-similarity is assumed. This idea is based on three assumptions: (a) the coefficient of energy spectrum at low wavenumbers is constant throughout the decay, (b) large-scale self-similarity and (c) TKE decays according to $\frac{du_{r.m.s}^2}{dt} = -A\frac{u_{r.m.s}^3}{L_{uu}}$. Here, $u_{r.m.s}\left(\sim \sqrt{\frac{\langle \boldsymbol{u}^2 \rangle}{3}}\right)$ denotes the root mean square of streamwise velocity fluctuations, $L_{uu}(= \int_0^\infty f(r)\, dr$: $f(r) = \langle u(\boldsymbol{x})\, u(\boldsymbol{x} + r\boldsymbol{e}_x)\rangle / \langle u(\boldsymbol{x})^2 \rangle$ is the longitudinal autocorrelation coefficient and r denotes separation) is the integral length scale, t denotes time and A denotes a constant. With regard to (a), Batchelor (1949) and Saffman (1967) showed the permanence of large eddies throughout the decay under the assumption that integral moments of cumulants of velocity and vorticity distributions converge. In this case, once turbulence is fully developed, it remembers its initial conditions: coefficient c_m in the expression

$E(k \to 0) \sim c_m k^m$ becomes an invariant for $m \leq 4$ (Lesieur & Ossia 2000; Davidson 2004; Ishida, Davidson & Kaneda 2006). As a consequence of (b), invariants are expressed as $c_m \sim u_{r.m.s}^2 L_{uu}^{m+1}$, and as a consequence of (c), the TKE decay power law and growth of the integral length scale are respectively represented by

$$\left\langle \boldsymbol{u}^2 \right\rangle \sim t^{-\frac{2(m+1)}{m+3}}, \quad L_{uu} \sim t^{\frac{2}{m+3}}. \tag{3.1}$$

Taylor microscale λ and Kolmogorov scale η are respectively represented by

$$\lambda \sim t^{\frac{1}{2}}, \quad \eta \sim t^{\frac{n+1}{4}}. \tag{3.2}$$

Note that the only requirement to hold (3.2) is a power law, i.e. $\left\langle \boldsymbol{u}^2 \right\rangle \sim t^{-n}$, which can be obtained without similarity.

With regard to the form of the energy spectrum in homogeneous isotropic turbulence, many studies dealing with the Karman–Howarth and the Lin equations suppose some type of self-similarity such as complete self-similarity (e.g. Dryden 1943; Korneyev & Sedov 1976; George 1992), asymptotic-type behaviours (e.g. Speziale & Bernard 1992) and infeasibility of one similarity range extending from $k = 0$ to $k = \infty$ (e.g. Batchelor 1948; Karman & Lin 1949; Saffman 1967). In the case of complete self-similarity of the energy spectrum, the energy spectrum at low wavenumbers is represented as $E(k \to 0) \sim k$, and this yields $\left\langle \boldsymbol{u}^2 \right\rangle \sim t^{-1}$ and $L_{uu} \sim t^{\frac{1}{2}}$. Thus, the Reynolds numbers Re_L $(=\frac{u_{r.m.s} L_{uu}}{\nu})$ and Re_λ $(=\frac{u_{r.m.s}\lambda}{\nu})$, where ν is the kinematic viscosity, are conserved throughout the decay. Furthermore, the ratios of η and L_{uu}, i.e. $\eta/L_{uu} \sim Re_L^{-\frac{3}{4}}$, and of λ and L_{uu}, i.e. $\lambda/L_{uu} \sim Re_L^{-\frac{1}{2}}$ are also conserved. Therefore, $E(k \to 0) \sim k$ is a special case in the sense that it is the only spectrum in which complete self-similarity over all scales is maintained. Turbulence corresponding to this spectrum may be simulated numerically using DNS (Davidson 2011), as done in EDQNM (Lesieur & Ossia 2000).

In contrast, with regard to the energy spectrum that relates to the infeasibility of a single similarity range from $k = 0$ to $k = \infty$ (e.g. Batchelor 1948; Karman & Lin 1949; Saffman 1967), the energy spectrum needs to be divided into at least three ranges: low wavenumber range which is essentially determined by invariants, intermediate range that does not necessarily comply with the similarity characteristics of high wavenumbers but is significantly influenced by the

TKE dissipation rate ϵ and high wavenumber range influenced by both ϵ and ν. It is considered that this is the plausible spectral form of real turbulence such as grid turbulence. With regard to this energy spectrum, two different forms of energy spectra are believed to exist: the Saffman spectrum and the Batchelor spectrum. In Saffman turbulence, the energy spectrum at low wavenumbers is given by $E(k \to 0) \sim \frac{Lk^2}{4\pi^2}$ (Saffman, 1967). Here, $L = \int \langle \boldsymbol{u} \cdot \boldsymbol{u}' \rangle \, d\boldsymbol{r}$ ($\langle \boldsymbol{u} \cdot \boldsymbol{u}' \rangle$ is a two-point velocity correlation, $\boldsymbol{u}'$ is a velocity vector with separation $r = |\boldsymbol{r}|$) is Saffman's integral, which is known as the conservation of linear momentum. In the case of Saffman turbulence, TKE decays according to $\langle \boldsymbol{u}^2 \rangle \sim t^{-\frac{6}{5}}$. By contrast, in Batchelor's turbulence, the energy spectrum at low wavenumbers is given by $E(k \to 0) \sim \frac{Ik^4}{24\pi^2}$ (Batchelor, 1953; Batchelor & Proudman, 1956). Here, under the assumption of $L = 0$, $I = -\int \boldsymbol{r}^2 \langle \boldsymbol{u} \cdot \boldsymbol{u'} \rangle \, d\boldsymbol{r}$ is called Loitsianskii's integral, which is known as the conservation of angular momentum. If Loitsianskii's integral is constant, TKE decays according to $\langle \boldsymbol{u}^2 \rangle \sim t^{-\frac{10}{7}}$. The initial condition determines whether the resulting energy spectrum would be of the Saffman type $E(k \to 0) \sim k^2$ or the Batchelor type $E(k \to 0) \sim k^4$. In the presence of an adequate linear impulse, Saffman turbulence would be generated. Conversely, in the absence of an adequate linear impulse, Batchelor turbulence would be generated.

In numerical simulations, various energy spectra can be set (Lesieur & Ossia, 2000), and the energy spectrum changes according to the initial condition (Lesieur & Ossia, 2000). In addition, Lesieur & Ossia (2000) showed that the TKE power law and the growth of the integral length scale are not inconsistent with the consequence of the self-similarity assumption.

Grid turbulence has been commonly used to investigate the nature of homogeneous isotropic decaying turbulence. However, very few studies (e.g. Krogstad & Davidson 2010) have investigated the existence of invariants related to the large scale. Therefore, the TKE decay exponent and the energy spectrum form at low wavenumbers in grid turbulence are still controversial. Furthermore, experimental investigations on the deterministic characteristics of the energy spectrum at low wavenumbers have been insufficient, although these behaviours have been confirmed via DNS and EDQNM (e.g. Ishida *et al.* 2006; Lesieur & Ossia 2000). In previous experiments, $\langle \boldsymbol{u}^2 \rangle \sim t^{-1}$ (e.g. Gad-El-Hak & Corrsin 1974; Schedvin *et al.* 1974) and the decay exponent close to Saffman's decay exponent or

Kolmogorov's decay exponent (e.g. Comte-Bellot & Corrsin 1966; Mohamedo & LaRue 1990; Lavoie *et al.* 2007; Krogstad & Davidson 2010) have been reported. It should be noted that only a few previous studies applied the appropriate region, i.e. $x/M >$ 40 - 60, to determine the virtual origin and the decay exponent, where x is the distance from the grid and M is the grid mesh size. Therefore, the question whether typical grid turbulence is of the Saffman or Batchelor type or neither (Monin & Yaglom 1975) remains unanswered. The answer to this question is quite important because numerous fundamental and practical experiments in grid turbulence have been conducted thus far. The TKE decay of grid turbulence is reviewed carefully in §3.2.2.

In this study, TKE decay and invariants in grid turbulence are investigated under a wide range of M and Re_M ($=UM/\nu$, where U is the mean velocity) (i.e. M = 10, 15, 25 and 50 mm and Re_M = 6700, 9600, 16000 and 33000) values using cylindrical and square grid bars. In the decay region, the Reynolds numbers based on the Taylor microscale λ, $Re_\lambda \left(= \frac{\sqrt{\langle \boldsymbol{u}^2 \rangle / 3}\lambda}{\nu} \right)$, range from 27 to 112. Here, we used $\langle \boldsymbol{u}^2 \rangle = u^2_{r.m.s} + v^2_{r.m.s} + w^2_{r.m.s} \approx u^2_{r.m.s} + 2v^2_{r.m.s}$. In addition, the effects of the values of M and Re_M (within the range considered here) and the shape of the grid bar (i.e. cylindrical and square) are discussed. In this study, we limit the discussions to 'regular' grid turbulence (i.e. turbulence generated by rectangular array of square or cylindrical bars with a standard value of solidity σ) at moderate Reynolds numbers, i.e. Re_λ=27$\sim$112: we do not consider other types of turbulent generator for generating higher Re_λ. Note that in most previous experiments using a 'regular' grid, $Re_\lambda = O(10) \sim O(10^2)$, which is similar magnitude considered in this study.

3.2 Energy spectra at low wavenumbers and energy decay: overviews

3.2.1 Energy spectra of isotropic turbulence at low wavenumbers

In homogeneous isotopic turbulence, the energy spectrum $E(k)$ is represented as follows (Krogstad & Davidson 2010; Davidson 2011):

$$E(k) = \frac{1}{\pi}\int_0^\infty \langle \boldsymbol{u}\cdot\boldsymbol{u}'\rangle\, kr\sin(kr)\, dr. \tag{3.3}$$

The energy spectrum at low wavenumbers can be expanded in series by Taylor expansion at $k = 0$ as in (2.30). Here,

$$L = \int \langle \boldsymbol{u}\cdot\boldsymbol{u}'\rangle\, d\boldsymbol{r} = \int \frac{u_{r.m.s}^2}{r^2}\frac{\partial}{\partial r}\left[r^3 f(r)\right] d\boldsymbol{r} = 4\pi u_{r.m.s}^2\left[r^3 f(r)\right]_\infty \tag{3.4}$$

is Saffman's integral and

$$I = -\int \boldsymbol{r}^2 \langle \boldsymbol{u}\cdot\boldsymbol{u}'\rangle\, d\boldsymbol{r} = 8\pi r_{r.m.s}^2 \int_0^\infty r^4 f(r)\, dr \tag{3.5}$$

is Loitsianskii's integral. When either Saffman or Loitsianskii's integral is constant with time, the energy spectrum at low wavenumbers is conserved throughout the energy decay process.

Assuming large-scale self-similarity, Saffman's integral becomes equivalent to (2.42). When Saffman's integral becomes constant, we represent the time evolution of the TKE and the integral length scale as follows: (Krogstad & Davidson, 2010):

$$\frac{u_{r.m.s}^2}{u_{r.m.s0}'^2} = \left(1+\frac{5A}{6}\frac{u_{r.m.s0}t}{L_{uu0}}\right)^{-\frac{6}{5}}, \frac{L_{uu}}{L_{uu0}} = \left(1+\frac{5A}{6}\frac{u_{r.m.s0}t}{L_{uu0}}\right)^{\frac{2}{5}}, \tag{3.6}$$

where $u_{r.m.s0}$ and L_{uu0} are the initial values of $u_{r.m.s}$ and L_{uu}, respectively.

Assuming large-scale self-similarity , Loitsianakii's integral becomes equivalent to (2.36). Note that when Loitsianskii's integral becomes constant, the time evolutions of the TKE and integral length scale are as follws:

$$\frac{u_{r.m.s}^2}{u_{r.m.s0}^2} = \left(1 + \frac{7A}{10}\frac{u_{r.m.s0}t}{L_{uu0}}\right)^{-\frac{10}{7}}, \quad \frac{L_{uu}}{L_{uu0}} = \left(1 + \frac{7A}{10}\frac{u_{r.m.s0}t}{L_{uu0}}\right)^{\frac{2}{7}}. \tag{3.7}$$

However, there are opinions that Loitsianskii's integral is not constant during the decay, even if energy spectrum is $E(k \to 0) \sim k^4$ (Batchelor & Proudman 1956; Chasnov 1993). That is, if Loitsianskii's integral depends on time (i.e. $I \sim t^{\gamma}$, where γ is a constant.), the time evolutions of the TKE and integral length scale are as follows:

$$u_{r.m.s}^2 \sim t^{2\frac{5-\gamma}{7}}, \; L_{uu} \sim t^{\frac{2+\gamma}{7}}. \tag{3.8}$$

This means that non-invariance of Loitsianskii's integral does not necessarily preclude Batchelor turbulence.

Here, it is worth revisiting other energy spectra at low wavenumbers in homogeneous isotropic turbulence, as expanded by Davidson (2011). Equation (3.3) could be rewritten as follows:

$$E(k) = \frac{k^2}{\pi}\int_0^{\infty}\frac{\partial}{\partial r}\left(r^3 u_{r.m.s}^2 f(r)\right)\frac{d}{d(kr)}\left(\int_0^{kr}\frac{\sin(t)}{t}dt\right)dr, \tag{3.9}$$

If $f(r \to \infty) \sim r^{-2}$ is satisfied, the energy spectrum at low wavenumbers can be expanded

$$E(k \to 0) = \frac{ku_{r.m.s}^2}{2}\left[3r^2 f(r) + r^3\frac{\partial f(r)}{\partial r}\right]_{r=\infty} - \frac{k^2}{\pi}\int_0^{\infty} r\frac{\partial^2}{\partial r^2}\left(r^3 u_{r.m.s}^2 f(r)\right)dr + \cdots. \tag{3.10}$$

In this case, $u_{r.m.s}^2 L_{uu}^2$ becomes constant throughout the decay when using self-similarity of the integral length scale. Furthermore, $u_{r.m.s}^2\lambda^2$ and $u_{r.m.s}^2\eta^2$ become constant because this case requires complete self-similarity of the spectrum. However, as noted in §3.1, $E(k \to 0) \sim k$ is a special case in the sense that it is the only spectrum in which complete self-similarity over all scales can be maintained at high Re (Davidson, 2011).

The energy spectrum at low wavenumbers can be expanded in series by Taylor expansion of $\sin(kr)$ at $k = 0$. By truncating the Taylor series such as $\sin(kr) =$

$kr - \frac{k^2 r^2}{2} \sin(\phi), 0 < \phi < kr$, we obtain (Davidson, 2011):

$$E(k \to 0) = \frac{Lk^2}{4\pi^2} - \frac{k^3}{2\pi} \int_0^\infty \langle \boldsymbol{u} \cdot \boldsymbol{u}' \rangle r^3 \sin(\phi)\, dr. \tag{3.11}$$

If $f(r \to \infty) \sim r^{-4}$ is satisfied, $E(k \to 0) \sim k^3$ is obtained. In this case, L becomes invariant (=0) throughout the energy decay. This form of the energy spectra at low wavenumbers yields the TKE decay of $\langle \boldsymbol{u}^2 \rangle \sim t^{-\frac{4}{3}}$. Other energy spectra at low wavenumbers have been confirmed in a numerical simulation by Lesieur & Ossia (2000), e.g. $E(k \to 0) \sim k^s$, where $3 < s < 4$. With regard to these theories, considerable parts remain unclear, including physical meanings (Davidson 2011).

3.2.2 TKE decay of grid turbulence

Analyses based on the self-similarity of correlation, structure function and energy spectrum have led to predictions of the TKE decay exponent in homogeneous isotropic turbulence (Kolmogorov 1941c; Dryden 1943; Saffman 1967; George 1992). Therefore, the TKE power decay law in grid turbulence has been investigated to determine which theory expresses real turbulence.

In 'regular' grid turbulence, Comte-Bellot & Corrsin (1966) showed that the decay exponent n lies in $1.15 < n < 1.33$ in the Re_M range of 17000–135000 after straining by contraction for improving isotropy. Lavoie *et al.* (2007) showed that n lies in $1.10 < n < 1.23$ after straining by contraction and lies in $1.04 < n < 1.21$ without contraction at $Re_M = 10400$. Krogstad & Davidson (2010) showed that $n = 1.13 \pm 0.02$. Further, they showed that $u^2_{r.m.s} L^3_{uu}$, which corresponds to Saffman's integral, is constant. From these results, the energy decay exponent n has been measured to be close to Saffman's energy decay of $n = 6/5$. On the other hand, Batchelor & Townsend (1948b) and Bennett & Corrsin (1978) showed that the energy spectrum should take the form $E(k \to 0) \sim k^4$ for Batchelor turbulence because they obtained $u^2_{r.m.s} \sim t^{-\frac{5}{2}}$ in the final period of decay in grid turbulence. Further, Schedvin *et al.* (1974) conducted the experiments at high Re_M of 408000 and suggested that $n = 1$. However, their experiments were conducted at $x/M = 35$, 38, 40 and 41: Their test section was too short

compared with the mesh size for properly determining the decay exponent and realising quasi-homogeneous isotropic turbulence, as mentioned later.

For generating high Re_λ turbulence, other types of turbulent generator have been used. Gad-El-Hak & Corrsin (1974) measured the decay exponent in the Re_M range of 41800-73400 using an active grid, which injects air into the free stream. For co-flow injection, which generates relatively isotropic turbulence, they reported that n lies in $1.04 < n < 1.28$, with the lowest value of n corresponding to the highest injection rate. However, significant inhomogeneities were observed at the highest injection rate. For counter-flow injection, they estimated $1.00 < n < 1.24$. However, this arrangement also produced significant anisotropy and inhomogeneities. Mydlarski & Warhaft (1996) conducted the experiments with an active grid at $Re_\lambda = 319$ and estimated the TKE decay exponent $n = 1.21$. Then, Antonia *et al.* (2013) reestimated the TKE decay exponent of Makita (1991) and reported that $n = 1.12$ for an active grid at $Re_\lambda = 387$.

With regard the TKE decay exponent n, George (1992) found that $\langle \boldsymbol{u}^2 \rangle \sim t^{-1}$ at very high Reynolds numbers. Then, he showed that there is a possiblity that the TKE decay exponent depends on the turbulent Reynolds number and that TKE decay asymptotes to $\langle \boldsymbol{u}^2 \rangle \sim t^{-1}$ at very high Reynolds numbers. Actually, experimental (George 1992; George & Davidson 2004) and numerical (Burattini *et al.* 2006) results asymptote to $\langle \boldsymbol{u}^2 \rangle \sim t^{-1}$ with increasing Reynolds number. Antonia *et al.* (2013) recently showed that TKE power law approaches $\langle \boldsymbol{u}^2 \rangle \sim t^{-1}$ with increasing Reynolds number. However, most previous high–Reynolds–number experiments lack large-scale homogneities in cross-section (e.g. Makita 1991; Kang *et al.* 2003). In that sense, it is unclear that $\langle \boldsymbol{u}^2 \rangle \sim t^{-1}$ is due to $E(k \to 0) \sim k$. Note that the corresponding invariant, $u_{r.m.s}^2 L_{uu}^2$=constant, has not been confirmed in previous studies on grid turbulence. In contrast, Burattini *et al.* (2006), Huang & Leonard (1994) and Mohamedo & LaRue (1990) suggested that $n \neq 1$ at sufficiently high Re_M. Davidson (2011) showed that the energy spectrum corresponding to $\langle \boldsymbol{u}^2 \rangle \sim t^{-1}$, $E(k \to 0) \sim k$, is unlikely in grid turbulence because its energy spectrum tensor diverges as $k \to 0$ and long range correlation $f(r \to \infty) \sim r^{-2}$ is too strong. Therefore, he concluded that the minimum energy decay rate in grid turbulence is probably that for Saffman

turbulence and slight departure of the decay exponent from 6/5 for Saffman turbulence may be the influence of A, which is a weak function of t as discussed later. Thus, these asymptotic behaviour to $\langle \boldsymbol{u}^2 \rangle \sim t^{-1}$ should be carefully investigated by means of experiments at high Re_λ with large-scale homogeneities. This will be a subject of future study and is out of scope in this paper.

3.3 Experiments

Schematic views of the experimental apparatus and the test section are shown in figures 3.1(a) and 3.1(b), respectively. The experiments were conducted in a closed-loop wind tunnel at Nagoya University (figure 3.1a), the same as that used in Nagata *et al.* (2011) and Sasoh *et al.* (2014). The test section has a width of 0.994 m, height of 0.46 m and length of 4 m. The side walls of the test section are made of acrylic resin, and the lower and upper walls are made of aluminium. The contraction ratio is 12:1, and the background turbulence is less than 0.4% of mean velocity. Turbulence was generated by grids (figure 3.2(a): $M = 10$ mm and 25 mm, figure 3.2(b): $M = 15$ mm, 25 mm and 50 mm) installed at the entrance of the wind tunnel's test section, as shown in figure 3.1(b). Grid solidity was $\sigma = 0.36$ for all grids. This value is typical of turbulence-generating grids used in previous studies (e.g. Batchelor & Townsend 1948b; Bennett & Corrsin 1978; Gad-El-Hak & Corrsin 1974; Lavoie *et al.* 2007; Nagata *et al.* 2011). The mesh Reynolds numbers were set to $Re_M = 6700$, 9600, 16000 and 33000. The experimental conditions are summarised in Table 3.1.

For streamwise and vertical velocity measurements, constant-temperature anemometry (DANTEC Streamline) with an I-type hot-wire probe (DANTEC 55P11, hereinafter referred to as 'single wire') and an X-type hot-wire probe (DANTEC 55P61, hereinafter referred to as 'cross wire') were used. The diameter of the single wire was 5 μm and its length was 1.25 mm. The diameter of the cross wire was 5 μm and its length was 1.25 mm; the separation between these two sensors was 1 mm. The single wire was calibrated in the wind tunnel, and instantaneous streamwise velocity was calculated according to King's law. The cross wire was calibrated in yaw in the wind tunnel. A set of calibration data were obtained for both hot-wire sensors by varying the yaw angle θ from -45° to 45°

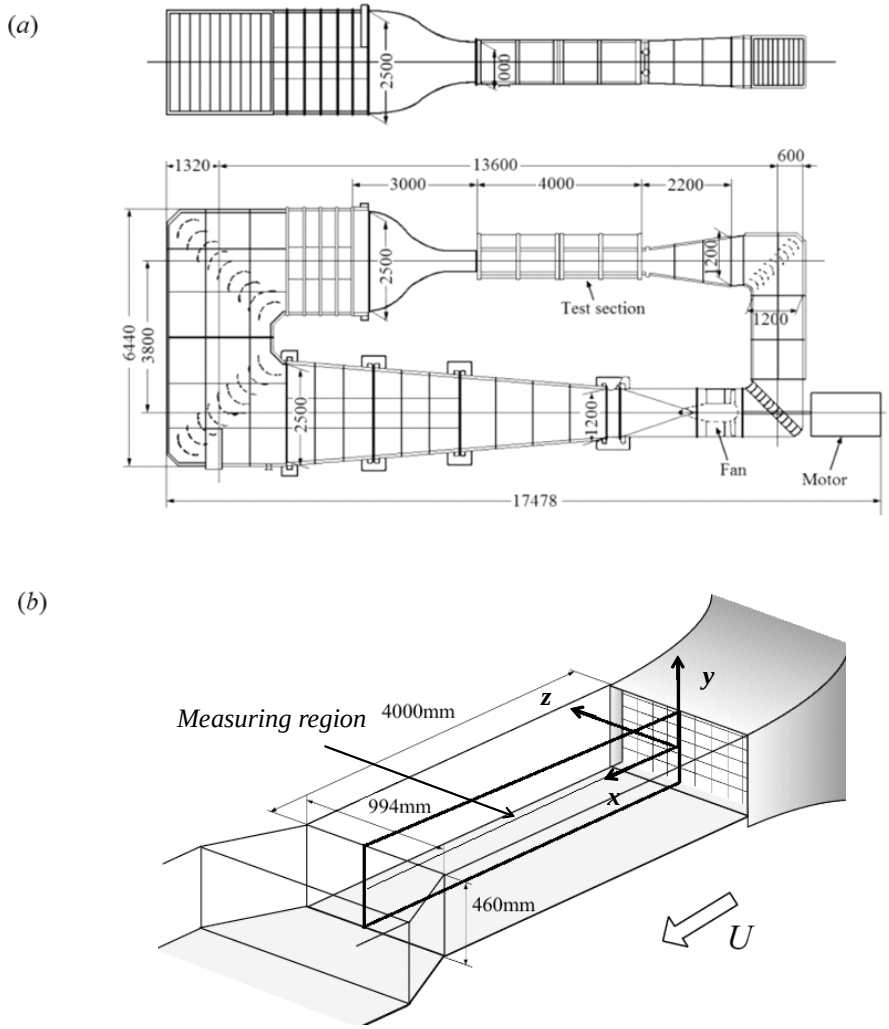

Figure 3.1: Experimental setup: (a) wind tunnel overview and (b) schematic of test section and measurement area

Figure 3.2: Schematic of (a) cylindrical grid and (b) square grid

in steps of 5°, while maintaining a constant velocity across the probe. Then, the effective velocity U_{eff} was calculated as $U_{eff} = Vf(\theta) = V\sqrt{\cos^2\theta + k^2\sin^2\theta}$ (Hinze 1959). Here, $f(\theta)$ is a yaw function and the unknown coefficient k for each wire was determined from yaw-angle calibration. The Levenberg-Marquardt method was used for calculating the unknown parameter. V was calculated from $V = \frac{U_{1eff}+U_{2eff}}{f_1(\theta)+f_2(\theta)}$ using the bisection method. Here, $f_1(\theta)$ and $f_2(\theta)$ are the yaw functions of hot wires 1 and 2, respectively. Then, instantaneous streamwise velocity $U_{ins.}$ and instantaneous vertical velocity $V_{ins.}$ were calculated from $U_{ins.} = V\cos\theta$ and $V_{ins.} = V\sin\theta$. The frequency response of the single wire was found to be approximately 60 kHz for U= 10 ms^{-1}. The sampling rate f_s in the single-wire experiments was set to 50 kHz for obtaining reliable derivative quantities, e.g. TKE dissipation rate ϵ. The sampling rate f_s for the cross wire was set to 40 kHz. The frequency response was found to be approximately 50 kHz for U = 10 ms^{-1}. For both measurements, the data sampling number was 1048576 and 10 measurements were conducted at each point for reducing statistical errors. Measurements using the single wire were conducted from x = 500 mm to 2350 mm in steps of 50 mm at the centre of the wind tunnel. Measurements using the cross wire were conducted from x = 500 mm to 2100 mm in steps of 50 mm at the centre of the wind tunnel.

Furthermore, for confirming homogeneity, measurements were conducted in the vertical direction at the most downstream location. We adjusted the mean velocities to be the same as those in the decay characteristics experiments. Note that homogeneity tends to break in the far downstream region because eddies become larger relative to the tunnel side in that region. The sampling rate f_s for this measurement was set to 10 kHz. This value is sufficient for resolving the Kolmogorov frequency. Measurements were conducted from y = 50 mm to 410 mm in steps of 20 mm. The data sampling number for this case was 262144 and 10 measurements were conducted at each point.

If we calculate derivative quantities directly without removing electric noise, suspicious derivative quantities are obtained, and their values may depend on the filter's cutoff. In the case without electric noise removal, artificial signals having the characteristics of white noise are seen. As a characteristic of white noise, the power spectrum $P(f)$ takes the form $P(f) = const.$ with the same intensity for

all frequency regions; therefore, the S/N ratio decreases in the high-wavenumber region. The effect of electric noise is considerable in the one-dimensional dissipation spectrum. Therefore, we should remove these artificial signals for obtaining reliable derivative quantities. There are mainly two methods of noise removal: an analogue filter and a digital filter (with the use of Fourier transform, wavelet transform and so on). In this study, we used a digital filter. Two methods are used for calculating the Taylor microscale λ. In the first method, we used

$$\lambda^2 = \frac{u_{r.m.s}^2}{\left\langle \left(\frac{\partial u}{\partial x}\right)^2 \right\rangle} = \frac{\int_{k_{min}}^{k_{max}} E_{11}(k_1)\, dk_1}{\int_{k_{min}}^{k_{max}} k_1^2 E_{11}(k_1)\, dk_1} = \frac{U^2}{4\pi^2} \frac{\int_{f_{min}}^{f_{max}} E_{11}(f)\, df}{\int_{f_{min}}^{f_{max}} f^2 E_{11}(f)\, df} \tag{3.12}$$

where $k_{min} = \frac{2\pi f_{min}}{U}$ is the lowest wavenumber which is determined from the data number and $k_{max} = \frac{2\pi f_{max}}{U}$ is the cutoff wavenumber.

The second method is the use of the Fourier expansion derivative. Let us consider the derivative of signal $x(t)$ and express $x(t)$ in Fourier expansion. Then, we have,

$$x(t) \sim \frac{a_0}{2} + a_1 \cos(\omega_1 t) + b_1 \sin(\omega_1 t) + \cdots + a_{n_{max}} \cos(\omega_{n_{max}} t) + b_{n_{max}} \sin(\omega_{n_{max}} t) + \cdots + a_N \cos(\omega_N t) + b_N \sin(\omega_N t), \tag{3.13}$$

where $\omega_N = \pi f_s$ is the Nyquist frequency, whose value is higher than typical Kolmogorov frequency, and the time derivative of above equation is as follows:

$$\frac{dx(t)}{dt} \sim -\omega_1 a_1 \sin(\omega_1 t) + \omega_1 b_1 \cos(\omega_1 t) + \cdots - \omega_{n_{max}} a_{n_{max}} \sin(\omega_{n_{max}} t) + \omega_{n_{max}} \cos(\omega_{n_{max}} t) + \cdots - \omega_N a_N \sin(\omega_N t) + \omega_N b_N \cos(\omega_N t). \tag{3.14}$$

As shown in (3.14), the high sampling rate affects the derivative quantity because the Nyquist frequency ω_N increases with an increase in the sampling rate. Thus, we should truncate the irrelevant signal, whose frequency is higher than the optimum frequency $\omega_{n_{max}}$ in the Fourier space. Here, $\omega_{n_{max}}$ is the optimum frequency, which does not include the effects of white noise. Using the inverse Fourier transform, we could calculate derivative quantities. We confirmed that there are no differences between the first and the second methods when calculating λ. Thus, these methods are reliable for obtaining derivative quantities, e.g.

TKE dissipation rate ϵ, derivative skewness $S_{\frac{\partial u}{\partial x}}$ and derivative flatness $F_{\frac{\partial u}{\partial x}}$. The results of $S_{\frac{\partial u}{\partial x}}$ and $F_{\frac{\partial u}{\partial x}}$ are shown in § 3.4 and are in good agreement with those of a previous study (Sreenivasan & Antonia, 1997).

The longitudinal and lateral integral length scales, L_{uu} and L_{vv}, are defined as the integration of the longitudinal and lateral correlation coefficients, $f(r)$ and $g(r) = \langle v(\boldsymbol{x})\, v(\boldsymbol{x} + r\boldsymbol{e}_x)\rangle / \langle v(\boldsymbol{x})^2 \rangle$, from 0 to ∞, respectively. However, in the pratical calculation of the integral length scales, the correlation coefficient can never be measured for infinite separation and the correlation at large separation is affected by noise. In this study, we truncated the integration from 0 to r_f for calculating L_{uu} and the integration from 0 to r_g for calculating L_{vv}:

$$L_{uu} = \int_0^{r_f} f(r)\, dr, \quad L_{vv} = \int_0^{r_g} g(r)\, dr \tag{3.15}$$

In this study, r_f was set to the first zero-crossing point and r_g was set to the second zero-crossing point, where $g(r)$ turns into positive from negative. We also used Taylor frozen hypothesis. Typical profiles of $f(r)$ and $g(r)$ are shown in the next section.

Table 3.1: Experimental conditions and decay exponent n obtained using regression method (RM) and maximum decay range method (MDRM). Additionally, the results of Krogstad & Davidson (2010) (Ref. *a*) and Lavoie *et al.* (2007) (Ref. *b*) are listed. $Sq25lac$, $Cy25lbc$, $Cy25lac$ and $Cy25lhc$ correspond to the results with contraction. The expression of Cylinder HW indicates a cylindrical grid wound by a small helical wire.

Present work									RM			MDRM		
	Symbol	M [mm]	Bar shape	U_∞ [ms^{-1}]	L_{uu}/M	η [mm]	Re_M	Re_λ	n	x_{low}/M	x_0/M	n	x_{start}/M	x_0/M
$Cy10a$	▽	10	Cylinder	10.6	0.98–2.03	0.21–0.45	6700	27–29	1.18	50	5.01	1.18	50	4.0
$Sq15a$	○	15	Square	10.4	0.72–1.25	0.18–0.32	9600	47–50	1.15	53	3.47	1.17	50	3.0
$Sq15b$	△	15	Square	17.2	0.78–1.39	0.14–0.27	16000	61–67	1.12	53	4.69	1.19	53	3.0
$Cy25a$	⊕	25	Cylinder	10.4	0.40–0.67	0.16–0.35	16000	59–65	1.12	58	4.10	1.13	60	3.0
$Cy25b$	⊗	25	Cylinder	20.0	0.44–0.75	0.10–0.24	33000	67–72	1.10	62	5.01	1.12	60	3.0
$Sq25a$	□	25	Square	10.4	0.46–0.80	0.12–0.24	16000	58–64	1.16	48	5.71	1.20	50	3.0
$Sq25b$	×	25	Square	20.0	0.51–1.01	0.08–0.20	33000	88–91	1.12	44	4.65	1.14	60	3.0
$Sq50a$	+	50	Square	10.5	0.29–0.48	0.10–0.24	33000	99–112	–	–	–	–	–	–
Ref. *a*														
$Sq40a$	◎	40	Square	13.5	0.61–1.15	–	36000	73–82	1.13	45	7.30	1.12	50	6.0
Ref. *b*														
$Sq25la$	⧈	24.76	Square	6.4	–	0.41	10400	43	–	–	–	1.04± 0.02	30	7.4±0.8
$Cy25lb$	◬	24.76	Cylinder	12.1	–	0.35	10400	42	–	–	–	1.19± 0.04	32	5.7±1.3
$Cy25la$	▽	24.76	Cylinder	9.8	–	0.33	10400	40	–	–	–	1.21± 0.03	30	3.8±1.0
$Sq25lac$	◫	24.76	Square	6.4	–	0.42	10400	40	–	–	–	1.20± 0.03	34	4.9±1.0
$Cy25lbc$	◬	24.76	Cylinder	12.2	–	0.31	10400	39	–	–	–	1.22± 0.02	30	5.2±0.7
$Cy25lac$	▽	24.76	Cylinder	6.4	–	0.31	10400	36	–	–	–	1.22± 0.02	25	3.1±0.6
$Cy25lhc$	ⓘ	24.76	Cylinder HW	6.4	–	0.31	10400	36	–	–	–	1.22± 0.02	25	3.1±0.6

3.4 Results and discussion

3.4.1 Homogeneities and isotropy

In this study, we are interested in the behaviour of large-scale structures. Thus, we first demonstrate that there are no or negligible effects of wind tunnel size on the measurements. To this end, we carefully checked the homogeneities of the vertical direction (cross-section) at the most downstream position. Figure 3.3 shows the vertical distribution of $u_{r.m.s}$ normalised by U at the most downstream position . The vertical coordinate y is normalised by L_{uu}. As shown in figure 3.3, side wall effects are very small except for $Sq50a$, and we confirmed good homogeneities across a wide range in the vertical direction. Note that width of the test section is more than twice as large as the height. With regard to $Sq50a$, we do not make quantitative discussions of the statistics because of the narrow range of homogeneities. The large homogeneous domain ensures that the turbulence has enough time to settle down to a homogeneous shear-free state. Thus, the bulk properties of a turbulent flow evolving in a very large domain ($L_{Domain} \gg L_{uu}$) are not influenced by the remote boundaries.

We expect the skewness S and the flatness F of homogeneous isotropic turbulence to be 0 and 3, respectively, for all velocity components. However, the distribution of fluctuating velocities in grid turbulence is expected to depart slightly from the Gaussian distribution owing to slow streamwise decay. Figure 3.4 shows the streamwise distribution of streamwise velocity skewness $S_u\,(=\langle u^3\rangle/u^3_{r.m.s})$ and flatness $F_u\,(=\langle u^4\rangle/u^4_{r.m.s})$. As shown in figure 3.4, the positive values of S_u near the grid decrease with increasing downstream distance. These results are consistent with those of Bennett & Corrsin (1978) and Mohamedo & LaRue (1990). Note that the values of S_u approach 0 around $x/M = 50$–60, while $F_u \sim 3$ in the entire streamwise direction. This implies that there are some effects of shear in the region $x/M < 50$–60.

For isotropic turbulence, the ratios $u^2_{r.m.s}/v^2_{r.m.s}$ and $u^2_{r.m.s}/w^2_{r.m.s}$ should be unity everywhere, where $v^2_{r.m.s}$ and $w^2_{r.m.s}$ are the vertical and spanwise turbulent intensities, respectively. However, as observed in previous experiments (e.g. Comte-Bellot & Corrsin 1966; Lavoie *et al.* 2007), $u_{r.m.s}$ is slightly larger than

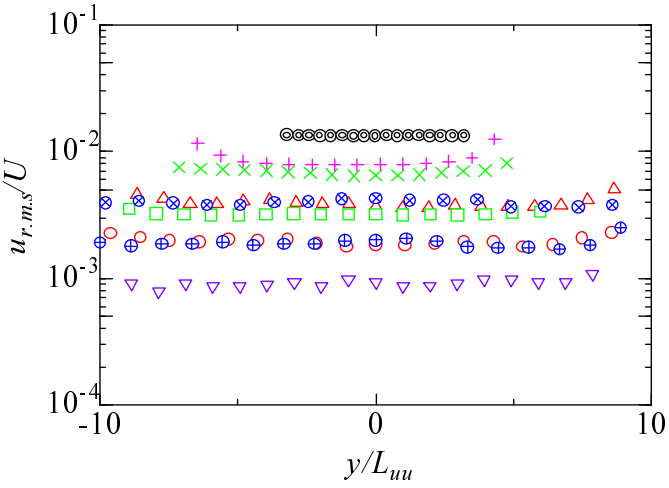

Figure 3.3: Vertical distribution of $u_{r.m.s}/U$. The vertical coordinate y is normalised by L_{uu}. For symbols, see Table 3.1.

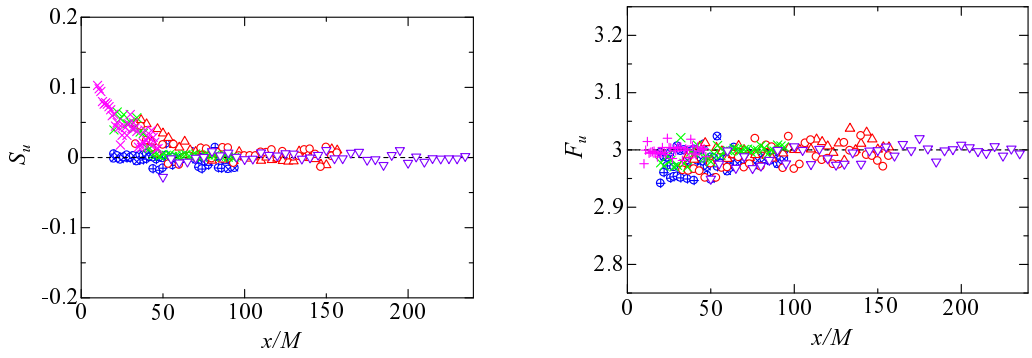

Figure 3.4: Streamwise distribution of streamwise velocity skewness S_u and flatness F_u. For symbols, see Table 3.1.

$v_{r.m.s}$ and $w_{r.m.s}$ in grid turbulence. The ratio of $u^2_{r.m.s}$ and $v^2_{r.m.s}$ is shown in figure 3.5. Additionally, the profiles of $u^2_{r.m.s}/v^2_{r.m.s}$ and $u^2_{r.m.s}/w^2_{r.m.s}$ in Lavoie *et al.* (2007) and Krogstad & Davidson (2010) are shown in figure 3.5. Profiles of $u^2_{r.m.s}/w^2_{r.m.s}$ without contraction in Lavoie *et al.* (2007) ($Sq25la$: $\square$, $Cy25lb$: $\triangle$, $Cy25la$: $\triangledown$) are nearly constant for $x/M > 50$, although slight anisotropies stand out. These anisotropies can be reduced by introducing the contraction as shown by Lavoie *et al.* (2007) (not shown in figure 3.5). In contrast, the ratios given in Krogstad & Davidson (2010) are close to unity. Our results shows that values of $u^2_{r.m.s}/v^2_{r.m.s}$ for $Cy25a$, $Cy25b$, $Sq25a$, $Sq25b$ and $Sq50a$ are close to unity. Profiles of $u^2_{r.m.s}/v^2_{r.m.s}$ for $Cy10a$, $Sq15a$ and $Sq15b$ show slight anisotropy; they are close to the results of Lavoie *et al.* (2007).

To investigate the degree of anisotropy and the effects of different grid geometries, autocorrelation coefficients are investigated. In homogeneous isotropic turbulence, the relationship between $f(r)$ and $g(r)$ is found to be as follows from the relationship $g(r) = f(r) + \frac{1}{2} r \frac{\partial f(r)}{\partial r}$ (Batchelor, 1953):

$$\int_0^\infty r^m g(r)\, dr = \frac{1-m}{2} \int_0^\infty r^m f(r)\, dr \quad (m \geq 0)\,. \tag{3.16}$$

From (3.16), $g(r)$ is negative for large r if $f(r)$ is positive for large r. Figure 3.6 shows $f(r)$ and $g(r)$ at $x/M = 50$. As shown in figure 3.6, the autocorrelation coefficients have slightly different forms depending on grid geometry. Similar observation was made in Lavoie *et al.* (2005), although they made the observation from the structure function. As shown in figure 3.6, $g(r)$ agrees well with the $g(r)_{cal.}$ calculated using the isotropic relationship for $Sq25a$ and $Sq25b$. Note that $g(r)$ for the square grids has a smaller negative value than that for the cylindrical grids. For both grids, $g(r)$ takes large negative values at lower Re_λ than those at high Re_λ. This overshoot at large separations suggests that the turbulence generated by the cylindrical grids is more periodic than that generated by the square grids. Then, the form of the autocorrelation coefficients depend on Re_λ.

To demonstrate that the present grid turbulence is a typical one (which is free from the tunnel's wall effect) and to confirm that reliable derivative quantities can be obtained, we compared derivative skewness $S_{\frac{\partial u}{\partial x}}$ $\left(= \left\langle (\partial u/\partial x)^3 \right\rangle / \left\langle (\partial u/\partial x)^2 \right\rangle^{\frac{3}{2}}\right)$

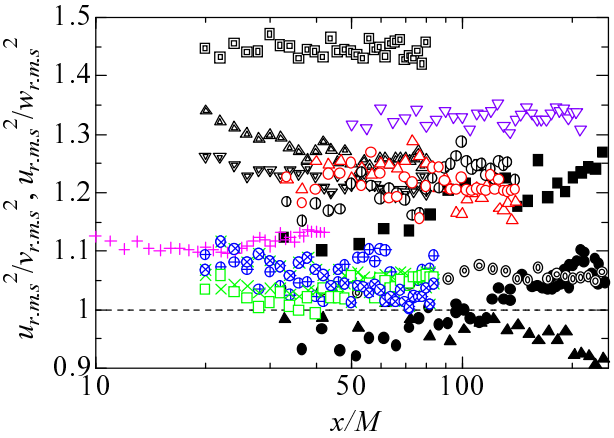

Figure 3.5: Streamwise distribution of stress ratios. For symbols, see Table 3.1. Also included are distributions from Krogstad & Davidson (2010); $(u_{r.m.s}/v_{r.m.s})^2$ (LDA): ●, $(u_{r.m.s}/v_{r.m.s})^2$ (CTA) : ▲, $(u_{r.m.s}/w_{r.m.s})^2$ (CTA) : ■, $q^2/3u^2_{r.m.s}$ (CTA) : ◎ and Lavoie *et al.* (2007). The symbols used in Lavoie *et al.* (2007) are defined in Table 3.1.

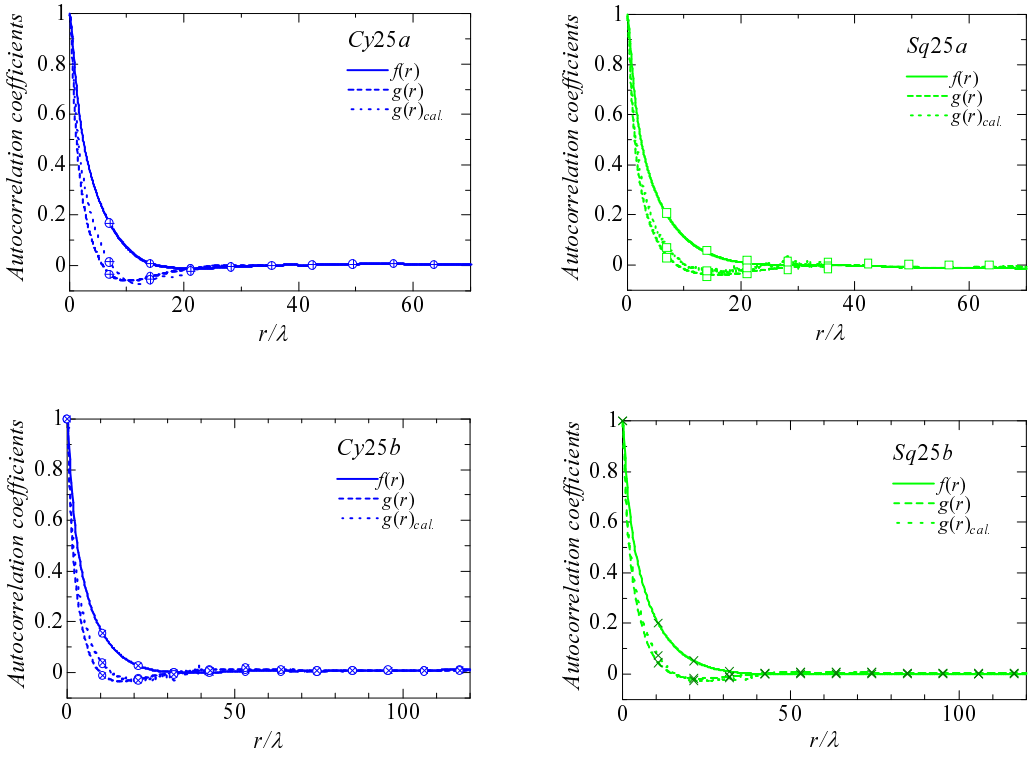

Figure 3.6: Measured and calculated (subscript *cal.*) distribution of autocorrelation coefficients for different grid geometries and Re_λ.

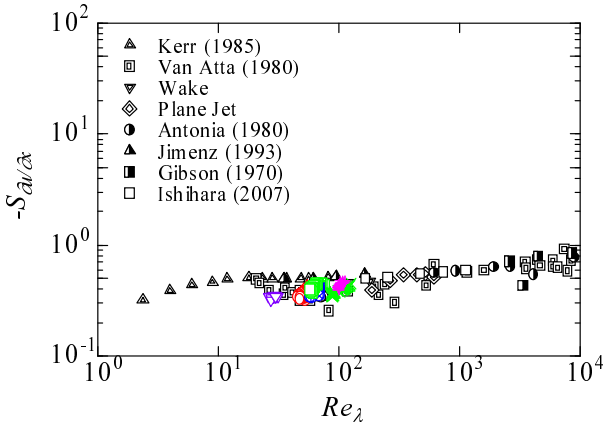

Figure 3.7: Relationship between derivative skewness $S_{\frac{\partial u}{\partial x}}$ and Re_λ. The data are compared with those compiled by Sreenivasan & Antonia (1997). For symbols used in the present study, see Table 3.1. The symbols used in Sreenivasan & Antonia (1997) are shown in the figure. See Sreenivasan & Antonia (1997) about citations. DNS results for $k_{max}\eta \approx 1$ in Ishihara *et al.* (2007) are also included.

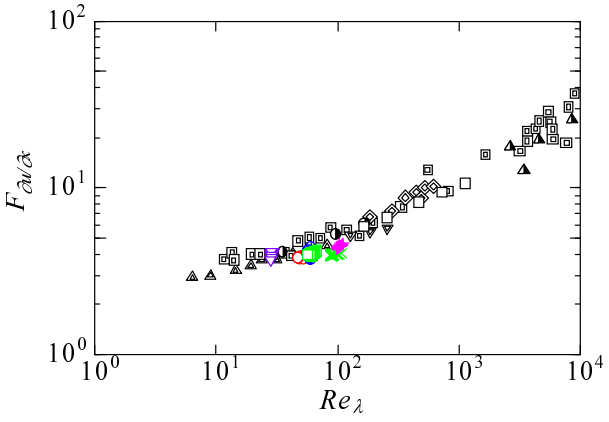

Figure 3.8: Relationship between derivative flatness $F_{\frac{\partial u}{\partial x}}$ and Re_λ. Symbols are the same as those in figure 3.7.

and derivative flatness $F_{\frac{\partial u}{\partial x}}\left(=\left\langle(\partial u/\partial x)^4\right\rangle/\left\langle(\partial u/\partial x)^2\right\rangle^2\right)$ with those compiled by Sreenivasan & Antonia (1997) in figures 3.7 and 3.8: We confirmed good agreements with the previous results.

3.4.2 Energy decay

Figure 3.9 shows the decay of turbulent intensity normalised by U^2. It can be seen that $u^2_{r.m.s}/U^2$ largely depends on M and grid geometry, but it has a minor Re_M dependence for the same M value and grid geometry.

In grid turbulence, streamwise turbulent intensity decays according to the following power law:

$$\frac{u^2_{r.m.s}}{U^2} = a\left(\frac{x}{M} - \frac{x_0}{M}\right)^{-n}, \tag{3.17}$$

where a is a constant. The methods for calculating n and the virtual origin x_0 are very important while discussing the energy decay characteristics of grid turbulence. In (3.17), three unknowns, a, x_0 and n are included. In this study, the two methods used by Krogstad & Davidson (2010) are adopted.

In the first method, called the regression method (RM), optimum data that do not include data from inadequate regions (i.e. the upstream region, where turbulence is not fully developed, and the region corresponding to the final period of decay) are selected. Then, the objective function is determined using the data from the adequate region. First, all data measured from the upstream to the downstream direction are employed for obtaining a power function using a nonlinear least-squares method. Here, we used the Levenberg-Marquardt method. Let x_{low} be the first streamwise position for obtaining the smallest deviation between the measured data and the objective function. Second, the data are fitted from the most downstream point by fixing x_{low}. Let x_{high} be the position for obtaining the smallest deviation. Finally, the power function exponent is obtained by fitting the data in the regions between x_{low} and x_{high}.

The second method is called the maximum decay range method (MDRM) suggested by Lavoie *et al.* (2007). In this method, some virtual origins are given, and the decay exponent is searched for by fitting the power function over different

regions. To this end, at least 10 points are fixed in the most downstream region. Let x_{start} be the starting point for fitting, and let $n\left(x_{start}\right)$ be the decay exponent calculated from the fitting process originating from x_{start}.

$$n\left(x_{start}\right) = \ln\left(\frac{a}{\frac{u^2_{r.m.s}}{U^2}\left(x_{start}\right)}\right) / \ln\left(\frac{x_{start} - x_0}{M}\right) \tag{3.18}$$

The Levenberg-Marquardt method was used for fitting. The virtual origin was determined from among the assumed values that provided the minimum scattering of n. Finally, the decay exponent is obtained by averaging for the determined x_0 values.

Table 3.1 lists the values of n obtained using the two methods. In addition, the results of Krogstad & Davidson (2010) (Ref. a in Table 3.1) and Lavoie *et al.* (2007) (Ref. b in Table 3.1) are listed. In both methods, the values of n are close to 6/5 for Saffman turbulence. Additionally, the results of Krogstad & Davidson (2010) and Lavoie *et al.* (2007) are close to 6/5. Lavoie *et al.* (2007) investigated the effects of initial conditions using a square mesh, cylindrical mesh and a cylindrical mesh wound by a small helical wire. They showed that the decay exponent for square grids without contraction is $n = 1.04 \pm 0.02$ and that for the other cylindrical grids without contraction is $n \approx 6/5$. Note that the values of the decay exponents in our results, the results of Krogstad & Davidson (2010) and those of Lavoie *et al.* (2007) are different from the previously adopted values of $n = 1.25$ (Comte-Bellot & Corrsin, 1966) and $n = 1.3$ (Mohamedo & LaRue, 1990). Furthermore, they are different from $n = 1$, which was predicted by Dryden (1943). In addition, the values of the virtual origins are never zero, as suggested by Mohamedo & LaRue (1990). The values of x_{low} for RM and x_{start} for MDRM are listed in Table 3.1. On average, the decay of turbulent intensity is well fitted using the power law in the region $x/M > 50$ for the square grids and $x/M > 60$ for the cylindrical grids.

Figure 3.10 shows the power law decay. Hereafter, x_0 obtained by RM is used. Speziale & Bernard (1992) showed that TKE decay in completely self-similar isotropic turbulence is determined by the initial conditions. With regard to the difference in grid geometry (i.e. $Sq25a$ and $Cy25a$, $Sq25b$ and $Cy25b$ in our results), there are no differences in terms of the decay exponents. In contrast,

turbulence generated by the cylindrical grids is slightly anisotropic compared with that generated by the square grids, as mentioned in § 3.1, and there are slight differences in the starting points of their respective fully developed regions. For turbulence generated by the cylindrical grids, the fully developed region tends to be far from the grids, while for turbulence generated by the square grids, the fully developed region tends to start slightly closer to the grids. In fact, the power law decay regions start from a farther location for the cylindrical grids in RM and MDRM. This is due to the difference in the wake-development processes. In fact, Lavoie *et al.* (2007) showed that the peaks in the spectra remain at $x/M = 20$, and this is associated with strong periodic motions in the flow. Then, there are larger overshoots in autocorrelation coefficients for the cylindrical grids, as shown in figure 3.6. Thus, it is possible that the turbulence generated by the cylindrical grids needs a longer distance to be fully developed compared with that generated by the square grids. Note that the values of x_0 are similar for both cylindrical and square grids.

Figure 3.11 shows the streamwise variation in Re_λ. In homogenous isotropic turbulence, Re_λ is represented by $Re_\lambda \sim t^{\frac{-n+1}{2}}$. Figure 3.11 also shows the theoretically estimated $Re_\lambda \sim (x/M - x_0/M)^{-0.1}$ for Saffman turbulence (i.e. $n = 6/5$). Hereafter, the coloured symbols for this study correspond to the downstream regions of x_{low}/M.

3.4.3 TKE dissipation rate and effect of coefficient A

It is known that the following relation is satisfied at high Re_λ from experiments and numerical simulations (e.g. Taylor 1935; Sreenivasan 1984; Kaneda *et al.* 2003):

$$\frac{du^2_{r.m.s}}{dt} = -A\frac{u^3_{r.m.s}}{L_{uu}}, \tag{3.19}$$

The relationship between the coefficient A and Re_λ was investigated by means of DNS (Kaneda *et al.*, 2003): A is almost constant at high Re_λ. When (3.19) holds, TKE dissipation rate can be considered to be dominated by large-scale eddies. Thus, the energy spectrum at low wavenumbers plays an important role

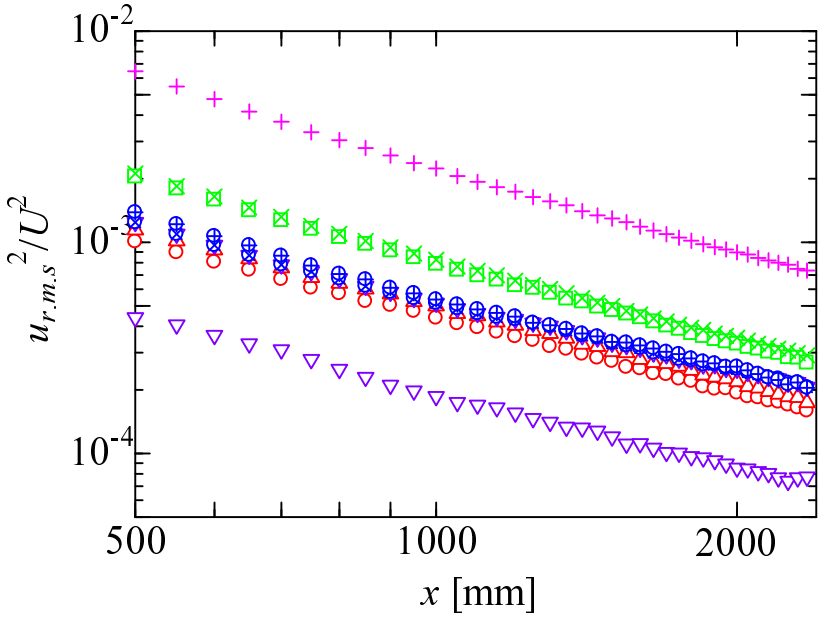

Figure 3.9: Turbulent intensity decay. For symbols, see Table 3.1.

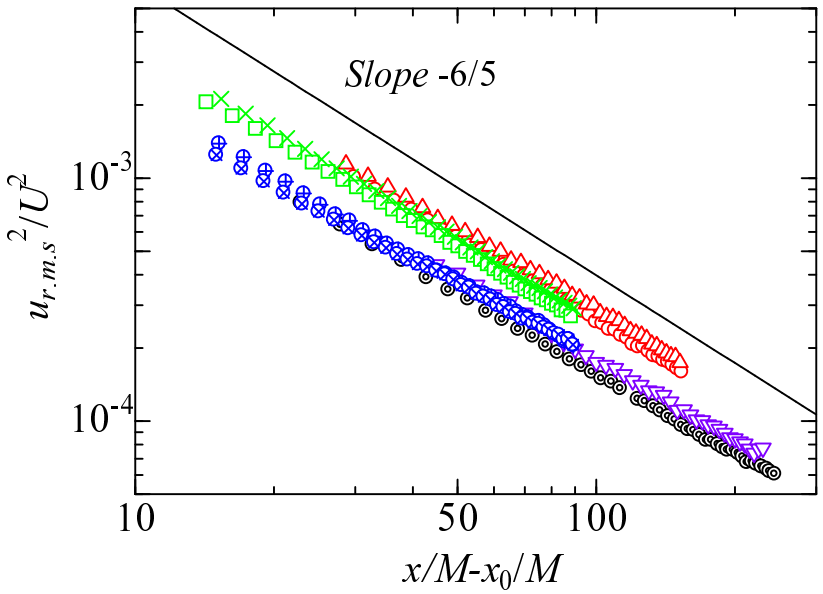

Figure 3.10: Power law decay of $u^2_{r.m.s}/U^2$. The results of Krogstad & Davidson (2010) are included as well. For symbols, see Table 3.1.

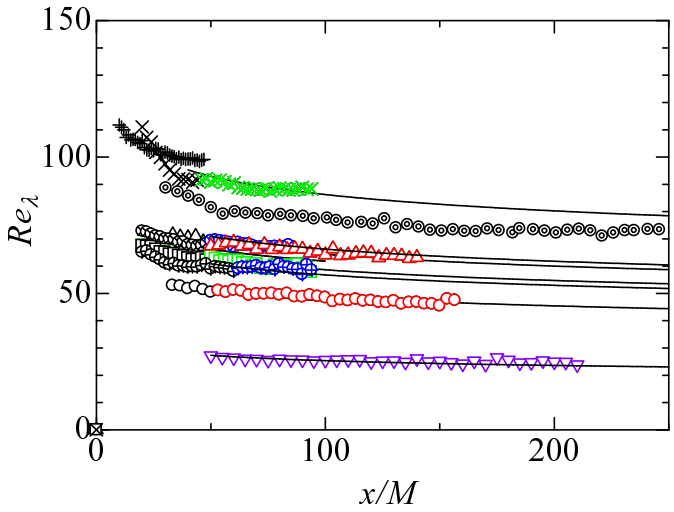

Figure 3.11: Streamwise variation in Re_λ. For symbols, see Table 3.1. The lines show $Re_\lambda \sim (x/M - x_0/M)^{-0.1}$.

in the turbulent field. For instance, $E(k \to 0) \sim k^m$ yields the TKE decay exponent $n = 2(m+1)/(m+3)$ using self-similarity and (3.19) (Sagaut & Cambon, 2008). Note that this relationship is satisfied only when A is constant. Krogstad & Davidson (2010) showed that A is a weak function of time in grid turbulence. Therefore, they concluded that the TKE decay exponent departs slightly from Saffman's theoretical value. For investigating the behaviours of A, TKE dissipation rate ϵ should be calculated with high accuracy. In homogeneous isotropic turbulence, the left side of (3.19) becomes equivalent to $\epsilon = 2\nu \langle S_{ij} S_{ij} \rangle$ from the TKE equation because there are no spatial gradients for the statistical quantities, where $S_{ij} = \frac{1}{2}\left(\frac{\partial u_i}{\partial x_j} + \frac{\partial u_j}{\partial x_i}\right)$. Additionally, ϵ is known for a physical quantity that characterises turbulence, and the following equation holds for homogeneous isotropic turbulence.

$$\epsilon = \nu \left\langle \boldsymbol{\omega}^2 \right\rangle = 2\nu \int_0^\infty k^2 E(k)\, dk = -\frac{3}{2}\frac{du_{r.m.s}^2}{dt} \tag{3.20}$$

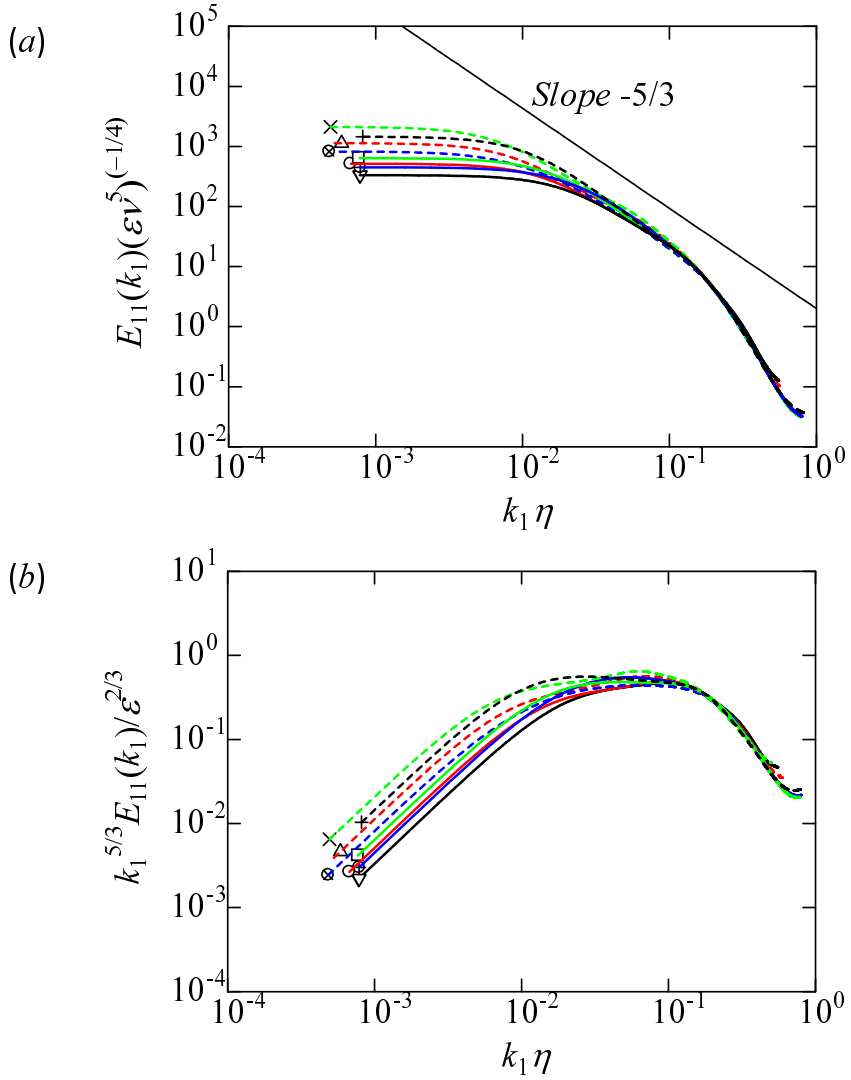

Figure 3.12: (a) One-dimensional longitudinal spectra and (b) one-dimensional longitudinal spectra multiplied by $(k_1\eta)^{5/3}$. Symbols correspond to $Cy10a$: $\triangledown$ —, $Sq15a$: $\circ$ —, $Sq15b$: $\triangle$ $\cdots$, $Cy25a$: $\oplus$ —, $Cy25b$: $\otimes$ $\cdots$, $Sq25a$: $\square$ —, $Sq25b$: $\times$ $\cdots$, $Sq50a$: $+$ $\cdots$.

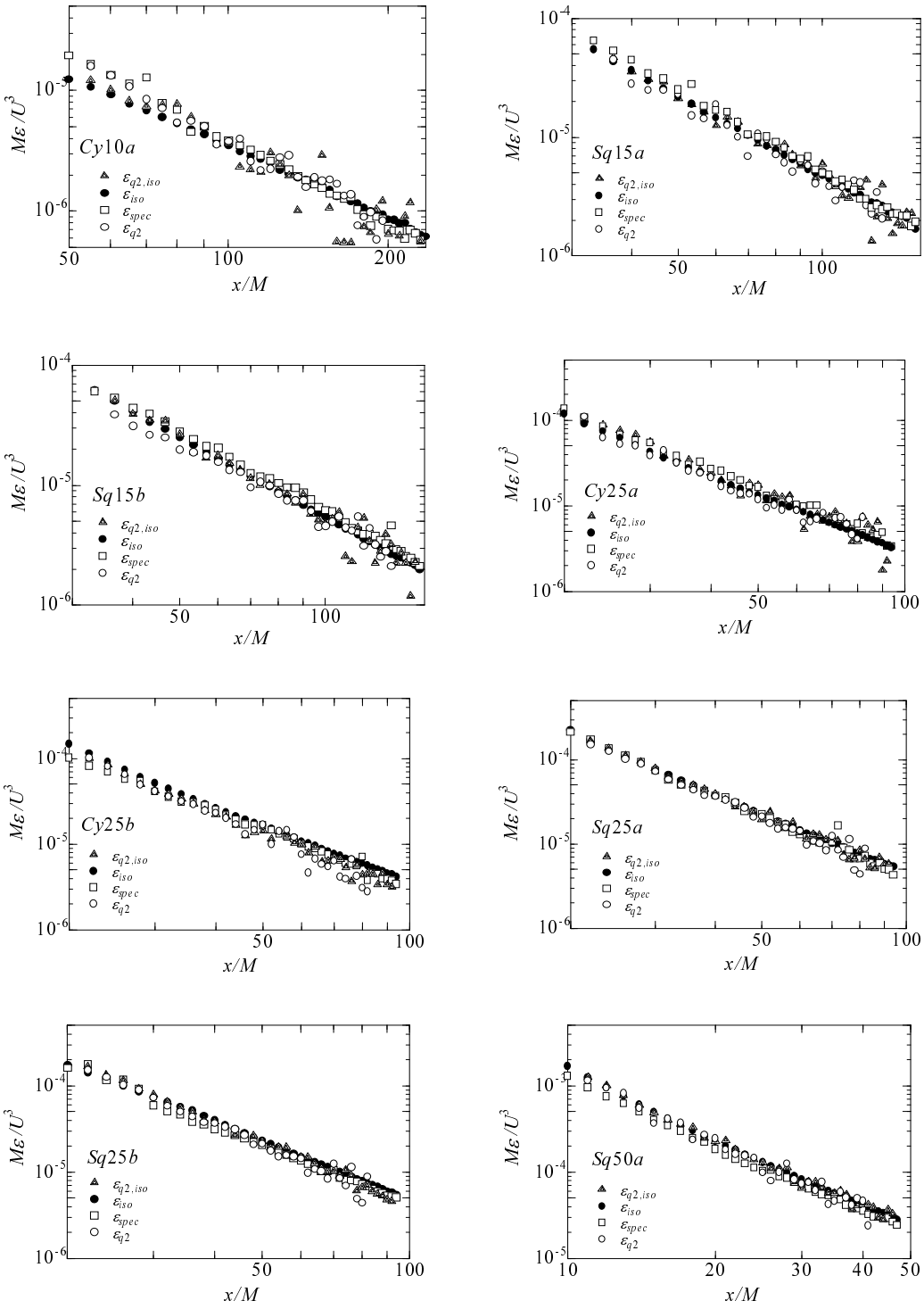

Figure 3.13: Streamwise variation in ϵ

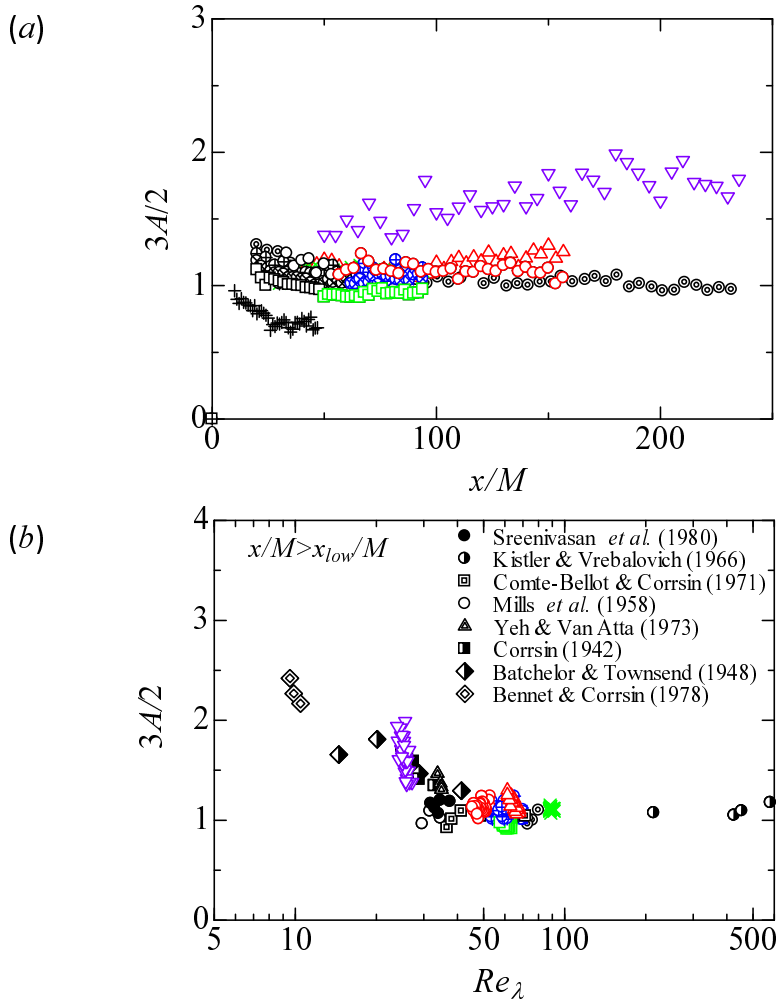

Figure 3.14: (a) Streamwise variation in A and (b) dependence of A on Re_λ in the power law decay region of $x/M > x_{low}/M$. For symbols, see Table 3.1. Also included are results from Krogstad & Davidson (2010): ◎ and grid turbulence data compiled by Sreenivasan (1984). See Sreenivasan (1984) about citations.

In the experiments, we have difficulties in calculating ϵ without any assumptions. In grid turbulence, turbulence is nearly homogeneous and isotropic, as shown before. In this study, ϵ is calculated using three methods (Krogstad & Davidson, 2010). In the first method, assuming isotropy, ϵ can be written as follows:

$$\epsilon = 15\nu \left\langle \left(\frac{\partial u}{\partial x} \right)^2 \right\rangle = 15\nu \int_0^\infty k_1^2 E_{11}(k_1)\, dk_1 \tag{3.21}$$

The estimation of ϵ by (3.21) requires only the measurement of u. This method is valid for relatively high-Reynolds-number flows. The energy dissipation rate calculated using (3.21) is denoted by ϵ_{iso}. In the second method, ϵ was calculated from TKE decay, $\epsilon = -\frac{1}{2}\frac{d\langle \boldsymbol{u}^2 \rangle}{dt} = -\frac{U}{2}\frac{d\langle \boldsymbol{u}^2 \rangle}{dx}$, using the isotropy assumption and Taylor's frozen hypothesis. The TKE dissipation rate thus calculated with the single wire is denoted by $\epsilon_{q^2,iso}$, and that calculated with the cross wire is denoted by ϵ_{q^2}. Here, we assumed $\langle \boldsymbol{u}^2 \rangle = u_{r.m.s}^2 + 2v_{r.m.s}^2$. In the third method, the universality of inertial subrange is used. Kolmogorov's second hypothesis predicts a specific form of the universal velocity spectrum called the 'inertial subrange', which is valid for wavenumbers k between the large-scale energy-containing wavenumber ($k_{L_{uu}}$) region and the small-scale viscous dissipation (k_η) region. If such a wavenumber regime exists, its spectrum will depend only on k and the energy flux from the larger to the smaller scales at the energy dissipation rate ϵ. The inertial subrange for the energy spectrum is determined from dimensional analysis:

$$E(k) = C_k \epsilon^{\frac{2}{3}} k^{-\frac{5}{3}} \text{ for } k_{L_{uu}} \ll k \ll k_\eta, \tag{3.22}$$

where C_k is the constant. For a one-dimensional longitudinal spectrum, $E_{uu}(k_1) = C_1 \epsilon^{\frac{2}{3}} k_1^{-\frac{5}{3}}$ is obtained for isotropic turbulence, where k_1 is the longitudinal wavenumber. In this study, $C_1 \approx 0.4$, as reported in the DNS results for homogeneous isotropic turbulence (Kaneda *et al.*, 2003) as well as in experiments on various types of turbulence (Sreenivasan, 1995), was adopted. Figure 3.12(a) shows the one-dimensional longitudinal spectra. It can be confirmed that the -5/3 power law in the inertial subrange expands with increasing Re_λ (with increasing Re_M). In contrast, the energy spectra for $Cy10a$ and $Sq15a$ have narrow regions exhibiting the -5/3 power law because of relatively low Re_λ. Thus, we used the

profiles multiplied by $(k_1\eta)^{\frac{5}{3}}$ (figure 3.12b) to calculate the value of ϵ. The TKE dissipation rate calculated using the third method is denoted by ϵ_{spec}. Figure 3.13 shows the streamwise variation in ϵ calculated using the three methods. As shown in figure 3.13, we can see good agreement among ϵ_{iso}, $\epsilon_{q^2,iso}$, ϵ_{q^2} and ϵ_{spec}. Thus, it is considered that local isotropy is satisfied. In this study, ϵ_{iso} was used for calculating A because of the lowest scatter.

Streamwise variations in A are shown in figure 3.14(a). Here, A is calculated as follows:

$$\frac{3A}{2} = \frac{\epsilon L_{uu}}{u_{r.m.s}^3}. \tag{3.23}$$

With the exception of $Cy10a$, A is a decreasing function in the upstream region. This tendency is consistent with the results of Krogstad & Davidson (2010). However, in the downstream region of $x/M > x_{low}/M$, where turbulence is fully developed and freely decaying, A is almost constant except for $Cy10a$. Variations in A against Re_λ are shown in figure 3.14(b). Here, the data in the power law decay region (i.e. $x/M > x_{low}/M$) are plotted. The results of Krogstad & Davidson (2010) and the data of grid turbulence compiled by Sreenivasan (1984) are also shown in figure 3.14(b). As shown in this figure, we could confirm good agreement with previous grid turbulence results: A tends to become constant with increasing Re_λ.

In contrast, A is a function of time even for fully developed turbulence when Re_λ is low (for $Cy10a$ in this study). This tendency was also observed in a DNS (Kaneda *et al.*, 2003). In this case, the TKE decay and the evolution of the integral length scale are represented by (3.24) and (3.25) when Saffman's integral is constant (Krogstad & Davidson, 2010).

$$\frac{u_{r.m.s}^2}{u_0'^2} = \left[1 + \frac{5}{6}\frac{u_{r.m.s0}}{L_{uu0}}\int_0^t A\,(t)\,dt\right]^{-\frac{6}{5}} \tag{3.24}$$

$$\frac{L_{uu}}{L_{uu0}} = \left[1 + \frac{5}{6}\frac{u_{r.m.s0}}{L_{uu0}}\int_0^t A\,(t)\,dt\right]^{\frac{2}{5}} \tag{3.25}$$

If A is a power function of time, $A(t) \sim t^p$, the following equations can be derived (Krogstad & Davidson, 2010).

$$u^2_{r.m.s} \sim t^{-\frac{6}{5}(1+p)} \tag{3.26}$$

$$L_{uu} \sim t^{\frac{2}{5}(1+p)} \tag{3.27}$$

For $Cy10a$, $p \sim 0.1$ is determined using the least squares method. Note that $p \approx 0$ for other cases at $x/M > x_{low}/M$ (see figure 3.14(a)). Thus, $u^2_{r.m.s} \sim t^{-1.32}$ and $L_{uu} \sim t^{0.44}$ correspond to Saffman turbulence for $Cy10a$.

3.4.4 Length scales

In grid turbulence, λ^2 is linearly proportional to distance if the TKE power law decays following (3.17) and isotropy is satisfied (e.g. this assumption corresponds to (3.20)). Further, appling Taylor frozen hypothesis, we obtain:

$$\lambda^2 = \frac{u^2_{r.m.s}}{\left\langle (\partial u/\partial x)^2 \right\rangle} = 15\nu \frac{u^2_{r.m.s}}{\epsilon} = -\frac{10\nu}{U} \frac{u^2_{r.m.s}}{du^2_{r.m.s}/dx} = \frac{10\nu}{Un}(x - x_0)\,. \tag{3.28}$$

When $n = 6/5$ for Saffman turbulence is applied to (3.28),

$$\frac{\lambda^2}{M^2} = \frac{25}{3Re_M}\left(\frac{x}{M} - \frac{x_0}{M}\right). \tag{3.29}$$

When Saffman's integral is constant and $A(t) \sim t^p$ is compensated for, L_{uu} and L_{vv} are represented by

$$\frac{L_{uu}}{M} \propto \frac{L_{vv}}{M} \propto \left(\frac{x}{M} - \frac{x_0}{M}\right)^{\frac{2}{5}(1+p)}. \tag{3.30}$$

Similarly, λ is represented by

$$\frac{\lambda^2}{M^2} = \frac{25}{3Re_M(1+p)}\left(\frac{x}{M} - \frac{x_0}{M}\right). \tag{3.31}$$

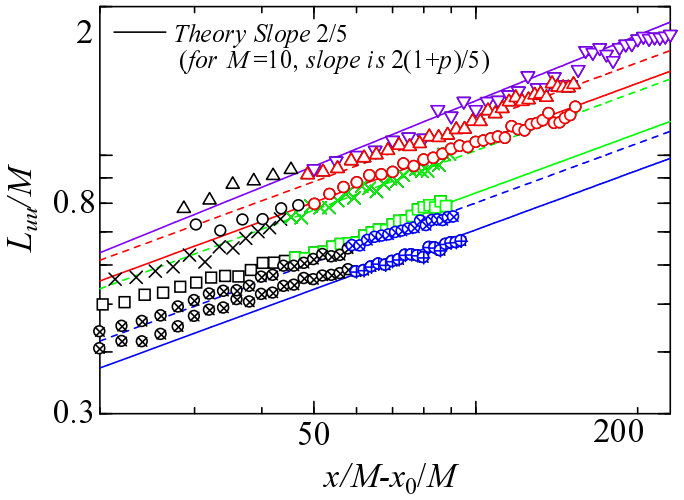

Figure 3.15: Streamwise variation in L_{uu}/M. For symbols, see Table 3.1. The lines show the theoretical slope 2/5 (for $Cy10a$, slope is $2\,(1+p)\,/5$).

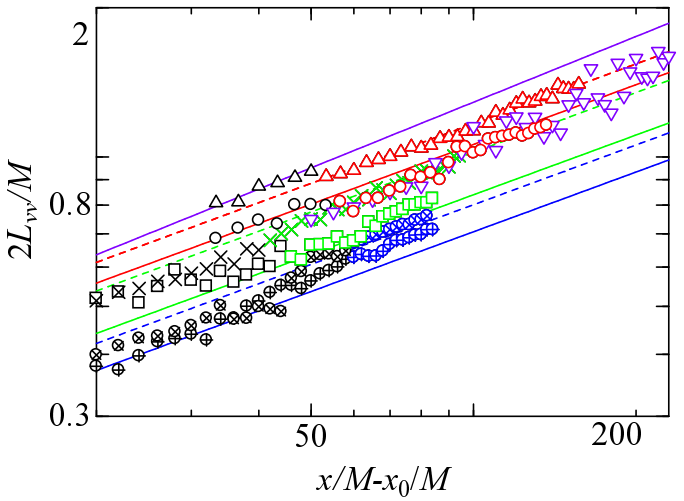

Figure 3.16: Streamwise variation in $2L_{vv}/M$. For symbols, see Table 3.1. The lines are the same as those in figure 3.15.

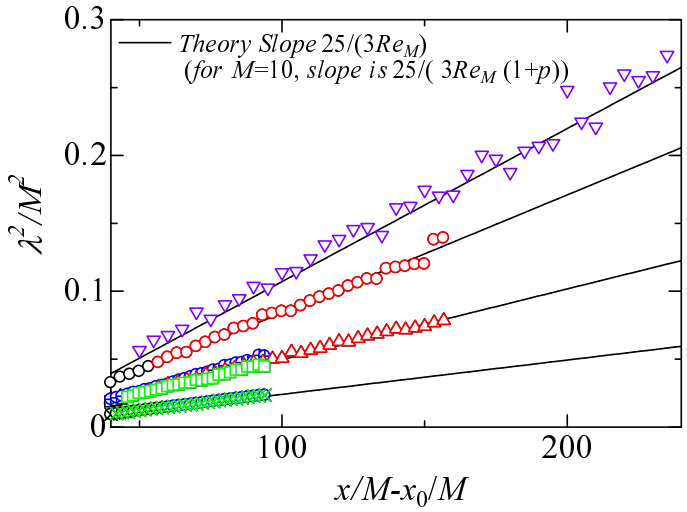

Figure 3.17: Streamwise variation in λ^2/M^2. For symbols, see Table 3.1.

The streamwise variations in L_{uu}, L_{vv} and λ^2 are shown in figures 3.15, 3.16 and 3.17, respectively. Figures 3.15 and 3.16 show that L_{uu} and L_{vv} grow according to (3.30) for Saffman turbulence. Note that isotropic relationships, i.e. $L_{uu} = 2L_{vv}$, are confirmed except for $Cy10a$, which is a slightly anisotropic case. Similar observations were also made by Antonia *et al.* (2003), who showed that $L_{uu} \sim L_{vv} \sim t^{\frac{2}{5}}$; however, in their case, L_{uu}/L_{vv} was 2.75. For $Cy10a$, which is the most anisotropic case in this study, this ratio is about 2.5. Figure 3.17 shows that λ^2 grows linearly and that the profiles are well described by (3.31) for Saffman turbulence.

3.4.5 Invariants

The invariants $u^2_{r.m.s}L^3_{uu}$ and $v^2_{r.m.s}L^3_{vv}$ corresponding to Saffman turbulence are shown in figures 3.18 and 3.19, and the invariants $u^2_{r.m.s}L^5_{uu}$ and $v^2_{r.m.s}L^5_{vv}$ corresponding to Batchelor turbulence are shown in figures 3.20 and 3.21, respectively. Here, the invariants are normalised using U and M. Figures 3.18 and 3.19 show that Saffman's integral becomes invariant regardless of grid geometry and exam-

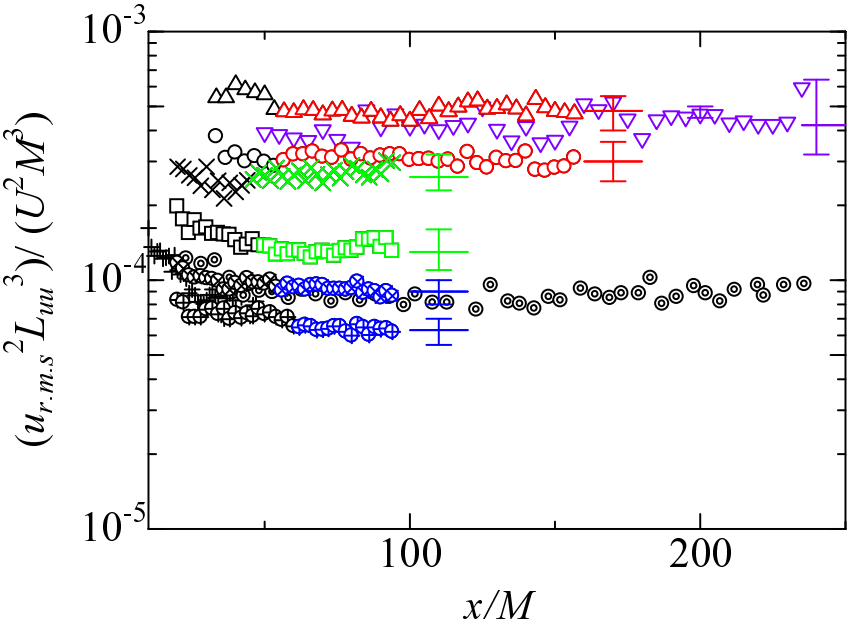

Figure 3.18: Streamwise variation in normalised $u_{r.m.s}^2 L_{uu}^3$. The results of Krogstad & Davidson (2010): ◎ are also included. For symbols, see Table 3.1.

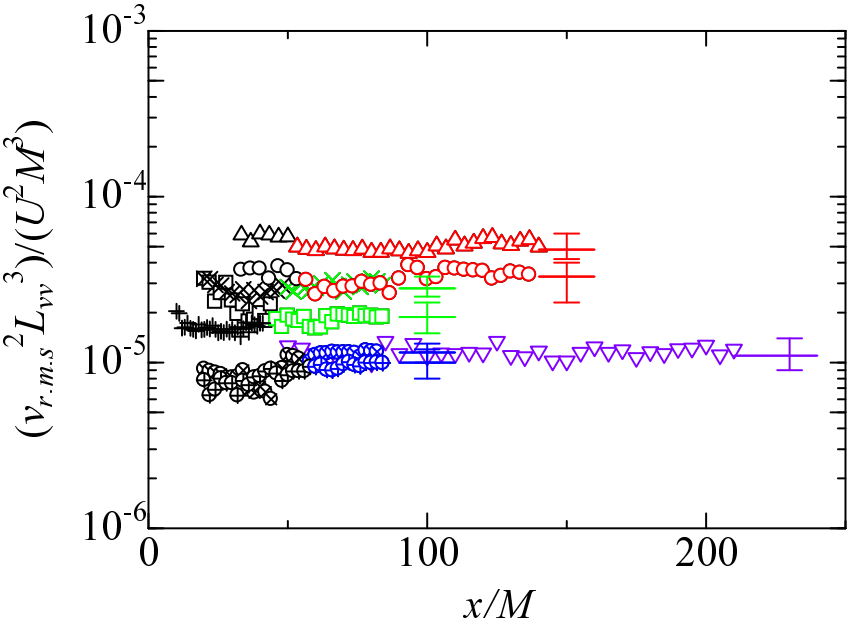

Figure 3.19: Streamwise variation in normalised $v_{r.m.s}^2 L_{vv}^3$. For symbols, see Table 3.1.

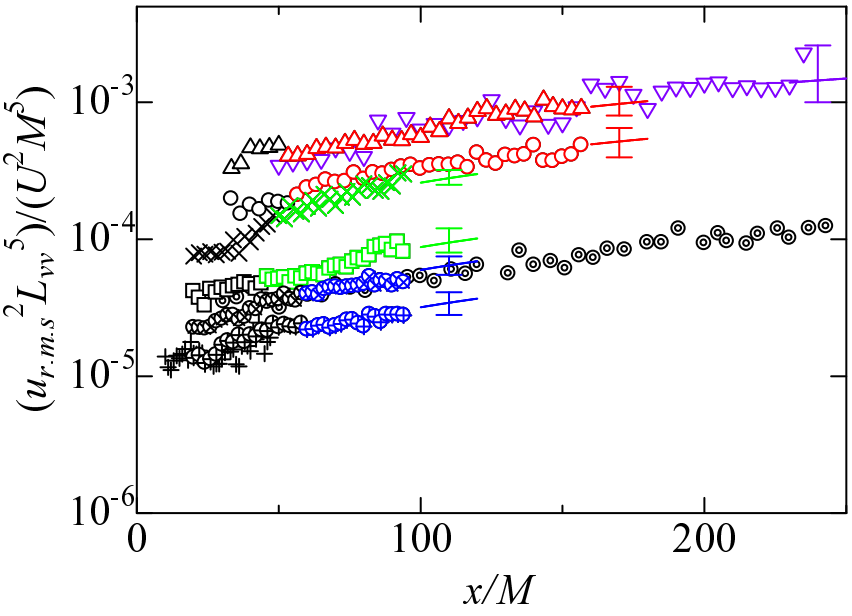

Figure 3.20: Streamwise variation in normalised $u_{r.m.s}^2 L_{uu}^5$. For symbols, see Table 3.1.

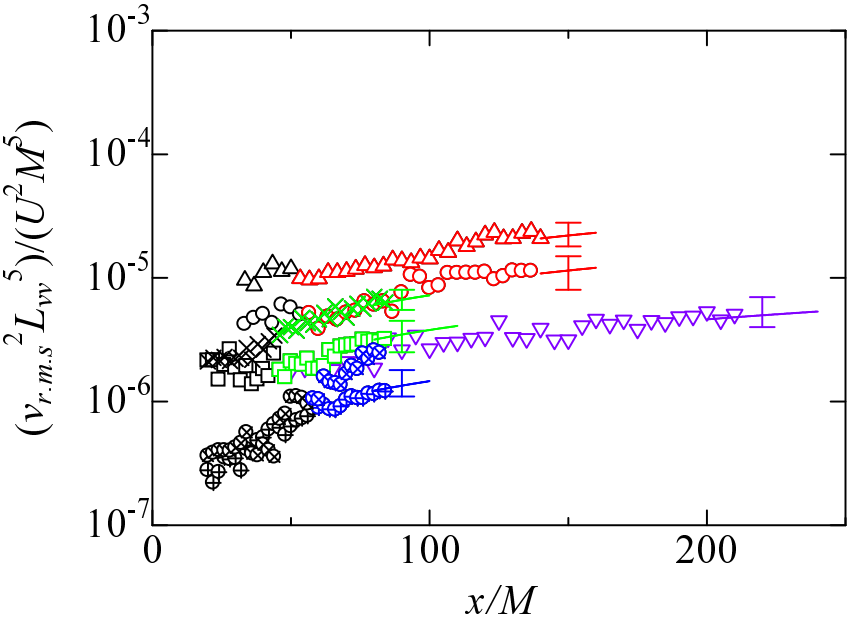

Figure 3.21: Streamwise variation in normalised $v_{r.m.s}^2 L_{vv}^5$. For symbols, see Table 3.1.

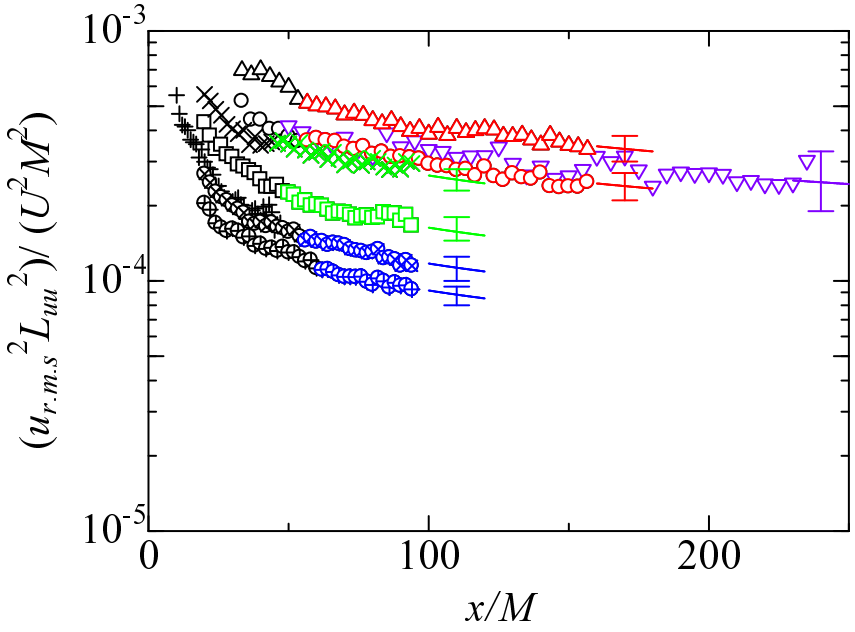

Figure 3.22: Streamwise variation in normalised $u^2_{r.m.s}L^2_{uu}$. For symbols, see Table 3.1.

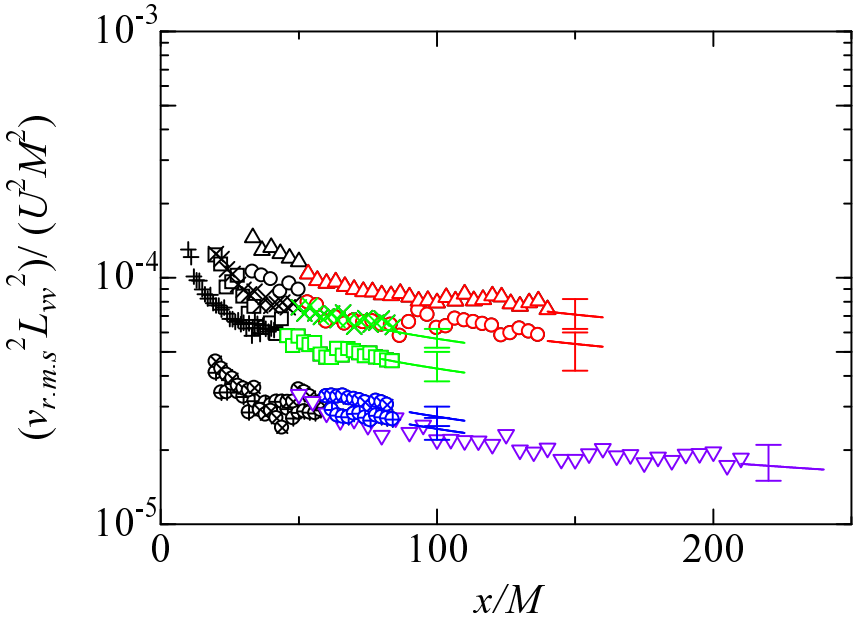

Figure 3.23: Streamwise variation in normalised $v^2_{r.m.s}L^2_{vv}$. For symbols, see Table 3.1.

ined Re_M. In addition, it is shown that for the same grid geometry and same Re_M (i.e. comparison of $Sq15b$ and $Sq25a$), normalised $u^2_{r.m.s}L^3_{uu}$ and $v^2_{r.m.s}L^3_{vv}$ are larger for small M. In contrast, for different grid geometries and the same Re_M (i.e. comparisons of $Cy25a$ and $Sq25a$, $Cy25a$ and $Sq25b$), normalised $u^2_{r.m.s}L^3_{uu}$ and $v^2_{r.m.s}L^3_{vv}$ for the cylindrical grids are smaller than those for the square grids. For the same M and grid geometry (i.e. comparisons of $Sq15a$ and $Sq15b$, $Cy25a$ and $Cy25b$, $Sq25a$ and $Sq25b$), normalised $u^2_{r.m.s}L^3_{uu}$ and $v^2_{r.m.s}L^3_{vv}$ are larger for large Re_M.

Then, it is suggested from TKE decay that the region where $u^2_{r.m.s}L^3_{uu}$ and $v^2_{r.m.s}L^3_{vv}$ become constant is farther for the cylindrical grids than that for the square grids. This is probably due to the difference in the wake development processes of these grids, and it is considered that the turbulence generated by square grids is better mixed than that generated by the cylindrical grids. Saffman (1967) predicted that the linear impulse would be zero if the turbulent wake of the grids were to retain a periodic structure. Although turbulent flows generated by grids have a periodic structure near the grids, mixing takes place gradually, and the flows change to fully developed turbulent fields. Thus, it is possible that periodic structures do not exist permanently in the Re_M range used herein. Therefore, this presents the possibility that grid turbulence at moderate Re_λ could be Saffman turbulence. In contrast, figures 3.20 and 3.21 show that Loitsianskii's integrals do not become invariant.

Finally, the invariants $u^2_{r.m.s}L^2_{uu}$ and $v^2_{r.m.s}L^2_{vv}$, which correspond to complete self-similarity of the energy spectrum and $\langle \boldsymbol{u}^2 \rangle \sim t^{-1}$, are shown in figures 3.22 and 3.23, respectively. From these figures, it is shown that $u^2_{r.m.s}L^2_{uu}$ and $v^2_{r.m.s}L^2_{vv}$ are not constant in the decay region.

These results are consistent with the conclusions of Krogstad & Davidson (2010). In this study, the same conclusion as that of Krogstad & Davidson (2010) was obtained for a wide range of M and Re_M values for both the cylindrical and square grid bars. These results support the hypothesis that grid turbulence is a type of Saffman turbulence at moderate Re_λ.

3.5 Conclusions

The energy decay characteristics and invariants of grid turbulence were investigated for five grids (square bars with mesh sizes M = 15, 25 and 50 mm and cylindrical bars with mesh sizes M = 10 and 25 mm) and four mesh Reynolds numbers (Re_M = 6700, 9600, 16000 and 33000). The main results of this study are as follows.

1. Decay exponents of TKE in grid turbulence are close to Saffman's theoretical value of $\frac{6}{5}$ (for the M = 10 mm grid, $\frac{6}{5}(1+p) \sim 1.32$) in all cases. There are almost no differences in the TKE decay exponents of different grid geometries (i.e. square, cylindrical). However, turbulence generated by cylindrical grids tends to develop fully at further distances than that generated by square grids.

2. In the fully developed region, the integral length scales L_{uu} and L_{vv} grow according to $L_{uu} \sim 2L_{vv} \propto (x/M - x_0/M)^{2/5}$ (for the M = 10 mm grid, $L_{uu} \propto (x/M - x_0/M)^{\frac{2}{5}(1+p)} \sim (x/M - x_0/M)^{0.44}$), and the Taylor microscale λ grows according to $\lambda \propto (x/M - x_0/M)^{\frac{1}{2}}$.

3. $u^2_{r.m.s}L^3_{uu}$ and $v^2_{r.m.s}L^3_{vv}$, which correspond to Saffman's integral, become constant in the energy decay region in all cases, regardless of grid geometry. However, the region where $u^2_{r.m.s}L^3_{uu}$ and $v^2_{r.m.s}L^3_{vv}$ become constant is farther for the cylindrical grids than that for the square grids. Then, $u^2_{r.m.s}L^3_{uu}$ and $v^2_{r.m.s}L^3_{vv}$ are conserved. In contrast, $u^2_{r.m.s}L^5_{uu}$ and $v^2_{r.m.s}L^5_{vv}$, which correspond to Loitsianskii's integral, and $u^2_{r.m.s}L^2_{uu}$ and $v^2_{r.m.s}L^2_{vv}$, which correspond to the complete self-similarity of the energy spectrum, do not become constant at moderate Reynolds numbers.

These results suggest that the grid turbulence generated by a square or a cylindrical grid is a type of Saffman turbulence for the Re_M range of 6700–33000 (Re_λ = 27–112).

Chapter 4

Changes in grid turbulence interacting with a weak shock wave

4.1 Introduction

A lot of efforts have been devoted to clarify the mechanism of the interaction between turbulence and a shock wave. However, the physical mechanism for each change in physical quantities has not been well understood because of the complex linear and nonlinear effects, in which turbulence has an impact on a shock wave, and vice versa.

Previous studies (see §1.1.2.1 and §1.1.2.2) have reached an agreement that the shock wave amplifies turbulence kinetic energy (TKE). However, further investigation is required with regard to the changes in the length scales because previous results are not consistent. In addition, previous studies mainly focus on the interaction between high–Mach–number turbulence and a shock wave and few studies focus on the interaction between low-Mach-number turbulence and a shock wave. The former studies are important in advances in combustion process and space physics, whereas the latter is directly related with a sonic boom problem, in which a shock wave propagates in the atmosphere. In addition, it is expected that the difference in turbulent Mach-number yields the different changes in turbulent characteristics after the interaction. In fact, Briassulis *et al.*

(2001) concluded that the growth rate of shear layers in a high-Mach-number flow is different from that in a low-Mach-number flow. Wang *et al.* (2012) showed by DNS that the magnitude of the derivative skewness is larger than 1 in high-Mach-number turbulence, and this is much larger than that in low-Mach-number turbulence. This indicates that the impact of a shock wave on other turbulence characteristics can be different between in high- and low-Mach-number turbulence. In other words, the turbulent Mach-number plays an important role on the turbulence-shock wave interaction.

In this study, changes in turbulence characteristics after the interaction with a weak shock wave are experimentally investigated in low-Mach-number (i.e. divergence-free) turbulence. To the best of my knowledge, there is no study on the changes in divergence-free turbulence interacting with a shock wave. The purpose of the present study is to obtain reliable experimental data in divergence-free grid turbulence after the interaction. Furthermore, we try to explain the change in turbulence from the viewpoint of initial turbulent Mach number (i.e. initially divergence-free or curl-free turbulence).

4.2 Experiments

4.2.1 Experimental apparatus

The experiments were conducted in a closed-loop wind tunnel at Nagoya University, the same as that used in §3. A shock wave is generated by a diaphragm-less shock tube using a quick piston valve and emitted from the open end of the shock tube, which is located at $(x, y, z) = (1500\ \text{mm}, 0, 275\ \text{mm})$ and directed vertically downward across the turbulent flow (figure 4.1 (a)). This shock tube was modified from the previous study (Sasoh *et al.*, 2014) and is redesigned to generate stronger shock wave. The deriven section of the shock tube which is with an atmospheric pressure has a total length of 3565 mm and 21.3 mm in inner diameter. Dry air is charged into the driver air reservoir to avoid freezing of water.

The differential pressure between low and high pressure rooms is set to 900 kPa. Shock Mach-number in the shock tube is calculated by $M_s = D/\Delta t/C_0$, where Δt is the time concerning a shock wave passing the distance D and C_0

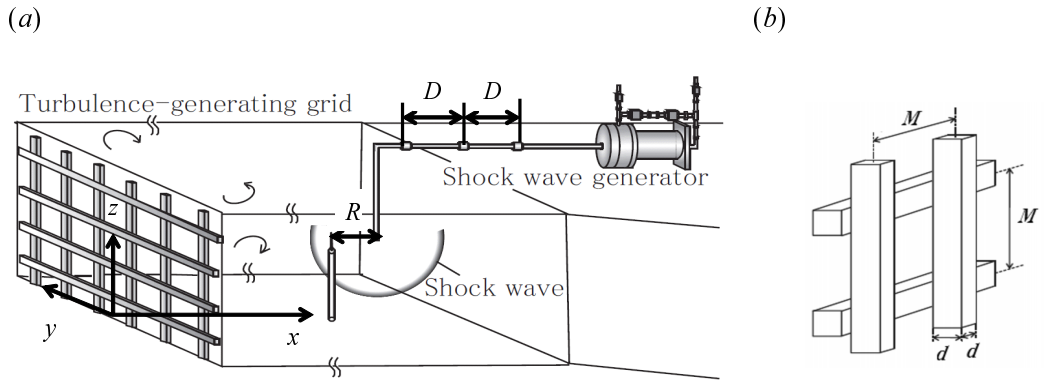

Figure 4.1: Schematic view of (a) the experimental apparatus combining the wind tunnel and shock wave generator and (b) the square grid. Here, $R = 600$ mm is the distance from the open end of the shock wave generator to the hot–wire.

is the sound speed. In the present study, Δt is estimated from pressure signals measured by two piezoelectric pressure tranducers (H112A21, PCB Piezotronics Inc., the sensitivity is 7.25 mV/kPa and rise time is less than 2.0 μs), which are set up in the shock tube with a distance $D = 430$ mm. The results after 100 measurements show that the average shock Mach-number M_{sAve} is 1.617 with a standard deviation of 0.002, while theoretical value is 1.608. Thus the present experimental system has quantitatively sufficient reliability and repeatability.

Turbulence was generated by grids (figure 4.1 (b)) installed at the entrance of the test section shown in figure 4.1 (a). Here, M is the grid mesh size and d is the thickness of the grid. The grid solidity is $\sigma = 0.36$ for all the grids. Coordinates x, y and z refer to the downstream, spanwise and vertical directions, respectively, with the origin being at the base of the test section's entrance.

4.2.2 Experimental conditions and methods

The experimental conditions of grid turbulence are summarized in Table 4.1. The mesh Reynolds numbers were set to $Re_M = U_{mean}M/\nu = 9600$, 16700, 20000, 33000, 60000 and 66700, where U_{mean} is the mean velocity and ν is the kinematic viscosity. Here, M_U ($= U_{mean}/C_0$) and M_t ($= u_{r.m.s}/C_0$) are the Mach num-

ber based on the mean velocity and the turbulent Mach number, respectively. $Re_\lambda = u_{r.m.s}\lambda/\nu$ is the Reynolds number based on the Taylor microscale λ and L is the streamwise integral length scale defined by the integration of autocorrelation function. Here, the Taylor's frozen hypothesis was used for calculating λ and L. The characteristics of the shock wave were investigated by using three piezoelectric pressure tranducers with acceleration compensation (113B28, PCB Piezotronics Inc., the sensitivity is 14.5 mV/kPa and the rise time is 1 μs.), located at (x, y, z) = (925 mm, 0, 0), (1025 mm, 0, 0) and (1130 mm, 0, 0). The hot wire was placed at (x, y, z) = (900 mm, 0, 275 mm). A shock wave propagates spherically from the open end. The shock Mach-number at the probe location estimated from the geometrical condition is about 1.05 and it is fixed in all flows. We also confirmed the propagation of the shock wave by means of Schlieren photography.

Instantaneous streamwise velocity is measured by using hot wire anemometry (DANTEC Streamline) with an I-type hot wire probe (DANTEC 55P11). The diameter of the wire was 5 μm and its length was 1.25 mm. The wire was calibrated in the wind tunnel and the instantaneous streamwise velocity was calculated by King's law. The sampling rate was set to 100 kHz. The frequency response of the single wire was found to be approximately 60 kHz and 100 kHz for $U_{mean} \sim 10$ ms^{-1} and 20 ms^{-1}, respectively. The experiments were performed 250 times for each condition in order to obtain reliable statistics.

4.3 Results and Discussion

4.3.1 The characteristics of the shock wave

Figure 4.2 shows several examples of overpressure histories without a flow in 200 trials at different locations. When the shock wave reflects the pressure transducer, the overpressure is suddenly increased. Then, the overpressure decreases due to the expansion fan and further decreases down to a negative value. The overpressure starts to recover toward the atmospheric value. This tendency was also similar to the overpressure history of laser induced blast wave (Liang *et al.*, 2001). It is confirmed that there is no device oscillation as seen in the previous

Table 4.1: Experimental Conditions of the initial turbulent fields, also included are the lowest Mach number conditions in the experiments of Keller & Merzkirch (1990) and Agui *et al.* (2005). Note that L and λ in Keller & Merzkirch (1990) are the length scales for scalar. The grid used by Keller & Merzkirch (1990) is a punched plate and different from ours. Therefore the mesh size written in this table is the effective mesh size, which is equivalent to the squared mesh size.

	M [mm]	x/M	Re_M	Re_λ	M_U	L/M	λ/M	$M_t \times 10^3$
Case 1	15	60	9600	49	0.029	0.583	0.205	0.709
Case 2	15	60	20000	70	0.051	0.864	0.157	1.330
Case 3	25	36	16700	64	0.029	0.450	0.125	0.910
Case 4	25	36	33300	92	0.051	0.520	0.087	1.874
Case 5	50	18	33300	105	0.029	0.250	0.057	1.617
Case 6	50	18	60000	148	0.051	0.367	0.047	2.803
Case 7	100	9	66700	159	0.029	0.162	0.026	2.660
Keller & Merzkirch (1990)	7.1	–	35000	–	0.181	0.465	0.338	–
Agui *et al.* (2005)	3.18	–	37000	162	0.371	–	–	–

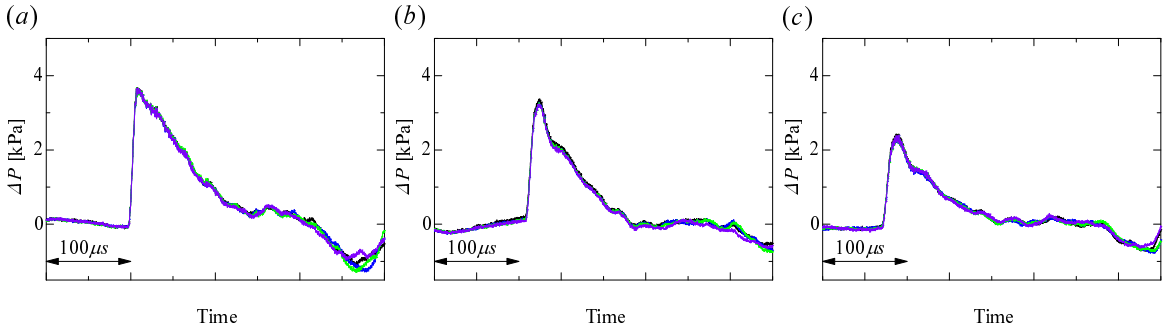

Figure 4.2: Examples of pressure waveforms without a flow at locations (*a*) $(x, y, z) = (1130 \text{ mm}, 0, 0)$, (*b*) $(x, y, z) = (1025 \text{ mm}, 0, 0)$ and (*c*) $(x, y, z) = (925 \text{ mm}, 0, 0)$. These figures include the four randomly selected overpressure histories in 200 experiments.

study (Sasoh *et al.*, 2014) in the overpressure histories. This is due to the increase of overpressure strength. Figures 4.3 and 4.4 show overpressure histories with turbulence in the strongest and weakest shock waves for cases 1 and 7, respectively. The difference of the peak value in the strongest and weakest cases is more significant at $x = 1025$ and 925 mm, where turbulence is stronger (larger Re_λ), than that at $x = 1130$ mm. Furthermore, we cannot see clear difference in the arrival time in spite of the fact that there are clear differences in the peak of overpressure and turbulence characteristics such as Re_λ.

Figure 4.5 shows the variation of peak values of the overpressure in 200 experiments. It increases with Re_λ, indicating that stronger turbulence causes larger impact on the pressure history behind the shock wave.

4.3.2 The variations of turbulence quantities

Figure 4.6 shows the instantaneous velocity signal before and after the interaction for cases 1 and 7. The velocity signal after the interaction exhibits drastic changes characterized by bursts of highly intermittent events. Similar results can be seen in the experiments of Agui *et al.* (2005). The instantaneous velocity signals have discontinuity when the shock wave passed the probe. This tendency was seen in

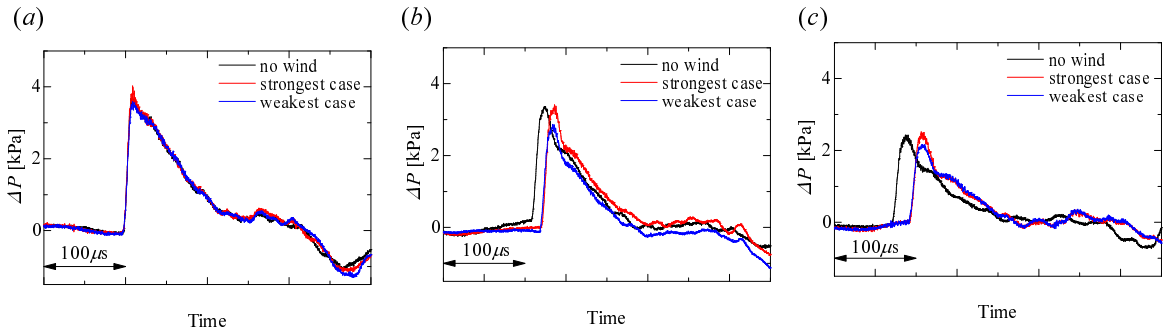

Figure 4.3: Examples of pressure waveforms interacting with grid turbulence for case 1 at locations (a) $(x, y, z) = (1130$ mm, 0, 0), (b) $(x, y, z) = (1025$ mm, 0, 0) and (c) $(x, y, z) = (925$ mm, 0, 0). Black line corresponds to the pressure waveform without a flow, and red and blue lines correspond to pressure waveform in the strongest and weakest cases, respectively.

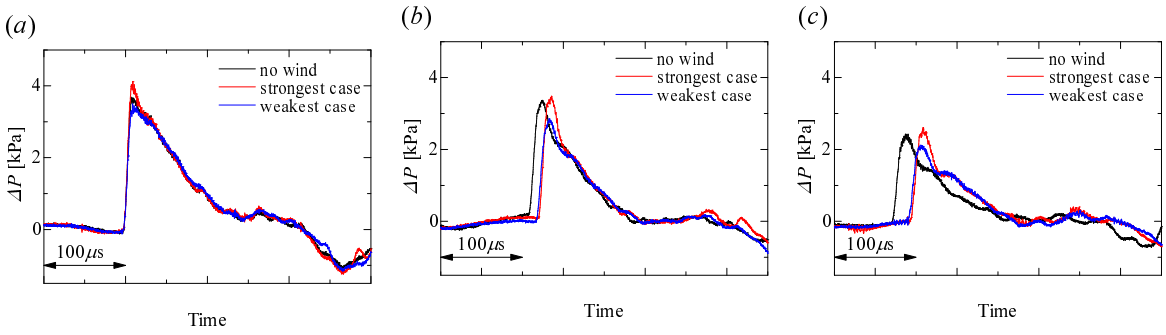

Figure 4.4: Same as figure 4.3 but for case 7.

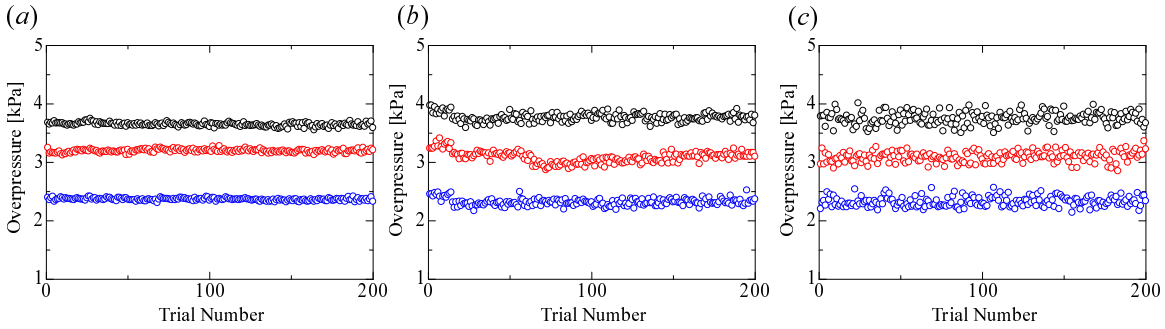

Figure 4.5: Variation of peak value of the overpressure in the case (a) without a flow, (b) case 1, and (c) case 7. Black, red and blue circles correspond to the overpressures at locations (x, y, z) = (1130 mm, 0, 0), (x, y, z) = (1025 mm, 0, 0), and (x, y, z) = (925 mm, 0, 0), respectively.

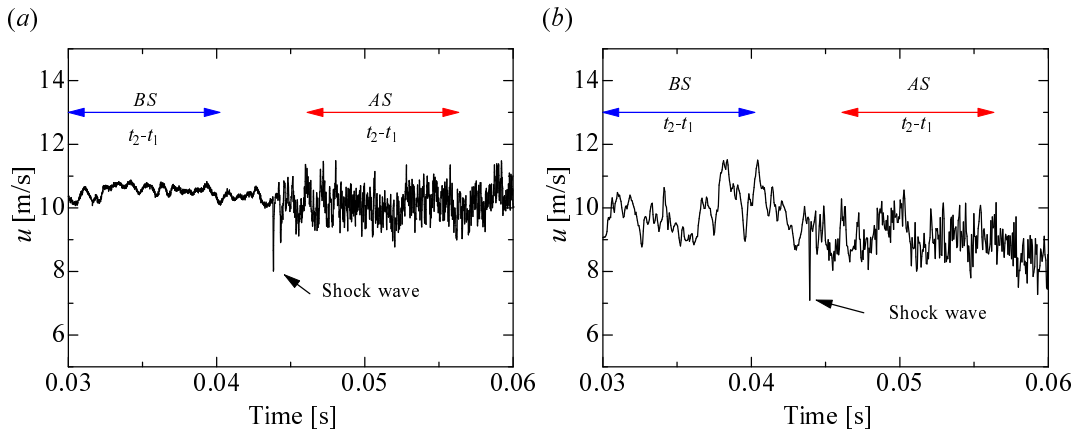

Figure 4.6: Examples of instantaneous velocity signal before and after the shock wave passage in (a) case 1 and (b) case 7 at the 600 mm upstream measurement from the open end of the shock wave generator. Here, BS and AS represent the analysis region before and after the interaction with the shock wave, respectively.

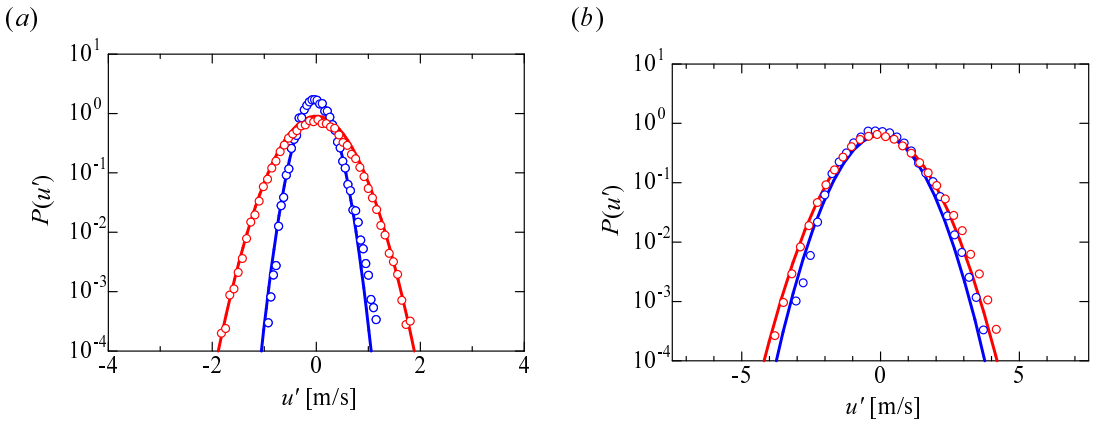

Figure 4.7: Probability density function (pdf) of streamwise velocity fluctuation u', $P(u')$, for case 1 (a) and case 7 (b). The blue and red circles are the pdfs of u' before and after the interaction, respectively. The blue and red solid lines represent Gaussian fit for $P(u')$ before and after the interactions, respectively.

all cases.

Figure 4.7 shows the probability density function (pdf) of the streamwise velocity fluctuation u'. The both pdfs are close to Gaussian regardless of the interaction.

The root mean square value of streamwise velocity fluctuation $u_{r.m.s}$ was evaluated as an ensemble average of time series data as follows:

$$u_{r.m.s}^2 = \frac{1}{N}\sum^{N}\frac{1}{t_2 - t_1}\int_{t_1}^{t_2}\left[u(t) - U_{ENS}\right]^2 dt,\ U_{ENS}(t) = \frac{1}{N}\sum^{N} u(t) \qquad (4.1)$$

where U_{ENS} is the ensemble averaged velocity over 250 ($= N$) experiments, t_1 and t_2 are starting and ending times of the analyzed signal, respectively. Here, $t_2 - t_1 = 0.01024$ s, which is longer than the turbulent characteristic time scale, e.g. L/U_{mean} and see table 4.1. Note that for $U_{mean} \sim 10$ ms^{-1}, turbulence travels about 0.1 m during the period. Using the linear extrapolation, shock-Mach-number at an upstream location by 0.1 m is approximately $M_s \approx 1.04$, which is a 1% reduction compared to $M_s \approx 1.05$ at the probe location. The relationship between the ratio of $u_{r.m.s}$ before (subscript BS) and after (subscript

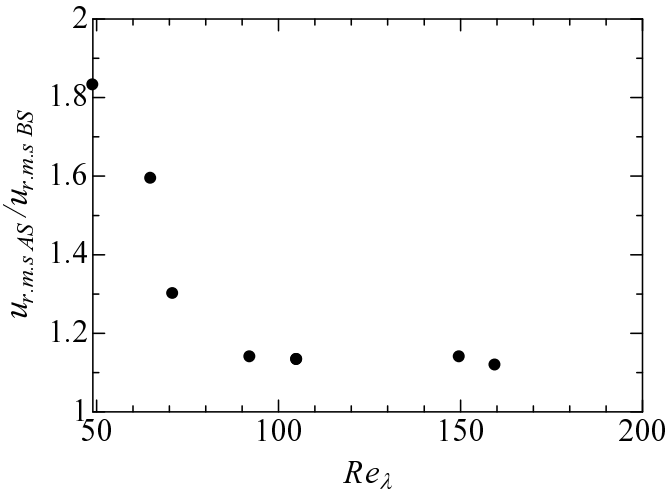

Figure 4.8: The ratio of $u_{r.m.s}$ before and after the interaction against Re_λ.

AS) the interaction and Re_λ is shown in figure 4.8. It is found that $u_{r.m.s}$ increases and the amplification is larger for small Re_λ.

The ratio of the streamwise integral length scales L before and after the interaction is plotted against Re_λ in figure 4.9. L decreases after the interaction and the reduction is more significant for small Re_λ. The result is consistent with Agui *et al.* (2005), Barre *et al.* (1996) and the results of DNS (Hannappel & Friedrich, 1995; Lee *et al.*, 1993), but is different from Keller & Merzkirch (1990) for integral length scale of density fluctuations. As to this difference, further studies including the changes in scalar will be needed.

4.3.3 Continuous wavelet analysis

Wavelet transform is a powerful tool to investigate phenomena involving changes in time and frequency (scale or wavenumber) such as turbulence-shock wave interaction. Continuous wavelet transform is defined as

$$T(a,b) = \frac{1}{\sqrt{a}} \int_{-\infty}^{\infty} dt\; u(t)\, \psi^* \left(\frac{t-b}{a} \right), \tag{4.2}$$

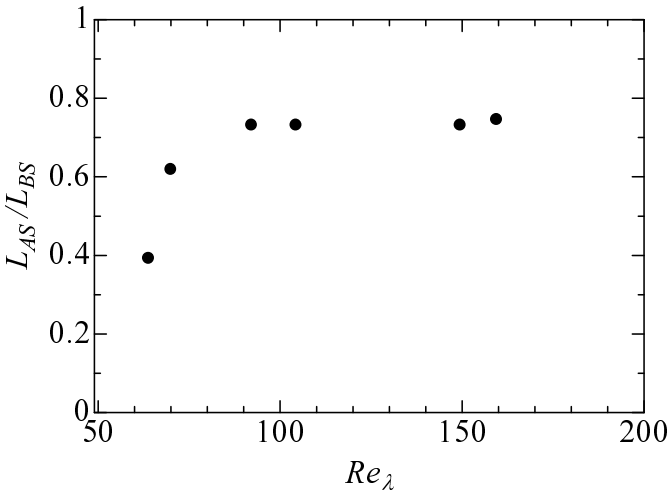

Figure 4.9: The ratio of L before and after the interaction against Re_λ.

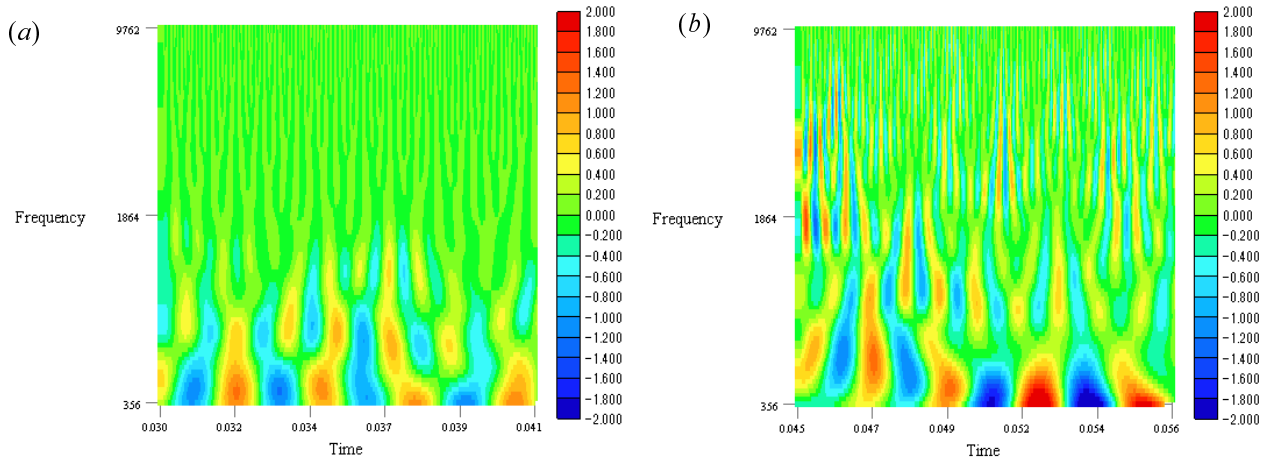

Figure 4.10: Continuous wavelet analysis for case 1 (a) before and (b) after the interaction. The real part of Morlet wavelet is shown. Here, we cannot see outstanding difference for imaginary part.

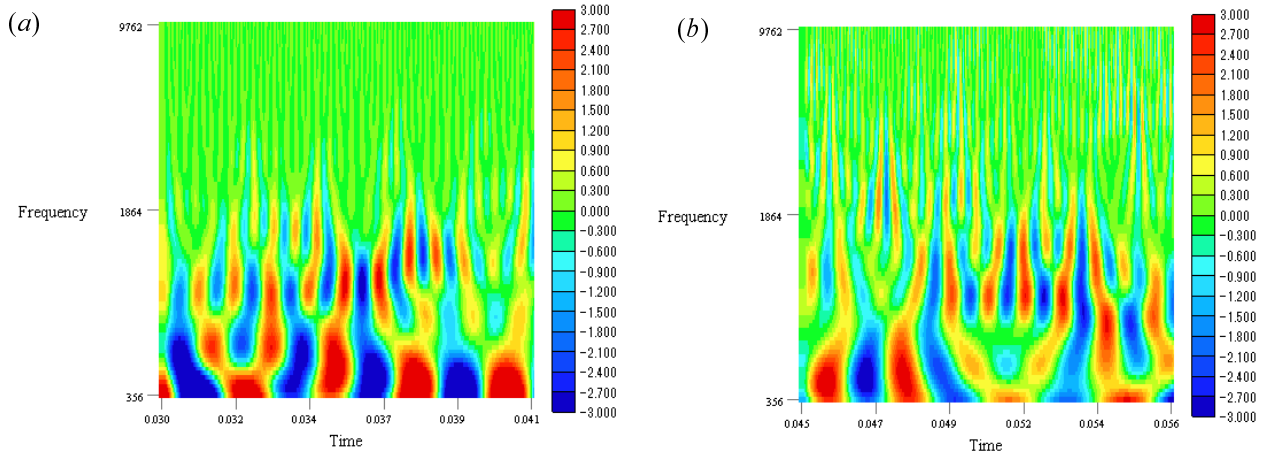

Figure 4.11: Same as figure 4.10 but for case 7.

where a and b are the dilation and location parameters, respectively. The superscript $*$ indicates the complex conjugate and $\psi(t)$ is a wavelet function. In this study, Morlet wavelet,

$$\psi(t) = \frac{1}{(2\pi)^{\frac{1}{4}}} \exp\left(-\frac{t^2}{2}\right) \exp(\imath k_\psi t), \tag{4.3}$$

is used. In an exact sense, Morlet wavelet does not satisfy the admissibility condition. However, by taking an adaptive value of k_ψ, the admissibility condition is approximately satisfied, and $k_\psi = 5.3$ was chosen in this study. In Morlet wavelet analysis, frequency can be converted by $f = k_\psi f_s / (2\pi a)$, where f_s is a sampling frequency. In the wavelet analysis with complex wavelet such as Morlet, (4.2) can be written as $T(a,b) = T^{Re}(a,b) + \imath T^{Im}(a,b)$, so that thick colors in figures 4.10 and 4.11 express the relative strong energy.

Figures 4.10 and 4.11 show the real part of continuous wavelet transform for cases 1 and 7, respectively. In fully developed grid turbulence, energy exhibits mainly in low frequency region and positive and negative values with almost the same magnitude appear periodically in time. On the other hand, there are remarkable changes in the distribution after the interaction and the energy exhibits both low and high frequency regions. This fact means that small scale eddies are

generated just behind the shock wave, which is also observed in the DNS study (Larsson *et al.*, 2013).

4.3.4 Spectral analysis

The discrete wavelet transform is used to calculate the power spectrum for the short time series data instead of the fast Fourier transform (FFT) since Fourier transform requires the long time series data. In the orthogonal discrete wavelet transform, $a = 2^m$ and $b = n \times 2^m$ in (4.2). Wavelet power spectrum is given by (Shin & Nakano, 2005)

$$E_{w,11}\left(f_m\right) = \frac{1}{2^l}\frac{2^m \Delta t}{\ln 2}\sum_{n=0}^{2^{l-m}-1}\left(T_{m,n}\right)^2 \Delta t, \tag{4.4}$$

where 2^l is the data number, Δt is the sampling time, and m and n correspond to the scale and translation, respectively. $T_{m,n}$ is the wavelet coefficient related to the discrete wavelet and expressed as $T_{m,n} = \int_{-\infty}^{\infty} dt\ u\left(t\right)\psi_{m,n}\left(t\right)$, where the wavelet function $\psi_{m,n}\left(t\right) = 2^{-m/2}\pi\left(2^{-m}t - n\right)$ satisfies the compact support.

One-dimensional power spectrum with the use of Taylor's frozen hypothesis is given by

$$E_{w,11}\left(k_{1,m}\right) = \frac{U\Delta t}{2\pi 2^{l-m}\ln 2}\sum_{n=0}^{2^{l-m}-1}\left(T_{m,n}\right)^2, \tag{4.5}$$

where $k_{1,m}$ is the m-th streamwise direction wavenumber. In this study, the Daubechies family with an index of 6 was used.

Figure 4.12 shows the one-dimensional power spectra. Good agreements are obtained between the wavelet power spectrum before the interaction and that calculated from the FFT of previous measurements in grid turbulence. As shown in figure 4.12, the energy at high wavenumbers increases after the interaction. Thus, the change in the r.m.s value of streamwise velocity fluctuation shown in figure 4.8 is due to the increase in energy at high wavenumbers.

4.3.5 The effects of initial turbulent Mach number

When we focus on the initially homogeneous isotropic turbulence, the velocity variance $\langle \boldsymbol{u}^2 \rangle$ is given by $\langle \boldsymbol{u}^2 \rangle = \left\langle \left(\boldsymbol{u}^s\right)^2 \right\rangle + \left\langle \left(\boldsymbol{u}^d\right)^2 \right\rangle$, where $\boldsymbol{u}^s$ and $\boldsymbol{u}^d$ are the

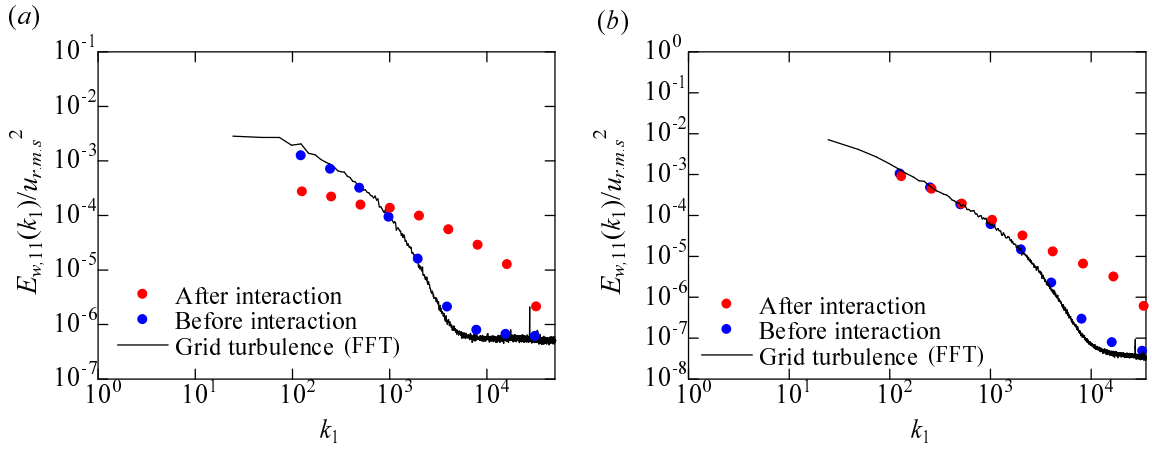

Figure 4.12: Discrete wavelet power spectra for case 1 (left) and case 7 (right).

solenoidal (divergence-free) and dilatational (curl-free) velocity components, respectively. Note that the present study focuses low-Mach-number turbulence, meaning turbulence before the interaction has no $\boldsymbol{u}^d$ component unlike previous studies, in which high-Mach-number turbulence has been mainly discussed (Agui *et al.*, 2005; Briassulis *et al.*, 1996; Honkan & Andreopoulos, 1992). Putting $\left\langle \left(\boldsymbol{u}^d\right)^2 \right\rangle = 0 \left(\left\langle (\boldsymbol{u}^s)^2 \right\rangle = 0 \right)$, the initial velocity field consists only of the solenoidal (dilatational) velocity component. Turbulecne consisting of solenoidal velocity component is similar to the Kolmogorov turbulence while turbulence consisting of dilatational velocity component is similar to the Burgulence. We will discuss the effects of initial turbulent Mach number on the changes in turbulence after the interaction. Here we consider the vorticity equation

$$\frac{\partial \omega_i}{\partial t} = \frac{\partial \omega_j u_i}{\partial x_j} - \frac{\partial \omega_i u_j^s}{\partial x_j} - u_j^d \frac{\partial \omega_i}{\partial x_j} - \omega_i \mathrm{div} \boldsymbol{u}^d - \left(\nabla \frac{1}{\rho} \times \nabla p \right)_i + \epsilon_{ijk} \nabla_j \left(\frac{1}{\rho} \frac{\partial \sigma_{kl}}{\partial x_l} \right). \quad (4.6)$$

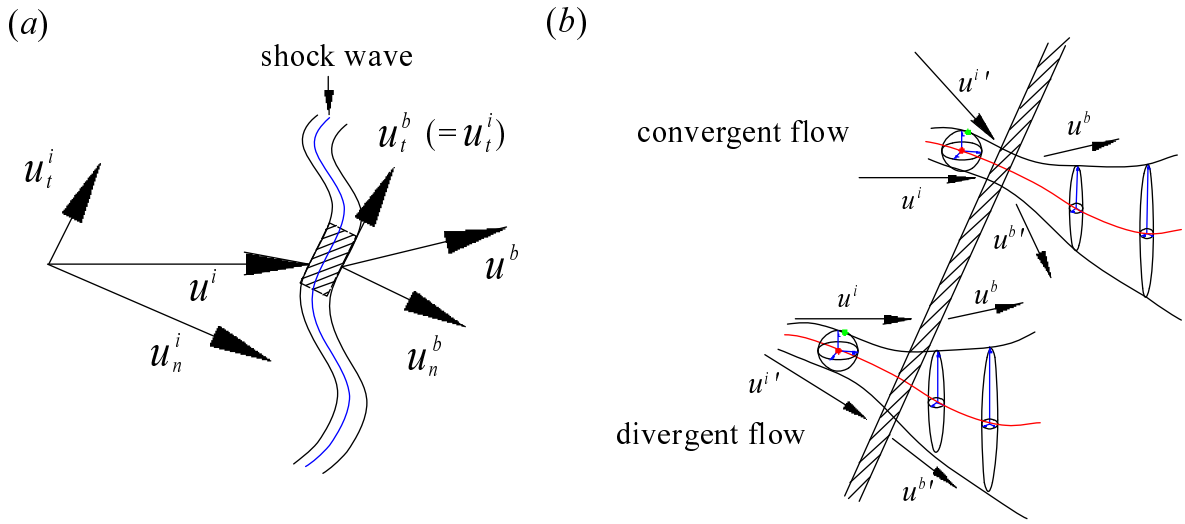

Figure 4.13: (a) Schematic of a shock wave and change in velocity vector at the reference frame, where $\boldsymbol{u}^i$ and $\boldsymbol{u}^b$ are the velocity vector in front (upstream) of a shock wave and that behind (downstream of) a shock wave, respectively. Here the subscripts t and n indicate the tangential and normal components against the shock wave front with the infinitesimal control volume, which is the shaded region, respectively. The blue curve represents a shock wave and black curves represent infinitesimal control volume surrounding a shock wave. (b) The magnified view of the shaded region in (a) and the axisymmetric convergent (or divergent) flow in front of a shock wave. Here, the velocity relation across the shock wave is given by Rankine-Hugoniot relation for an oblique shock wave. The points colored by red and green are the particles with the infinitesimal separation. $\boldsymbol{u}$ and $\boldsymbol{u}'$ are arbitrary random velocity components.

By integrating the above equation within the control volume surrounding a shock wave front shown in the shaded region in figure 4.13 (a), we obtain

$$\frac{d}{dt}\int_V \omega_i dV \approx \left[\oint_{S_{out}} \omega_n u_i dS - \oint_{S_{in}} \omega_n u_i dS\right] - \left[\oint_{S_{out}} \omega_i u_n^s dS - \oint_{S_{in}} \omega_i u_n^s dS\right] - \int_V u_j^d \frac{\partial \omega_i}{\partial x_j} dV - \int_V \omega_i \mathrm{div}\boldsymbol{u}^d dV - \int_V \left(\nabla\frac{1}{\rho}\times\nabla p\right)_i dV. \tag{4.7}$$

Note that we neglected the last term in (4.6) because it only plays a minor role. We also neglect the contribution from the infinitesimal sides notmal to the shock wave front because the shock thickness is negligibly small. The subscript n indicates the normal component, S_{in} and S_{out} are the surfaces of the inflow and outflow normal to the shock wave front. Thus, $\int_{S_{out}} \boldsymbol{\phi} dS$ $\left(\int_{S_{in}} \boldsymbol{\phi} dS\right)$ represents the outflow (inflow) amount of the physical quantity $\boldsymbol{\phi}$ after (before) the interaction. We now expand ω_i within the control volume in terms of the shock thickness δ_s as $\omega_i = \omega_i^{(0)} + \delta_s\omega_i^{(1)} + O\left(\delta_s^2\right)$, where $\omega_i^{(0)}$ is the inflow vorticity. Let $u_i^{s(0)}$ and $u_i^{d(0)}$ be the inflow solenoidal and dilatational velocity. Substitution of the perturbation series into the above equation and permutation of the above equation lead to

$$\begin{aligned}
&\int_{S_{out}} \left(\omega_n u_i - \omega_i u_n^s\right) dS \\
&\approx \oint_{S_{in}} \left(\omega_n^{(0)}\left(u_i^{s(0)} + u_i^{d(0)}\right) - \omega_i^{(0)} u_n^{s(0)}\right) dS + \int_V u_j^d \frac{\partial \omega_i^{(0)}}{\partial x_j} dV \\
&+ \int_V \omega_i^{(0)} \mathrm{div}\boldsymbol{u}^d dV + \int_V \left(\nabla\frac{1}{\rho}\times\nabla p\right) + \frac{d}{dt}\int_V \omega_i^{(0)} dV \\
&\quad + \delta_s\left[\int_V u_j^d \frac{\partial \omega_i^{(1)}}{\partial x_j} dV + \int_V \omega_i^{(1)} \mathrm{div}\boldsymbol{u}^d dV + \frac{d}{dt}\int_V \omega_i^{(1)} dV\right] + O\left(\delta_s^2\right).
\end{aligned} \tag{4.8}$$

The 3rd term represents the shock-induced compression as explained by rapid distortion theory (Jacquin *et al.*, 1993) and is equivalent to the jump condition or the Rankine–Hugoniot relation since $\mathrm{div}\boldsymbol{u}^d \approx \partial u_n^d/\partial x_n$ using $\partial u_i^d/\partial x_j \approx \delta_{in}\delta_{jn}\partial u_n^d/\partial x_n$. The 4th term is known as the baloclinic term. Grube *et al.* (2011) showed by DNS that the baroclinic term is smaller than the shock-induced compression term. The 5th and 6th terms can also be neglected since shock wave

thickness is negligibly small. Therefore, $(\omega_n u_i - \omega_i u_n^s)$ after the interaction is mainly determined by the 1st, 2nd and 3rd terms in the present study. Furthermore, taking account of the large value of div$\boldsymbol{u}^d$, it is expected that the contribution of the 3rd term is the largest. It is clear from (4.8) that the initial vorticity field $\omega_i^{(0)}$, which appears in the 1st, 2nd and 3rd terms, strongly influences on the turbulence characteristics after the interaction. If the initial velocity field is completely curl-free turbulence, i.e. $\left\langle \left(\boldsymbol{u}^{s(0)}\right)^2 \right\rangle = 0$, there is no contribution from $\omega_i^{(0)}$-related terms. In other words, $(\omega_n u_i - \omega_i u_n^s)$ after the interaction for completely divergence-free turbulence, i.e. $\left\langle \left(\boldsymbol{u}^{d(0)}\right)^2 \right\rangle = 0$, is larger than that for completely curl-free turbulence, since the contribution from the shock-induced compression increases with $\left\langle \left(\boldsymbol{u}^{s(0)}\right)^2 \right\rangle$. The increase in vorticity causes the increase in energy at high wavenumber as shown in figure 4.12. In fact, the increase in energy at high wavenumber obtained in the present study is larger than that in previous studies on high-Mach-number turbulence (Agui *et al.*, 2005; Honkan & Andreopoulos, 1992).

Next, we discuss the physical mechanism for the changes in turbulence after the interaction from a different perspective. Let us consider the motions of the two particles with the infinitesimal separation in front of a shock wave. Figure 4.13 (*b*) shows schematic for an axisymmetric convergent and divergent flow in front of a shock wave. After the particles passed a shock wave, the distance between the particles gradually increases because of the Rankine-Hugoniot relation. In such a situation, the Lyapunov exponent is positive, i.e. the structure expressed by the Lyapunov vectors deforms from a spherical shape to an ellipsoidal shape, and therefore, the velocity fluctuation increases. Furthermore, the length scales perpendicular to the shock wavefront decrease, whereas the length scales parallel to the shock wavefront increase as shown in figure 4.13 (*b*). This explanation is consistent with the alignment of eddies behind a planar shock wave(Larsson *et al.*, 2013).

Finally, we comment on the difference between the normal shock wave and the blast-like shock wave against the changes in turbulence. The main characteristic of a blast-like shock wave is that the shock wave is continuously followed by the expansion fan, i.e. it has two different density gradients: drastic compression due to the shock wave and expansion due to an expansion fan as shown in figures

4.2–4.4. Taking into account of the facts that turbulence has a pressure gradient, typically seen as a vortex tube, and a mean density gradient due to the expansion fan, the vorticity fluctuations are generated via the baroclinic effect. Thus, the turbulent field after the interaction with a blast-like shock wave is more complex and has messy field compared with that interacting with a normal shock wave.

4.4 Conclusions

Characteristics of divergence-free grid turbulence interacting with a weak shock wave ($M_s = 1.05$) are experimentally investigated. The main results are as follows.

1. The r.m.s value of the streamwise velocity fluctuation, $u_{r.m.s}$, increases after the interaction. The changes in $u_{r.m.s}$ become small with the increase of Re_λ for the same strength of the shock wave.

2. The streamwise integral length scale, L, decreases after the interaction. The changes in L become small with the increase of Re_λ for the same strength of the shock wave.

3. The continuous wavelet analysis shows that energy exhibits mainly in low frequency region and positive and negative values appear periodically in time before the interaction, whereas it exhibits both low and high frequency regions after the interaction. Furthermore, small scale eddies are generated just behind a shock wave. The spectral analysis also shows that the energy at high wavenumbers increases after the interaction. Thus, the increase in velocity fluctuation is caused by the increase in energy at high wavenumbers.

4. The increase in energy at high wavenumbers is interpreted from the viewpoint of initial turbulent Mach number and the increase for initially divergence-free turbulence is larger than that for initially high-Mach number (highly curl-free) turbulence.

Chapter 5

Rapid distortion analysis theory analysis on the interaction between homogeneous turbulence and a planar shock wave

5.1 Introduction

As described in chapter 4, the interaction between turbulence and a shock wave is very important in engineering and space physics. This interaction is observed in supersonic transport (SST) in the generation of sonic booms and in the flow of a combustor in engineering. Turbulence–shock interactions are observed in space physics, such as in star formation, with supernovas, and in the interaction between solar wind and bow shock around the earth.

With fluids in space, the characteristics of Burgulence, in which the velocity spectrum exhibits $E(k) \sim k^{-2}$, have been observed in the Ursa Major interstellar cloud (Miville-Deschenes *et al.*, 2003), where k is the wavenumber. On the other hand, the characteristics of Kolmogorov turbulence, the spectrum of electron density fluctuations which satisfies $k^2 N_k^{(e)}(k) \sim k^{-\frac{5}{3}}$ has been observed in the local interstellar medium (Armstrong *et al.*, 1995). Here, $N_k^{(e)}(k)$ is an electron density power spectrum. The former is considered as a characteristic that the dilatational mode dominates the velocity field, whereas the latter corresponds to

the case in which the solenoidal mode dominates the velocity field. The changes in turbulence interacting with a shock wave is assumed to depend on which mode dominated before the interaction.

Fundamental understanding of such physics is essential for the development of next generation SSTs, improvement of combustion processes and high-speed rotor flows, and further understanding of space physics. However, it is difficult to clarify the relationships between turbulence and a shock wave because it involves complex linear and nonlinear mechanisms, which can considerably change turbulence structure and its statistical properties, and the dynamics of the shock wave motion (Andreopoulos *et al.*, 2000). As shown in chapter 4, amplification of velocity fluctuations and substantial changes in turbulence characteristic length scales are the most recognized outcomes from the studies on turbulence interacting with a shock wave. However, there have been qualitative and quantitative disagreements between experimental results and direct numerical simulation (DNS) results in previous studies. Also the lack of a theory on the interaction between turbulence and shock waves has been identified.

Andreopoulos *et al.* (2000) documented the following unanswered questions regarding the interaction between turbulence and shock waves from the perspective of turbulence research.

1. How much of the amplification of turbulence interacted with a shock wave is caused entirely by the Rankine–Hugoniot conditions?
2. Why are vorticity fluctuations amplified more than velocity fluctuations?
3. Why is the energy of small eddies amplified more than that of large eddies?
4. Are the length scales of the incoming turbulence reduced or amplified through these interactions?
5. Is the TKE dissipation rate reduced?

This chapter attempts to provide analytical answers to the above five questions using rapid distortion theory (RDT) analysis.

More specifically, I investigate the changes in TKE, enstrophy, and turbulence characteristic lengths, and show that the amplifications of TKE and enstrophy

depend on the initial degree of anisotropy. Furthermore, we attempt to answer the unsolved questions in the report by Andreopoulos *et al.* (2000) within the linear theoretical framework.

5.2 Rapid Distortion Theory

5.2.1 Basic equations

The starting point of this study is the continuity equation (2.1) and momentum equation in a compressible fluid without any gravity effects.

$$\rho\frac{\partial}{\partial t}v_i + \rho v_j\frac{\partial}{\partial x_j}v_i = -\frac{\partial p}{\partial x_i} + \frac{\partial}{\partial x_i}\mu'\mathrm{div}\boldsymbol{v} + \frac{\partial}{\partial x_j}\mu\left(\frac{\partial v_i}{\partial x_j} + \frac{\partial v_j}{\partial x_i}\right), \tag{5.1}$$

where μ' is the second coefficient of viscosity (under the Stokes assumption, $\mu' = -\frac{2}{3}\mu$), respectively. We now divide the density, velocity, and pressure fields into mean and fluctuating components, i.e. $v_i = U_i + u_i$, $\rho = \overline{\rho} + \rho'$, and $p = \overline{p} + p'$, where U_i, $\overline{\rho}$, and $\overline{p}$ are the mean components and u_i, ρ', and p' are the fluctuating components. In the Reynolds averaged equation, we assume $\rho' \ll \overline{\rho}$ and neglect ρ' when $\overline{\rho}$ exists, and the density is linearized. This preserves the triad resonant condition in Fourier space as seen in the incompressible turbulence (Marion *et al.*, 1988).

5.2.1.1 Mean flow

In a compressible flow, the homogeneity requires that the mean flow gradients and mean pressure be spatially uniform; in an incompressible flow, mean pressure need not be uniform (Durbin & Zeman, 1992). In the former case, the requirement of a uniform mean velocity gradient indicates that $\boldsymbol{U}$ is expressed as $\boldsymbol{U} = \boldsymbol{x}\cdot\boldsymbol{S}(t)$, and that of a uniform pressure shows that the velocity satisfies $D\boldsymbol{U}/Dt = 0$ by substituting the Euler equation, because in turbulence–shock wave interactions, the mean field satisfies the Rankine–Hugoniot relation. From the continuity equation, the mean of a density and an adiabatic sound speed are given by

$$\overline{\rho} = \rho_0\mathrm{Det}(\boldsymbol{J}),\ \overline{c^2} = c_0^2\left[\mathrm{Det}(\boldsymbol{J})\right]^{\kappa-1}, \tag{5.2}$$

where the subscript 0 indicates the initial state and κ is the ratio of specific heats. The matrix $\boldsymbol{J}$ is given by

$$\boldsymbol{J} = \begin{bmatrix} \frac{1}{1+S_1 t} & 0 & 0 \\ 0 & \frac{1}{1+S_2 t} & 0 \\ 0 & 0 & \frac{1}{1+S_3 t} \end{bmatrix}, \tag{5.3}$$

where S_i is an arbitrary constant. In phenomena such as turbulence–shock wave interactions, turbulence is assumed to be strongly compressed in a one-dimensional direction, as confirmed by experiments (e.g. Honkan & Andreopoulos 1992; Agui *et al.* 2005) and DNSs (e.g. Lee *et al.* 1993; Larsson & Lele 2009). For one-dimensional compression, S_1 is negative and $S_2 = S_3 = 0$. Here, the magnitude of S_1 is the strength of compression. In RDT analysis, the shock-induced compression is approximated as a homogeneous compression. The mean density, determined by continuity, the mean pressure, determined by the isentropic formula, and the adiabatic sound speed are given, respectively, by

$$\overline{\rho}\,(t) = \rho_0 \frac{1}{1+S_1 t},\ \overline{p}\,(t) = p_0 \frac{1}{(1+S_1 t)^{\kappa}},\ \overline{c^2}\,(t) = c_0^2 \frac{1}{(1+S_1 t)^{\kappa-1}}. \tag{5.4}$$

Using the ideal gas law, the kinematic viscosity $\nu\,(t)$ is given by

$$\nu\,(t) = \frac{\overline{\mu}}{\overline{\rho}} = \frac{\mu_0}{\overline{\rho}} \left(\frac{\overline{T}}{T_0} \right)^n = \frac{\nu_0}{(1+S_1 t)^{n(\kappa-1)-1}}, \tag{5.5}$$

where the viscosity is given by the power law of temperature T, and the exponent n is taken to be $3/4$, as in Larsson & Lele (2009); Grube *et al.* 2011. Here κ is taken to be $\kappa = 7/5$.

5.2.1.2 Fluctuations

Owing to the assumption that the mean density is spatially uniform, and given that $D\boldsymbol{U}/Dt = 0$ and $D\overline{\rho}/Dt = -\overline{\rho}\nabla \cdot \boldsymbol{U}$, linearized continuity and momentum equations are given by

$$\frac{D}{Dt}\left(\frac{p'}{\kappa \overline{p}\,(t)} \right) = -\mathrm{div}\boldsymbol{u}, \tag{5.6}$$

$$\frac{\partial}{\partial t}u_i + U_j \frac{\partial u_i}{\partial x_j} + u_j \frac{\partial U_i}{\partial x_j} = -\overline{c^2}\,(t) \frac{\partial}{\partial x_i}\left(\frac{p'}{\kappa \overline{p}\,(t)} \right) + \nu \frac{\partial^2 u_i}{\partial x_j \partial x_j} + \frac{\nu}{3}\frac{\partial}{\partial x_i}\mathrm{div}\boldsymbol{u}. \tag{5.7}$$

Here, the conservation of entropy is used. Note that the assumption $\rho' \ll \overline{\rho}$ requires a turbulent Mach number $M_t \ll 1$; this requirement is satisfied when the initial velocity fields consist only of solenoidal modes. Using the Helmholtz decomposition, the velocity fields can be split into irrotational and rotational components:

$$\boldsymbol{u} = \nabla\phi + \nabla \times \boldsymbol{a} = \boldsymbol{u}^d + \boldsymbol{u}^s, \tag{5.8}$$

where ϕ is the scalar potential and $\boldsymbol{a}$ is the vector potential. Note that the dilatational component $\boldsymbol{u}^d$ is irrotational, i.e. $\nabla \times \boldsymbol{u}^d = 0$, and that the solenoidal component $\boldsymbol{u}^s$ satisfies $\nabla \cdot \boldsymbol{u}^s = 0$. Turbulence fluctuations are represented as the superposition of plane waves using Fourier transforms:

$$u_i(\boldsymbol{x}, t) = \int d\boldsymbol{\chi}\ \hat{u}_i(\boldsymbol{\chi}, t) \exp(\imath \boldsymbol{\chi} \cdot \boldsymbol{x}), \tag{5.9}$$

$$p(\boldsymbol{x}, t) = \int d\boldsymbol{\chi}\ \hat{p}(\boldsymbol{\chi}, t) \exp(\imath \boldsymbol{\chi} \cdot \boldsymbol{x}), \tag{5.10}$$

where $\boldsymbol{\chi}$ is the wavenumber vector. Because the system under consideration is treated as homogeneous turbulence, the wavenumber vectors vary in time as follows:

$$\frac{d\chi_i}{dt} = -\frac{\partial U_j}{\partial x_i}\chi_j = -S_{ji}\chi_j. \tag{5.11}$$

Taking the Fourier transform of (5.6) and (5.7) and using (5.11), we obtain

$$\frac{d}{dt}\frac{\hat{p}(\boldsymbol{\chi}, t)}{\kappa\overline{p}(t)} = -\imath\chi\hat{u}^d(\boldsymbol{\chi}, t), \tag{5.12}$$

$$\left(\frac{d}{dt} + \nu\chi^2\right)\hat{u}_j(\boldsymbol{\chi}, t) = -S_{jn}(t)\,\hat{u}_n(\boldsymbol{\chi}, t) - \imath\overline{c^2}(t)\,\chi_j\frac{\hat{p}(\boldsymbol{\chi}, t)}{\kappa\overline{p}(t)} - \frac{\nu}{3}\chi_j\chi_n\hat{u}_n(\boldsymbol{\chi}, t). \tag{5.13}$$

It is convenient to introduce two projectors, $\Pi_{ij}(\boldsymbol{\chi})$ and $P_{ij}(\boldsymbol{\chi}, t)$, which are expressions in Fourier space of the velocity field against (5.8):

$$\Pi_{ij}(\boldsymbol{\chi}) = \frac{\chi_i\chi_j}{\chi^2},\ P_{ij}(\boldsymbol{\chi}) = \delta_{ij} - \frac{\chi_i\chi_j}{\chi^2}, \tag{5.14}$$

where δ_{ij} is the Kronecker delta. Using these projectors, the velocity field can be split into dilatational and solenoidal parts:

$$\hat{u}_i(\boldsymbol{\chi}, t) = \hat{u}_i^d(\boldsymbol{\chi}, t) + \hat{u}_i^s(\boldsymbol{\chi}, t) = \Pi_{ij}(\boldsymbol{\chi})\,\hat{u}_j(\boldsymbol{\chi}, t) + P_{ij}(\boldsymbol{\chi}, t)\,\hat{u}_j(\boldsymbol{\chi}, t), \tag{5.15}$$

and using (5.15), it is obvious that the solenoidal mode satisfies

$$\boldsymbol{\chi} \cdot \boldsymbol{u}^s (\boldsymbol{\chi}, t) = 0. \tag{5.16}$$

We then consider the evolution of the dilatational and the solenoidal modes. Multiplying χ_i by (5.13) and dividing by χ, we obtain

$$\left(\frac{d}{dt} + \frac{4}{3}\nu(t)\chi^2\right)\hat{u}^d(\boldsymbol{\chi}, t) = -S_{ij}(t)\,\Pi_{ij}(\boldsymbol{\chi})\,\hat{u}^d(\boldsymbol{\chi}, t) - 2S_{ij}\frac{\chi_i}{\chi}P_{jn}(\boldsymbol{\chi}, t)\,\hat{u}_n^s(\boldsymbol{\chi}, t) - \imath\chi c^2(t)\frac{\hat{p}(\boldsymbol{\chi}, t)}{\kappa\overline{p}(t)}, \tag{5.17}$$

where $\hat{u}^d(\boldsymbol{\chi}, t) = \chi_j/\chi \hat{u}_j^d(\boldsymbol{\chi}, t)$. Multiplying $\chi^2 P_{ij}(\boldsymbol{\chi})$ by (5.13) and dividing by χ^2, we obtain

$$\left(\frac{d}{dt} + \nu(t)\chi^2\right)\hat{u}_i^s(\boldsymbol{\chi}, t) = \frac{\chi_l}{\chi}P_{ij}(\boldsymbol{\chi})\left[S_{lj}(t) - S_{jl}(t)\right]\hat{u}^d(\boldsymbol{\chi}, t) + \left(\frac{\chi_i\chi_l S_{lj}(t)\,\delta_{jn}}{\chi^2} - P_{ij}(\boldsymbol{\chi})\,S_{jn}(t)\right)\hat{u}_n^s(\boldsymbol{\chi}, t). \tag{5.18}$$

Note that there is a slight difference in the viscous terms in (5.17) and (5.18). Equations (5.17) and (5.18) are the same as the basis equations of Marion *et al.* (1988) for $S_1 = 0$. The solution to (5.11) can be easily obtained by means of separation of variables. The wavenumber vector $\boldsymbol{\chi}(t)$ is given by

$$\boldsymbol{\chi} = \left[\chi_1(t),\ \chi_2(t),\ \chi_3(t)\right] = \left[\frac{k_1}{1 + S_1 t},\ k_2,\ k_3\right], \tag{5.19}$$

where $\boldsymbol{k} = [k_1,\ k_2,\ k_3]$ is an initial wavenumber vector and $\chi^2 = \frac{1}{(1+S_1t)^2}\left[k_1^2 + k_{23}^2(1 + S_1 t)^2\right]$, where $k_{23}^2 = k_2^2 + k_3^2$.

5.2.2 RDT assumptions for the turbulence-shock wave interaction

RDT is a method for solving linearized governing equations under rapid deformation using a statistical technique; RDT solutions are exact solutions of the Navier–Stokes equations if the initial flow is a single plane wave because the nonlinear terms are exactly zero throughout the triad interaction (Craik & Criminale

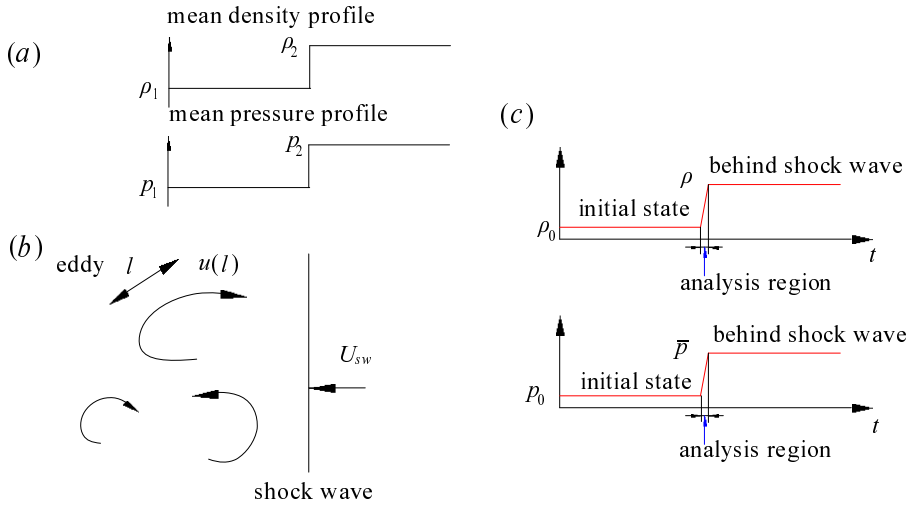

Figure 5.1: (a) Mean density and pressure profiles via the Rankine–Hugoniot relation, where the subscript 1 denotes the front of the planar shock wave and the subscript 2 denotes the back of the planar shock wave. (b) Schematic of interaction between turbulence and a shock wave. (c) Schematic of the RDT analysis region.

1986; Kevlahan & Hunt 1997). RDT equations are obtained by neglecting the nonlinear terms in (5.17) and (5.18) which linearize the equations; this allows analytical solutions for a number of cases. For the details of RDT, refer to Hunt & Carruthers (1990), Hunt & Kevlahan (1993), and Kevlahan & Hunt (1997).

Figure 5.1 shows a schematic of the turbulence–shock wave interaction. The time scale of the turbulence–shock wave interaction, T_{SW}, is found to be small, relative to the turbulence characteristic time scale $\tau(l) \sim l/u(l)$, where l is the turbulence characteristic length scale and $u(l)$ is a turbulence characteristic velocity. In addition, if the linear effects of the compression (e.g. $\sim \mid S_1 \mid (u(l)/l)$ for a compressing distortion) on vorticity $\boldsymbol{\omega}$ are much stronger than the nonlinear self-induced compression by the turbulence ($\sim (u(l)/l)^2$), the nonlinear terms do not play an important role. When turbulence is compressed by a planar shock wave, the strength of the characteristic compression can be given by

$$\mid S_1 \mid = \frac{U_{SW} - u_0}{\delta_{SW}}, \tag{5.20}$$

where δ_{SW} is the thickness of the region influenced by the shock–induced compression, U_{SW} is the speed of a shock wave and u_0 is the mean velocity in front of a shock. Thus, the following relations are assumed for the interaction between turbulence and the shock wave:

$$T_{SW} \ll \tau\left(l\right) \sim \frac{l}{u\left(l\right)} \text{ or } \mid S_1 \mid \gg \frac{u\left(l\right)}{l}. \tag{5.21}$$

The first relation in (5.21) is valid for small values of T_{SW}, whereas the second relation in (5.21) is valid for large values of $\mid S_1 \mid$. An overall criterion for the validity of RDT for calculating the statistics of the energy-containing eddies in a given turbulent flow can be derived from (5.21) in terms of the r.m.s. velocity $u_{r.m.s}$ and the integral length scale L (Kevlahan & Hunt, 1997). This leads to

$$T_{SW} \ll T_L \sim \frac{L}{u_{r.m.s}} \text{ or } \frac{u_{r.m.s}}{L}\frac{1}{\mid S_1 \mid} \equiv \delta \ll 1, \tag{5.22}$$

where T_L is the integral time scale. This can be re-expressed as

$$\frac{1}{T_L} \ll \max\left(\mid S_1 \mid, \frac{1}{T_{SW}}\right). \tag{5.23}$$

This criterion should be valid at the start of the distortion. Kevlahan (1997) showed that the vorticity jump is connected with a shock curvature, baroclinic effect, and the conservation of angular momentum. In RDT analysis, vorticity amplification is interpreted as caused by the angular momentum created by compression of the flow in the direction normal to the shock wave front. Therefore, one must note that the present analysis is limited to the case in which the deformation of the shock wave can be ignored. The bases of inviscid RDT equations are (5.12),

$$\frac{d}{dt}\hat{u}^d\left(\boldsymbol{\chi},t\right) = -S_{ij}\left(t\right)\Pi_{ij}\left(\boldsymbol{\chi}\right)\hat{u}^d\left(\boldsymbol{\chi},t\right) - 2S_{ij}\frac{\chi_i}{\chi}P_{jn}\left(\boldsymbol{\chi},t\right)\hat{u}^s_n\left(\boldsymbol{\chi},t\right) - \imath\chi c^2\left(t\right)\frac{\hat{p}\left(\boldsymbol{\chi},t\right)}{\kappa\overline{p}\left(t\right)}, \tag{5.24}$$

$$\begin{aligned}\frac{d}{dt}\hat{u}^s_i\left(\boldsymbol{\chi},t\right) = {} & \frac{\chi_l}{\chi}P_{ij}\left(\boldsymbol{\chi}\right)\left[S_{lj}\left(t\right) - S_{jl}\left(t\right)\right]\hat{u}^d\left(\boldsymbol{\chi},t\right) \\ & + \left(\frac{\chi_i\chi_l S_{lj}\left(t\right)\delta_{jn}}{\chi^2} - P_{ij}\left(\boldsymbol{\chi}\right)S_{jn}\left(t\right)\right)\hat{u}^s_n\left(\boldsymbol{\chi},t\right).\end{aligned} \tag{5.25}$$

Note that the dilatational mode in (5.25) disappears because of the symmetrical form of $S_{lj}(t) = \delta_{l1} S_{11}(t) \delta_{j1}$. For one-dimensional compression, (5.25) is the same as in Mahesh *et al.* (1994) without shear. However, they did not obtain the analytical solutions and only performed a numerical analysis. The solutions to the system are expected to have the form

$$\hat{u}_i^s(\boldsymbol{\chi}, t) = G_{ij}^s(\boldsymbol{\chi}, t)\, \hat{u}_j^s(\boldsymbol{k}, 0), \tag{5.26}$$

$$\hat{u}_i^d(\boldsymbol{\chi}, t) = G_{ij}^d(\boldsymbol{\chi}, t)\, \hat{u}_j(\boldsymbol{k}, 0) + G^p(\boldsymbol{\chi}, t)\, \hat{p}(\boldsymbol{k}, 0), \tag{5.27}$$

where $\boldsymbol{G}$ are Green functions.

5.2.3 ODEs and analytical solution for inviscid RDT

We consider the analytical solution of the inviscid RDT equations. From (5.25) and the solenoidal condition (5.16), we obtain

$$\underbrace{\frac{d}{dt}\begin{bmatrix} \hat{u}_1^s(\boldsymbol{\chi}, t) \\ \hat{u}_2^s(\boldsymbol{\chi}, t) \\ \hat{u}_3^s(\boldsymbol{\chi}, t) \end{bmatrix}}_{\hat{\boldsymbol{u}}^s} = \underbrace{\frac{S_1}{k_1^2 + k_{23}^2 (1 + S_1 t)^2} \begin{bmatrix} -k_{23}^2 (1 + S_1 t) & -k_1 k_2 & -k_1 k_3 \\ k_1 k_2 & -k_2^2 (1 + S_1 t) & -k_2 k_3 (1 + S_1 t) \\ k_1 k_3 & -k_2 k_3 (1 + S_1 t) & -k_3^2 (1 + S_1 t) \end{bmatrix}}_{\boldsymbol{A}} \underbrace{\begin{bmatrix} \hat{u}_1^s(\boldsymbol{\chi}, t) \\ \hat{u}_2^s(\boldsymbol{\chi}, t) \\ \hat{u}_3^s(\boldsymbol{\chi}, t) \end{bmatrix}}_{\hat{\boldsymbol{u}}^s}, \tag{5.28}$$

Here, the method for solving the ODEs is described briefly, because cumbersome calculations are required to solve them analytically (see Appendix A for details). The ODE will be set to $\frac{d\hat{u}_i^s(\boldsymbol{\chi}, t)}{dt} = A_{ij}(t)\, \hat{u}_j^s(\boldsymbol{\chi}, t)$ if the tensor notation of (5.28) is utilized. We then determine the eigenvalues of $A_{ij}(t)$. After some algebra, the eigenvalues of $A_{ij}(t)$ are as follows:

$$\lambda = 0, -\frac{S_1 k_{23}^2 (1 + S_1 t) + \imath S_1 k_1 k_{23}}{k_1^2 + k_{23}^2 (1 + S_1 t)^2}, -\frac{S_1 k_{23}^2 (1 + S_1 t) - \imath S_1 k_1 k_{23}}{k_1^2 + k_{23}^2 (1 + S_1 t)^2}. \tag{5.29}$$

Each eigenvector can be obtained for the acquired eigenvalues. Let B_{ij} be the transformation matrix which consists of eigenvectors. A diagonal matrix $D_{\alpha\beta}(t)$

can be expressed as $D_{\alpha\beta}(t) = B_{\alpha i}^{-1} A_{ij}(t) B_{j\beta}$. Multiplying B_{ij}^{-1} to (5.28) from the left side, we obtain $\frac{dy_i(\boldsymbol{\chi},t)}{dt} = D_{ij}(t) y_j(\boldsymbol{\chi},t)$, where $y_i(\boldsymbol{\chi},t) = B_{ij}^{-1}\hat{u}_i^s(\boldsymbol{\chi},t)$. Because $D_{ij}(t)$ is a symmetrical tensor, which has only diagonal components, the solution to $y_i(\boldsymbol{\chi},t)$ is obtained using separation of variables. If the relationship of $\hat{u}_i^s(\boldsymbol{\chi},t) = B_{ij} y_j(\boldsymbol{\chi},t)$ and the initial conditions of $y_i(\boldsymbol{k},0) = B_{ij}\hat{u}_j^s(\boldsymbol{k},0)$ are used, analytical solutions are given by

$$\begin{aligned}\hat{u}_1^s(\boldsymbol{\chi},t) &= P\hat{u}_1^s(\boldsymbol{k},0) - \frac{k_2 Q}{k_{23}}\hat{u}_2^s(\boldsymbol{k},0) - \frac{k_3 Q}{k_{23}}\hat{u}_3^s(\boldsymbol{k},0) \\ &= \frac{k^2(1+S_1 t)}{k_1^2 + k_{23}^2(1+S_1 t)^2}\hat{u}_1^s(\boldsymbol{k},0),\end{aligned} \tag{5.30}$$

$$\begin{aligned}\hat{u}_2^s(\boldsymbol{\chi},t) &= \frac{k_2 Q}{k_{23}}\hat{u}_1^s(\boldsymbol{k},0) + \frac{k_3^2 + k_2^2 P}{k_{23}^2}\hat{u}_2^s(\boldsymbol{k},0) + \frac{k_2 k_3}{k_{23}^2}(P-1)\hat{u}_3^s(\boldsymbol{k},0) \\ &= \frac{k_1 k_2 S_1 t(2+S_1 t)}{k_1^2 + k_{23}^2(1+S_1 t)^2}\hat{u}_1^s(\boldsymbol{k},0) + \hat{u}_2^s(\boldsymbol{k},0),\end{aligned} \tag{5.31}$$

$$\begin{aligned}\hat{u}_3^s(\boldsymbol{\chi},t) &= \frac{k_3 Q}{k_{23}}\hat{u}_1^s(\boldsymbol{k},0) + \frac{k_2 k_3}{k_{23}^2}(P-1)\hat{u}_2^s(\boldsymbol{k},0) + \frac{k_2^2 + k_3^2 P}{k_{23}^2}\hat{u}_3^s(\boldsymbol{k},0) \\ &= \frac{k_1 k_3 S_1 t(2+S_1 t)}{k_1^2 + k_{23}^2(1+S_1 t)^2}\hat{u}_1^s(\boldsymbol{k},0) + \hat{u}_3^s(\boldsymbol{k},0),\end{aligned} \tag{5.32}$$

where

$$P = \frac{k_1^2 + k_{23}^2(1+S_1 t)}{k_1^2 + k_{23}^2(1+S_1 t)^2}, \tag{5.33}$$

$$Q = \frac{k_1 k_{23} S_1 t}{k_1^2 + k_{23}^2(1+S_1 t)^2}. \tag{5.34}$$

For convenience in later discussions, the analytical solutions in the Craya–Herring decomposition are given by

$$\hat{u}^{(1)}(\boldsymbol{\chi},t) = \frac{\imath}{k_{23}}\hat{\omega}_1^s(\boldsymbol{\chi},t) = \left[\frac{k_3}{k_{23}}\hat{u}_2^s(\boldsymbol{k},0) - \frac{k_2}{k_{23}}\hat{u}_3^s(\boldsymbol{k},0)\right], \tag{5.35}$$

$$\hat{u}^{(2)}(\boldsymbol{\chi},t) = -\frac{\chi}{\chi_{23}}\hat{u}_1^s(\boldsymbol{\chi},t) = -\frac{k^2}{k_{23}}\frac{\hat{u}_1^s(\boldsymbol{k},0)}{\sqrt{k_1^2 + k_{23}^2(1+S_1 t)^2}}. \tag{5.36}$$

Interestingly, the vortex mode, $\hat{u}^{(1)}(\boldsymbol{\chi},t)$, is not affected by the rapid one-dimensional compression, whereas the wave mode, $\hat{u}^{(2)}(\boldsymbol{\chi},t)$, is strongly affected. Thus, vorticity in the one-dimensional compressed direction does not change throughout the

turbulence–shock wave interaction in the limiting case, as discussed later. This situation is similar to that in stratified turbulence (Hanazaki & Hunt, 1996). The fact that the vorticity does not change in the compressed direction is a direct result of the jump conditions for vorticity. Kevlahan (1997) also showed that vorticity only increases in the plane tangent to a shock wave.

After some algebra, the inviscid RDT equation for the dilatational mode becomes

$$\frac{d}{dt}\left[\frac{(1+S_1t)^{\kappa+1}}{k_1^2+k_{23}^2(1+S_1t)^2}\frac{d\hat{u}^d(\boldsymbol{\chi},t)}{dt}\right]+\frac{(1+S_1t)^{\kappa+1}}{k_1^2+k_{23}^2(1+S_1t)^2}\chi c^2(t)R(t)\hat{u}^d(t)$$
$$=-\frac{(1+S_1t)^{\kappa+1}}{k_1^2+k_{23}^2(1+S_1t)^2}\chi c^2(t)\frac{d}{dt}\left(\frac{2S_1k^2k_1(1+S_1t)^{\kappa}}{c_0^2\left[k_1^2+k_{23}^2(1+S_1t)^2\right]^2}\right)\hat{u}_1^s(\boldsymbol{k},0), \tag{5.37}$$

where $R(t)$ is given by

$$R(t)=\frac{d}{dt}\left(\frac{S_{11}(t)\Pi_{11}(\boldsymbol{\chi})}{\chi c^2(t)}\right)+\chi, \tag{5.38}$$

and the left-hand side (denoted hereafter as l.h.s.) of (5.37) is a typical Sturm–Liouville equation. Thus, the analytical solution is assumed to be a special function such as a Legendre function (e.g. Hanazaki & Hunt 2004). In general, the analytical solution will take the form $\hat{u}^d(\boldsymbol{\chi},t)=u_0(t)+C_1u_1(t)+C_1u_2(t)$, where u_0 is a particular solution, and $u_1(t)$ and $u_2(t)$ are basis solutions. If one basis solution is found, the analytical solution of the dilatational mode can be obtained. When $S_1=0$, the analytical solutions are expressed by trigonometric functions (Marion *et al.*, 1988). Unfortunately, we could not find any analytical solutions for the dilatational mode. Thus, hereinafter we only discuss the RDT solutions of the solenoidal mode. Note that Jacquin *et al.* (1993) found the analytical solution for the case in which the second term of (5.37) is neglected.

5.3 Homogeneous axisymmetric turbulence

Homogeneous axisymmetrical tensors in Cartesian coordinates have been developed by Batchelor (1946, 1953) and Chandrasekhar (1950). The general second-

order two-point correlation has the form

$$\Phi_{ij}(\boldsymbol{k}) = A_1 k_i k_j + A_2 n_i n_j + A_3 \delta_{ij} + A_4 n_i k_j + A_5 n_j k_i, \tag{5.39}$$

where $A_1 \sim A_5$ are functions (not all independent) of k^2 and $k\cos\theta = \boldsymbol{k}\cdot\boldsymbol{n}$, where $\boldsymbol{n}$ is a unit vector in the direction of the symmetry axis.

We obtain the relation $A_4 = A_5$ from the reflection invariant, $\Phi_{ij}(\boldsymbol{k}) = \Phi_{ij}(-\boldsymbol{k})$, which implies the symmetry condition $\Phi_{ij}(\boldsymbol{k}) = \Phi_{ji}(\boldsymbol{k})$. Then, we obtain the following relation from the solenoidal condition $k_i\Phi_{ij}(\boldsymbol{k}) = k_j\Phi_{ij}(\boldsymbol{k}) = 0$:

$$\Phi_{ij}(\boldsymbol{k}) = -k^2 P_{ij}(\boldsymbol{k}) A_1(k,\cos\theta) + H_{ij}(\boldsymbol{k}) A_2(k,\cos\theta) \tag{5.40}$$

$$\begin{aligned} H_{ij}(\boldsymbol{k}) &= n_i n_j + \frac{(\boldsymbol{k}\cdot\boldsymbol{n})^2}{k^2}\delta_{ij} - (\boldsymbol{k}\cdot\boldsymbol{n})\frac{n_i k_j + n_j k_i}{k^2} \\ &= \cos^2\theta e_i^{(1)}(\boldsymbol{k}) e_j^{(1)}(\boldsymbol{k}) + e_i^{(2)}(\boldsymbol{k}) e_j^{(2)}(\boldsymbol{k}), \end{aligned} \tag{5.41}$$

where $\boldsymbol{e}^{(1)}(\boldsymbol{\chi})$ and $e^{(2)}(\boldsymbol{\chi})$ are the basis unit vectors of the Craya–Herring decomposition defined as

$$\boldsymbol{e}^{(1)}(\boldsymbol{\chi}) = \frac{\boldsymbol{\chi}\times\boldsymbol{n}}{|\,\boldsymbol{\chi}\times\boldsymbol{n}\,|}, \quad \boldsymbol{e}^{(2)}(\boldsymbol{\chi}) = \frac{\boldsymbol{\chi}}{\chi}\times\boldsymbol{e}^{(1)}(\boldsymbol{\chi}). \tag{5.42}$$

For homogeneous isotropic turbulence, $A_1(k,\cos\theta) = -\frac{E(k)}{4\pi k^4}$ and $A_2(k,\cos\theta) = 0$ are satisfied. In the Craya-Herring frame, $\Phi_{ij}(\boldsymbol{\chi},t)$ is given by

$$\begin{aligned} \Phi_{ij}(\boldsymbol{k}) = e_i^{(1)}(\boldsymbol{k}) e_j^{(1)}(\boldsymbol{k}) \underbrace{\left[-k^2 A_1(\boldsymbol{k}) + \cos^2\theta A_2(\boldsymbol{k})\right]}_{Q^{(1)}(\boldsymbol{k})} \\ + e_i^{(2)}(\boldsymbol{k}) e_j^{(2)}(\boldsymbol{k}) \underbrace{\left[-k^2 A_1(\boldsymbol{k}) + A_2(\boldsymbol{k})\right]}_{Q^{(2)}(\boldsymbol{k})}. \end{aligned} \tag{5.43}$$

From the obtained analytical solutions (5.30) – (5.32), the energy spectral tensors are given by

$$\Phi_{\parallel}(\boldsymbol{\chi},t) = \Phi_{11}(\boldsymbol{\chi},t) = Q^{(2)}(\boldsymbol{k},0)\frac{k^2 k_{23}^2 (1+S_1 t)^2}{\left[k_1^2 + k_{23}^2(1+S_1 t)^2\right]^2}, \tag{5.44}$$

$$\Phi_{22}(\boldsymbol{\chi},t) = \frac{k_3^2}{k_{23}^2} Q^{(1)}(\boldsymbol{k},0) + \frac{Q^{(2)}(\boldsymbol{k},0)\,k_2^2}{k^2}\left(\frac{k_1^2}{k_{23}^2}P^2 + Q^2 - 2\frac{k_1}{k_{23}}PQ\right), \tag{5.45}$$

$$\Phi_{33}(\boldsymbol{\chi},t)=\frac{k_2^2}{k_{23}^2}Q^{(1)}(\boldsymbol{k},0)+\frac{Q^{(2)}(\boldsymbol{k},0)\,k_3^2}{k^2}\left(\frac{k_1^2}{k_{23}^2}P^2+Q^2-2\frac{k_1}{k_{23}}PQ\right), \tag{5.46}$$

$$\begin{aligned}\Phi_{\perp}(\boldsymbol{\chi},t)&=\frac{1}{2}\left[\Phi_{22}(\boldsymbol{\chi},t)+\Phi_{33}(\boldsymbol{\chi},t)\right]\\&=\frac{1}{2}\left[Q^{(1)}(\boldsymbol{k},0)+Q^{(2)}(\boldsymbol{k},0)\,\frac{k^2k_1^2}{\left[k_1^2+k_{23}^2(1+S_1t)^2\right]^2}\right],\end{aligned} \tag{5.47}$$

$$\Phi_{ii}(\boldsymbol{\chi},t)=\Phi_{\parallel}(\boldsymbol{\chi},t)+2\Phi_{\perp}(\boldsymbol{\chi},t)=Q^{(1)}(\boldsymbol{k},0)+Q^{(2)}(\boldsymbol{k},0)\left(P^2+Q^2\right), \tag{5.48}$$

where $Q^{(1)}(\boldsymbol{k},0)=Q^{(11)}(\boldsymbol{k},0)$ and $Q^{(2)}(\boldsymbol{k},0)=Q^{(22)}(\boldsymbol{k},0)$ for simplicity, and $Q^{(1)}(\boldsymbol{k},0)=Q^{(2)}(\boldsymbol{k},0)=\frac{E(k,0)}{4\pi k^2}$ when the initial turbulence is homogeneous isotropic turbulence, where $E(k,0)$ is the energy spectrum. Note that the energy spectral tensor in the compressed direction, $\Phi_{11}(\boldsymbol{\chi},t)$, is related only to the wave mode, $Q^{(2)}(\boldsymbol{k})$; it is not related to the vortex mode, $Q^{(1)}(\boldsymbol{k})$. Therefore, we can interpret the change in variance of u_1 as a direct consequence of the initial distribution of the wave mode with no dependence of the initial vortex mode. Thus, the obtained results depend on the initial complexity of the energy distribution.

In homogeneous turbulence, we have the following relation between the energy spectral tensor, $\Phi_{ij}(\boldsymbol{\chi},t)$, and the enstrophy spectral tensor $\Omega_{ij}(\boldsymbol{\chi},t)$ (Batchelor, 1953):

$$\Omega_{ij}(\boldsymbol{\chi},t)=\left\langle\hat{\omega}_i(\boldsymbol{\chi},t)\,\hat{\omega}_j^*(\boldsymbol{\chi},t)\right\rangle=\chi^2P_{ij}(\boldsymbol{\chi},t)\,\Phi_{ll}(\boldsymbol{\chi},t)-\chi^2\Phi_{ji}(\boldsymbol{\chi},t), \tag{5.49}$$

where $\hat{\omega}_i(\boldsymbol{\chi},t)=\imath\epsilon_{ijk}\chi_j\hat{u}_k(\boldsymbol{\chi},t)$. Thus, from the obtained analytical solutions (5.30)–(5.32), the enstrophy spectral tensors are given by

$$\begin{aligned}\Omega_{\parallel}(\boldsymbol{\chi},t)&=\Omega_{11}(\boldsymbol{\chi},t)=\left\langle\hat{\omega}_1(\boldsymbol{\chi},t)\,\hat{\omega}_1^*(\boldsymbol{\chi},t)\right\rangle\\&=\Omega_{11}(\boldsymbol{k},0)=k_{23}^2Q^{(1)}(\boldsymbol{k},0),\end{aligned} \tag{5.50}$$

$$\begin{aligned}\Omega_{\perp}(\boldsymbol{\chi},t)&=\frac{1}{2}\left[\Omega_{22}(\boldsymbol{\chi},t)+\Omega_{33}(\boldsymbol{\chi},t)\right]\\&=\frac{1}{2}\left[\frac{k_1^2}{(1+S_1t)^2}Q^{(1)}(\boldsymbol{k},0)+\frac{k_1^2+k_{23}^2(1+S_1t)^2}{(1+S_1t)^2}Q^{(2)}(\boldsymbol{k},0)\left(P^2+Q^2\right)\right],\end{aligned} \tag{5.51}$$

$$\begin{aligned}\Omega_{ll}(\boldsymbol{\chi},t) &= \chi^2\Phi_{ll}(\boldsymbol{\chi},t) = \left[\frac{k_1^2}{(1+S_1t)^2}+k_{23}^2\right]\Phi_{ll}(\boldsymbol{\chi},t)\\ &= \frac{k_1^2+k_{23}^2(1+S_1t)^2}{(1+S_1t)^2}\left[Q^{(1)}(\boldsymbol{k},0)+Q^{(2)}(\boldsymbol{k},0)\left(P^2+Q^2\right)\right].\end{aligned} \tag{5.52}$$

As shown in (5.50), it is obvious that the parallel enstrophy spectral tensor is independent of rapid one-dimensional compression.

5.4 Model spectra

In general, there is no precise analytical expression for experimental turbulent energy spectra. To discuss Reynolds number dependency for non-zero viscosity and energy distribution for homogeneous axisymmetric turbulence as an initial state, we used five energy spectra.

5.4.1 Model spectra for homogeneous isotropic turbulence (model spectrum A)

The following model spectrum describes the different forms of energy over a wide range of wavenumbers (Davidson, 2004):

$$E(k) = \frac{K_0\epsilon^{\frac{2}{3}}k^{-\frac{5}{3}}}{\left[1+\frac{3K_0}{2}(kL)^{-\frac{2}{3}}\right]^m}\exp\left[-\frac{3K_0}{2}(k\eta)^{\frac{4}{3}}\right], \tag{5.53}$$

where K_0 corresponds to the Kolmogorov constant, which was set to 1.52 in this study and m corresponds to the parameter that determines the slope of the energy spectrum at low wavenumbers: $E(k\to 0)\sim k^2$ for $m=11/2$ and $E(k\to 0)\sim k^4$ for $m=17/2$. In this study, we adopted a Saffman-type energy spectrum as an initial condition because there is experimental evidence of Saffman turbulence in grid turbulence (see chapter 3). In this study, the model spectrum (5.53) was transformed as a function of Re_λ to investigate the dependency on turbulence of Reynolds number based on the Taylor microscale for the non-zero-viscosity RDT solutions. Using Taylor–Kolmogorov scaling, $\eta/L \approx 15^{\frac{3}{4}}Re_\lambda^{-\frac{3}{2}}$, the transformed

model spectrum is described by

$$E(k) = \frac{K_0 \epsilon^{\frac{2}{3}} k^{-\frac{5}{3}}}{\left[1 + \frac{3K_0}{2}(kL)^{-\frac{2}{3}}\right]^{\frac{11}{2}}} \exp\left[-15 K_0 Re_\lambda^{-2} (kL)^{\frac{4}{3}}\right]. \tag{5.54}$$

In this study, we investigated Re_λ dependencies for non-zero-viscosity RDT (i) $Re_\lambda = 10^2$ and (ii) $Re_\lambda = 10^4$. The turbulent flow at $Re_\lambda = 10^2$ is a typical flow such as grid turbulence, whereas the turbulent flow at $Re_\lambda = 10^4$ is a typical flow such as atmospheric turbulence.

5.4.2 Model spectra for homogeneous axisymmetric turbulence

Sreenivasan & Narasimha (1978) proposed that a homogeneous axisymmetrical tensor can be described by the expansion in zonal harmonics of the two independent scalar functions. A_1 and A_2 can be expanded in zonal harmonics with the Legendre polynominal $P_{2m}(\cos\theta)$ as a basis function.

$$-k^2 A_1(\boldsymbol{k}, \theta) + A_2(\boldsymbol{k}, \theta) = \sum_{m=0}^{\infty} F_{2m}(\boldsymbol{k}) P_{2m}(\cos\theta), \tag{5.55}$$

$$A_2(\boldsymbol{k}, \theta) = \sum_{m=0}^{\infty} G_{2m}(\boldsymbol{k}) P_{2m}(\cos\theta). \tag{5.56}$$

The expansion in terms of spherical harmonics was generalized by Cambon & Teissèdre (1985) for arbitrary anisotropy. This expansion is consistent with that of Sreenivasan & Narasimha (1978) for axisymmetry.

Postulating that some pair of functions A_i, $(i = 1, \ldots, 4)$ depends only on k and not on $\cos\theta$, and using (5.55) and (5.56), a more concrete form of the energy spectral tensor can be obtained. Sreenivasan & Narasimha (1978) proposed the following three ansatzes for homogeneous axisymmetric turbulence:

1. Ansatz 1: A_1 and A_2 depend only on k.
2. Ansatz 2: A_2 and A_3 depend only on k.
3. Ansatz 3: A_1 and A_3 depend only on k.

In these three ansatzes, Ansatz 1 is the simplest model because the angular dependence appears throughout $P_{ij}(\boldsymbol{k})$ and $H_{ij}(\boldsymbol{k})$. Ansatz 2 is the more harmonic form (as compared with Ansatz 1) because it contains higher-order Legendre polynominals, e.g. $F_2(k) P_2(\cos\theta)$. In Ansatz 3, $A_2(k, \cos\theta)$ can be expressed as $A_2(k, \cos\theta) = \frac{1}{\cos^2\theta}[A_3 - k^2 A_1]$, where A_3 and A_1 are functions of k. As mentioned by Sreenivasan & Narasimha (1978), $A_1(k, \cos\theta)$ and $A_2(k, \cos\theta)$ do not depend on the angular dependence when $k^2 A_1 = -A_3$; therefore, they become isotropic forms. On the other hand, $A_2(k, \cos\theta)$ exhibits singularity for $\cos\theta = 0$ when $k^2 A_1 \neq -A_3$.

From the above-mentioned background for the three ansatzes, we used Ansatzes 1 and 2 for the model spectra.

5.4.2.1 Model spectra for Ansatz 1 (model spectrum B)

Ansatz 1 represents what is likely the simplest model for anisotropic turbulence (Nagata *et al.*, 2006). Because A_1 and A_2 are functions of only k in Ansatz 1, the form of $\Phi_{ij}(\boldsymbol{k})$ is obtained using the following simple relation:

$$F_{2m}(k) = G_{2m}(k) = 0, \ m = 1, 2, \ldots. \tag{5.57}$$

Thus, the energy spectral tensor is given by

$$\begin{aligned} \Phi_{ij}(\boldsymbol{k}) &= P_{ij}(\boldsymbol{k})(F_0(k) - G_0(k)) + H_{ij}(\boldsymbol{k}) G_0(k) \\ &= -k^2 P_{ij}(\boldsymbol{k}) A_1(k) + H_{ij}(\boldsymbol{k}) A_2(k). \end{aligned} \tag{5.58}$$

In the expression of the Craya-Herring decomposition, the energy spectral tensor is expressed by

$$\begin{aligned} \Phi_{ij}(\boldsymbol{k}) = &\underbrace{\left[-k^2 A_1(k) + \cos^2\theta A_2(k)\right]}_{Q^{(1)}(\boldsymbol{k})} e_i^{(1)}(\boldsymbol{k}) e_j^{(1)}(\boldsymbol{k}) \\ &+ \underbrace{\left[-k^2 A_1(k) + A_2(k)\right]}_{Q^{(2)}(k)} e_i^{(2)}(\boldsymbol{k}) e_j^{(2)}(\boldsymbol{k}). \end{aligned} \tag{5.59}$$

From the restrictions of the real functions of $Q^{(1)}(\boldsymbol{k})$ and $Q^{(2)}(\boldsymbol{k})$, $A_1(k)$ is negative and $-k^2 A_1(k) + A_2(k) > 0$. In their model spectrum, the forms of A_1 and A_2 are taken to be the exponential forms

$$A_1 = -\mathscr{B}_1 \exp\left(-\mathscr{R}_1 k^2\right), \ A_2 = \mathscr{B}_2 k^2 \exp\left(-\mathscr{R}_2 k^2\right), \tag{5.60}$$

where $\mathscr{B}_1$ and $\mathscr{B}_2$ are constants and $1/\mathscr{R}_1^{1/2}$ and $1/\mathscr{R}_2^{1/2}$ are proportional to the length scales of the isotropic and anisotropic components, respectively. For isotropic turbulence, $\mathscr{B}_2 = 0$, $\mathscr{B}_1 = 1/\pi^4$, and $\mathscr{R}_1 = 1/\pi$.

To determine the unknown coefficients, they prescribed the strength of anisotropy

$$\frac{\int d\boldsymbol{k}\ \Phi_{ii}(\boldsymbol{k})}{\int d\boldsymbol{k}\ \Phi_{11}(\boldsymbol{k})} = \frac{\langle u_i^2 \rangle}{\langle u_1^2 \rangle} = \left[1,\ \frac{1}{R_u},\ \frac{1}{R_u}\right] \text{ (no summation with respect to } i), \tag{5.61}$$

where $R_u = \langle u_1^2 \rangle / \langle u_i^2 \rangle$ represents the anisotropy strength and the relation of one-dimensional spectrum $\Theta_{11}(k_1)$ at $k_1 = 0$ as

$$\Theta_{11}(0) = \frac{u_1^2}{2\pi} \int_{-\infty}^{\infty} dr\ \langle u_1(\boldsymbol{x})\, u_1(\boldsymbol{x} + r\boldsymbol{e}_1) \rangle = \frac{\langle u_1^2 \rangle}{\pi} L_{11}. \tag{5.62}$$

The coefficients in (5.60) are given in Appendix B. Note that R_u is restricted to lie within the range $1 \leq R_u < 2$ so as to satisfy the non-negative Hermitian form of $\Phi_{ij}(\boldsymbol{k})$. When $R_u = 2$, the integral length scale $L_{22,1}\ (= L_{33,1})$ becomes zero, which is unphysical. For more detail, refer to their paper. Their model spectrum is for low-Reynolds-number flow, as seen in the grid turbulence. In the model spectrum for the high-Reynolds-number flow, the forms of A_1 and A_2 are taken to be the von Kármán spectral type as follows:

$$A_1(k) = -\mathscr{B}_1 \frac{1}{\left[1 + (\mathscr{R}_1 k)^2\right]^{\frac{17}{6}}},\ A_2(k) = \mathscr{B}_2 \frac{k^2}{\left[1 + (\mathscr{R}_2 k)^2\right]^{\frac{17}{6}}} \tag{5.63}$$

In a similar way to Nagata *et al.* (2006), the unknown coefficients are obtained and given in Appendix B. In the case of inviscid RDT (as described later), there is no dependency of the forms of A_1 and A_2 on the change in TKE. When the von Kármán forms are adopted, enstrophy is seen to diverge because of the power law form.

5.4.2.2 Model spectra for Ansatz 2 (model spectrum C)

In Ansatz 2, A_2 and A_3 are functions of k. Thus, $G_{2m}(k) = 0$ for $m = 1, 2, \ldots$. In addition, the relation $A_2(k) = G_0(k) = -\frac{3}{2}F_2(k)$ is obtained using $P_2(\cos\theta) = \frac{1}{2}(3\cos^2\theta - 1)$. Finally, the following relations are obtained:

$$G_0(k) = -\frac{3}{2}F_2(k),\ F_{2m+2}(k) = 0 = G_{2m}(k),\ m = 1, 2, \ldots. \tag{5.64}$$

Thus, the energy spectral tensor is given by

$$\Phi_{ij}(\boldsymbol{k}) = P_{ij}(\boldsymbol{k}) F_0(k) + \left[P_{ij}(\boldsymbol{k}) \left(\frac{3}{2} \cos^2\theta + 1 \right) - \frac{3}{2} H_{ij}(\boldsymbol{k}) \right] F_2(k). \quad (5.65)$$

Unlike the form of the energy spectral tensor in Ansatz 1, the angular dependency appears in $A_1(\boldsymbol{k})$. In the expression of the Craya–Herring decomposition, the energy spectral tensor is given by

$$\begin{aligned} \Phi_{ij}(\boldsymbol{k}) = & \underbrace{\left[F_0(k) + F_2(k) \right]}_{Q^{(1)}(k)} e_i^{(1)}(\boldsymbol{k}) e_j^{(1)}(\boldsymbol{k}) \\ & + \underbrace{\left[F_0(k) + \left(\frac{3}{2} \cos^2\theta - \frac{1}{2} \right) F_2(k) \right]}_{Q^{(2)}(\boldsymbol{k})} e_i^{(2)}(\boldsymbol{k}) e_j^{(2)}(\boldsymbol{k}). \end{aligned} \quad (5.66)$$

From the restriction of the real functions of $Q^{(1)}(\boldsymbol{k})$ and $Q^{(2)}(\boldsymbol{k})$, $F_0(k)+F_2(k) > 0$ and $F_0(k) > \frac{1}{2}F_2(k)$. When $F_2(k)$ is negative, $A_2(k)$ is positive. In this case, the magnitude of $F_0(k)$ must be larger than that of $F_2(k)$, regardless of θ.

Similar to Ansatz 1, the exponential forms for $F_0(k)$ and $F_2(k)$

$$F_0(k) = \mathscr{F}_0 k^2 \exp\left(-\mathscr{L}_0 k^2\right), \; F_2(k) = \mathscr{F}_2 k^2 \exp\left(-\mathscr{L}_2 k^2\right), \quad (5.67)$$

and the von Kármán forms

$$F_0(k) = \mathscr{F}_0 \frac{k^2}{\left[1 + (\mathscr{L}_0 k)^2\right]^{\frac{17}{6}}}, \; F_2(k) = \mathscr{F}_2 \frac{k^2}{\left[1 + (\mathscr{L}_2 k)^2\right]^{\frac{17}{6}}}, \quad (5.68)$$

have been adopted, in which the coefficients $\mathscr{L}_0$, $\mathscr{L}_2$, $\mathscr{F}_0$, and $\mathscr{F}_2$ are determined using a similar to the method used for Ansatz 1; they are given in Appendices B.3 and B.4 for the exponential and von Kármán type, respectively.

5.5 Results and Discussions for inviscid RDT

5.5.1 Angular distribution of energy spectral tensor

In homogeneous anisotropic turbulence, there is an angular dependency for $Q^{(1)}(\boldsymbol{\chi}, t)$ and $Q^{(2)}(\boldsymbol{\chi}, t)$. When we discuss the departure from isotropy, it is convenient to

introduce e–z decomposition (Sagaut & Cambon, 2008). For instance, the angular dependency of anisotropic turbulence has been discussed by Cambon *et al.* (1997). However, in this study, the angular distribution of parallel and perpendicular energy spectral tensors are discussed to better understand the phenomena in turbulence-shock wave interactions.

Figures 5.2 and 5.3 show the changes in angular dependency of energy spectral tensors, $\Phi_{\parallel}(\boldsymbol{\chi}, t)$ and $\Phi_{\perp}(\boldsymbol{\chi}, t)$, for model spectra A and B, respectively. In model spectrum A, the spectral tensor has energy at low wavenumbers, and this is caused by the Saffman form at low wavenumbers, whereas in model spectrum B (and C, not shown), the spectral tensor has energy near the inverse of the integral length scale, and this is due to the Batchelor form at low wavenumbers. When initial isotropic conditions are considered, there is a slight change in the angular distribution of $\Phi_{\parallel}(\boldsymbol{\chi}, t)$, whereas energy concentrates to approximately $\theta = \pi/4$ in the angular distribution of $\Phi_{\perp}(\boldsymbol{\chi}, t)$. As shown in figures 5.2 and 5.3, the shock-induced one-dimensional compression (hereinafter simply 'compression') transfers energy to high wavenumbers. This energy transfer was seen in $\Phi_{\perp}(\boldsymbol{\chi}, t)$, regardless of the choice of Ansatz 1 or 2. On the other hand, there was a slight difference in $\Phi_{\parallel}(\boldsymbol{\chi}, t)$ between Ansatzes 1 and 2. These different changes contribute to the changes in one-dimensional spectra at low wavenumbers. As discussed later, the energy changes at $\pi/2$ in $\Phi_{\perp}(\boldsymbol{\chi}, t)$ yield large changes at low wavenumbers in the compressed direction, whereas there are no changes in longitudinal one-dimensional spectra at low wavenumbers because the energy remains at $\pi/2$ in $\Phi_{\parallel}(\boldsymbol{\chi}, t)$.

As shown in figures 5.2 and 5.3, the changes in the energy spectral tensors strongly depend on the initial distributions of the energy spectral tensors. Thus, we can interpret the change in the angular distribution as the effect of the initial anisotropy. When the initial anisotropy is strong, as discussed later, the amplifications of velocity variances are larger than in the case of homogeneous isotropic turbulence. These results suggest that the change in turbulence after compression is different for the near and far regions of the grid turbulence. In fact, these differences have been reported by Agui *et al.* (2005). Regardless of the initial energy spectral tensors, the distribution of $\Phi_{\parallel}(\boldsymbol{\chi}, t)$ tends to concentrate at $\theta = \pi/2$, whereas that of $\Phi_{\perp}(\boldsymbol{\chi}, t)$ tends to concentrate at $\theta = \pi/4$.

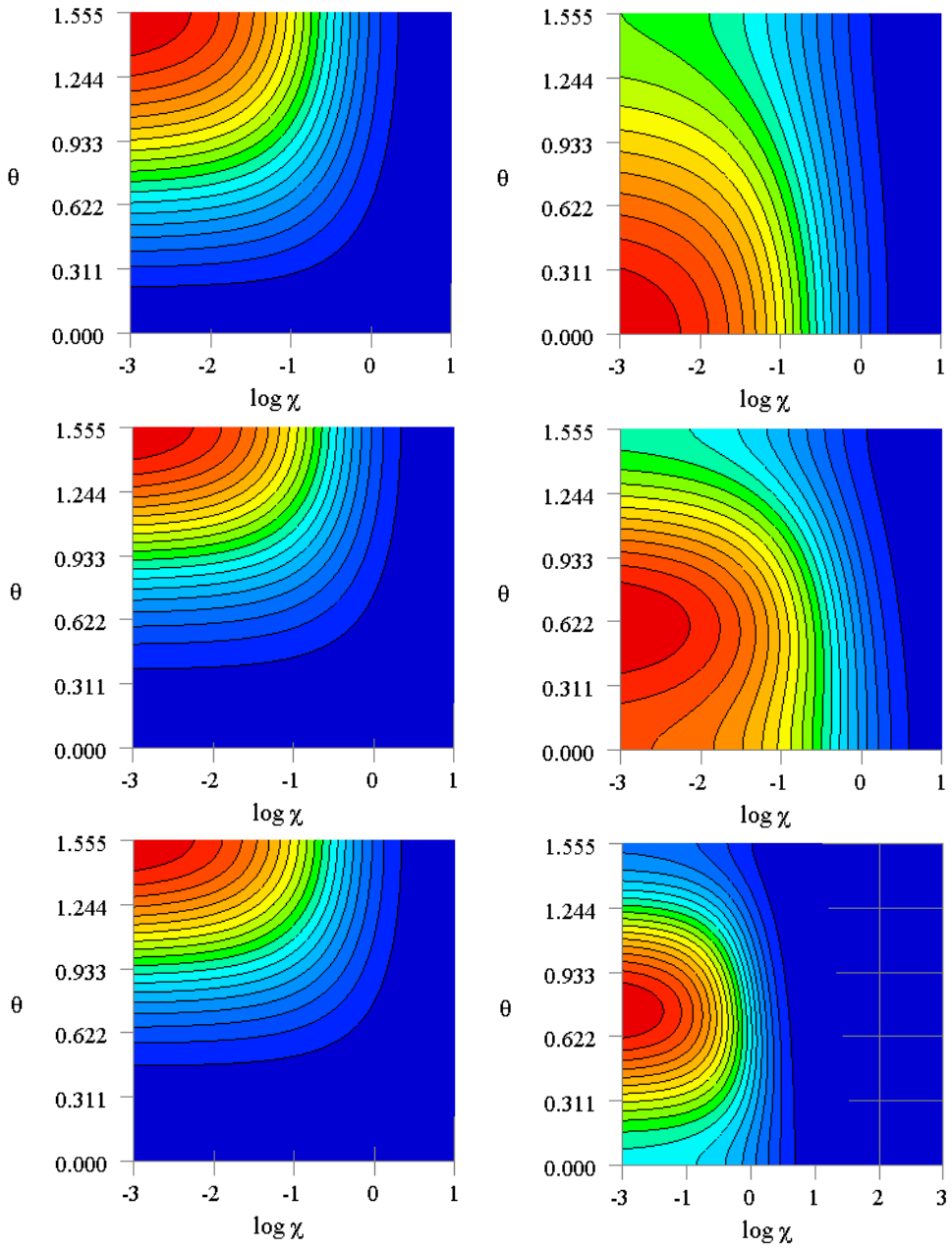

Figure 5.2: The angular distribution of energy spectral tensors in homogeneous isotropic turbulence for model spectrum A (the Saffman-Pao model spectrum, $Re_\lambda = 10^2$) as an initial condition ($\log\chi$–θ plot). The left-side figure shows the angular distribution of $\Phi_\parallel(\boldsymbol{\chi}, t)$. The right-side figures show the angular distribution of $\Phi_\perp(\boldsymbol{\chi}, t)$. The upper, middle, and lower figures correspond to $\overline{\rho}/\rho_0 = 1$, $\overline{\rho}/\rho_0 = 2$, and $\overline{\rho}/\rho_0 = 4$, respectively. Note that each colour contour is normalized by the maximum value in each figure.

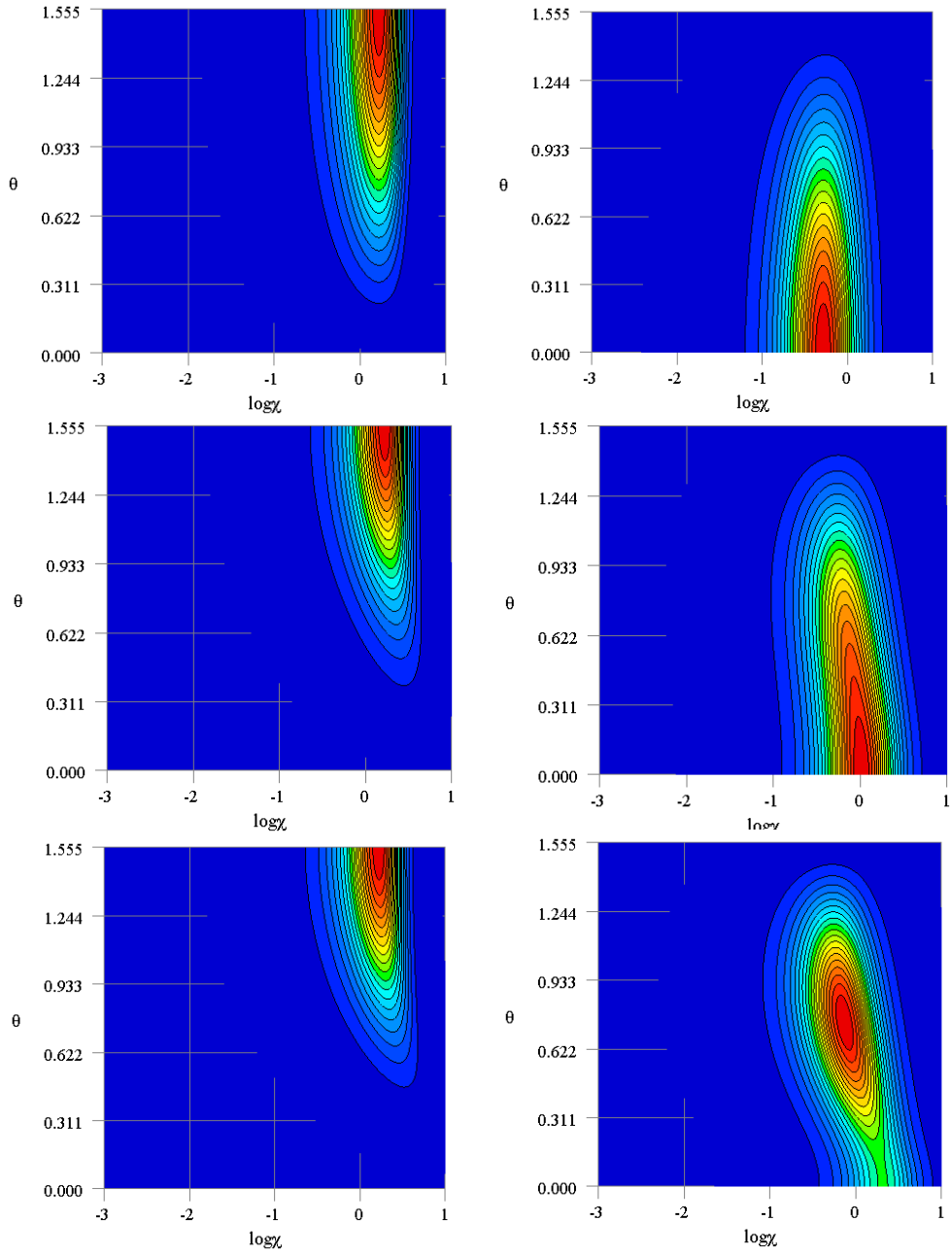

Figure 5.3: The same data as figure 5.2 but for model spectrum B with exponential form and $R_u = 7/4$.

5.5.2 Velocity variances

When isotropic initial conditions are considered, $Q^{(1)}(k) = Q^{(2)}(k) = \frac{E(k)}{4\pi k^2}$. From (5.44), (5.47), and (5.48), the energy spectral tensors are given by

$$\Phi_{\parallel}(\boldsymbol{\chi}, t) = \frac{E(k)}{4\pi k^2}\left[P^2 \sin^2\theta + Q^2\cos^2\theta + 2PQ\sin 2\theta\right], \tag{5.69}$$

$$\Phi_{\perp}(\boldsymbol{\chi}, t) = \frac{E(k)}{8\pi k^2}\left[1 + P^2\cos^2\theta + Q^2\sin^2\theta - 2PQ\sin 2\theta\right], \tag{5.70}$$

$$\Phi_{ll}(\boldsymbol{\chi}, t) = \frac{E(k)}{4\pi k^2}\left[1 + P^2 + Q^2\right], \tag{5.71}$$

where

$$K^s(0) = \int_0^\infty dk\ E(k) \tag{5.72}$$

is the initial TKE of the solenoidal mode. The variances of the parallel and perpendicular velocity fluctuations are given by

$$\begin{aligned}\left\langle u_{\parallel}^2(t)\right\rangle &= \int d\boldsymbol{\chi}\ \Phi_{\parallel}(\boldsymbol{\chi}, t) = \frac{1}{1+S_1 t}\int d\boldsymbol{k}\ \Phi_{\parallel}(\boldsymbol{\chi}, t)\\ &= \frac{K^s(0)}{2}\frac{C^3}{C^2-1}\left[1 + \left(C^2-2\right)\frac{\tan^{-1}\sqrt{C^2-1}}{\sqrt{C^2-1}}\right],\end{aligned} \tag{5.73}$$

$$\begin{aligned}\left\langle u_{\perp}^2(t)\right\rangle &= \int d\boldsymbol{\chi}\ \Phi_{\perp}(\boldsymbol{\chi}, t)\\ &= \frac{CK^s(0)}{2}\left[1 + \frac{C^2}{2\left(C^2-1\right)}\left(-1 + C^2\frac{\tan^{-1}\sqrt{C^2-1}}{\sqrt{C^2-1}}\right)\right],\end{aligned} \tag{5.74}$$

and the TKE of the solenoidal mode is given by

$$\begin{aligned}K^s(t) &= \frac{1}{2}\int d\boldsymbol{\chi}\ \Phi_{ll}(\boldsymbol{\chi}, t) = \frac{1}{1+S_1 t}\int d\boldsymbol{k}\ \Phi_{ll}(\boldsymbol{\chi}, t)\\ &= \frac{K^s(0)}{2}\left[C + C^3\frac{\tan^{-1}\sqrt{C^2-1}}{\sqrt{C^2-1}}\right],\end{aligned} \tag{5.75}$$

where $C = \overline{\rho}/\rho_0$. The limiting cases for (5.73) and (5.74) have been derived by Ribner & Tucker (1953). For Ansatzes 1 and 2, the changes in each velocity variance and TKE value are described in Appendix C. As confirmed by Larsson & Lele (2009) using DNS, the maximum wavenumber, which corresponds to the

resolution in the physical space, is important in turbulence–shock wave interactions. Using RDT analysis, Jacquin *et al.* (1993) obtained the TKE after the compression using the integration range $[k_{0,min} : k_{0,max}]$ for the initial homogeneous isotropic turbulence. However, as shown in the experiment of Barre *et al.* (1996), the TKE at high wavenumbers increases behind a shock wave. Furthermore, Larsson & Lele (2009) showed that different numerical resolutions yielded different amplification ratios of velocity variance, and that their DNS results were different from those of Lee *et al.* (1997) and LIA. Therefore, the maximum wavenumber, which corresponds to the resolution in the physical space, plays an important role in the statistical quantities of turbulence. In homogeneous turbulence, TKE dissipation of the solenoidal mode is expressed by $\epsilon^s = \nu \langle \boldsymbol{\omega}^2 \rangle$. Thus, the Kolmogorov length scale is expressed by $\eta = \left(\frac{\nu^2}{\langle \boldsymbol{\omega}^2 \rangle} \right)^{\frac{1}{4}} = \left(\frac{\overline{\mu}^2}{\overline{\rho}^2 \langle \boldsymbol{\omega}^2 \rangle} \right)^{\frac{1}{4}}$, and the ratio between the Kolmogorov length scale after and before the interaction with a shock wave can be written as follows using $\sqrt{\langle \boldsymbol{\omega}^2 \rangle} / \sqrt{\langle \boldsymbol{\omega}_0^2 \rangle} \sim \overline{\rho}/\rho_0$ (Mahesh *et al.*, 1997):

$$\frac{k_{0,max}}{k_{max}} = \frac{\eta}{\eta_0} = \left(\frac{\overline{\mu}^2 \rho_0^4}{\mu_0^2 \overline{\rho}^4} \right)^{\frac{1}{4}} = \left(\frac{\rho_0^4}{\overline{\rho}^4} f\left(\overline{T}\right) \right)^{\frac{1}{4}}, \tag{5.76}$$

where $\left(\overline{\mu}/\mu_0\right)^2 = f\left(\overline{T}\right)$ indicates that $\overline{\mu}$ is an increasing function of temperature $\overline{T}$. Larsson & Lele (2009) proposed the maximum wavenumber of $k_{max}/k_{0,max} = \left(\overline{\rho}/\rho_0\right)\left(T_0/\overline{T}\right)^{\frac{3}{8}}$. Here, we adopted the maximum wavenumber of $k_{max} > \frac{\overline{\rho}}{\rho_0} k_{0,max}$ in the numerical calculation. Figures 5.4 (a) and (b) show the changes in TKE and the changes in $\eta/\eta_0 \left(= k_{0,max}/k_{max}\right)$. When we set the the maximum wavenumber to $k_{max} > \frac{\overline{\rho}}{\rho_0} k_{0,max}$, the obtained results agreed with the exact solution (5.75). On the other hand, when we set the maximum wavenumber to $k_{max}/k_{0,max} = \left(\overline{\rho}/\rho_0\right)\left(T_0/\overline{T}\right)^{\frac{3}{8}}$ as used in Larsson & Lele (2009) and Larsson *et al.* (2013), the TKE amplification is underestimated in the RDT analysis. As confirmed by high-resolution DNS of Larsson & Lele (2009), the obtained results depend on the resolution. Furthermore, our RDT results suggest that the dependence on the resolution for the statistical quantities becomes remarkable with the increase of Mach number. Thus, RDT analysis strongly suggests that high-resolution DNS is needed to obtain the accurate results for the turbulence-shock wave interactions, especially for high Mach number flows. Of course, RDT is based on a linear theory and requirements of grid resolution for high Mach number flows should

be carefully examined using DNS in the future study. TKE amplification of the DNS results of Grube *et al.* (2011) is shown in figure 5.4; their result is in good agreement with the RDT analysis. LIA result in the near field (Jacquin *et al.*, 1993) is also included in figure 5.4. Based on this result, $k_{max} > \frac{\bar{\rho}}{\rho_0} k_{0,max}$ is used for the RDT analysis with non-zero viscosity in §5.6.

Figure 5.5 (a) shows the amplification of TKE for the initial homogeneous axisymmetric turbulence. The amplification of TKE depends on the initial degree of anisotropy; however, there is almost no dependency on the difference between Ansatzes 1 and 2. As discussed later, the amplification of $\langle u_\perp^2(t) \rangle$ contributes to the amplification of TKE for the initial homogeneous axisymmetric turbulence. Figure 5.5 (b) shows the changes in velocity anisotropy $\left\langle u_\parallel^2(t) \right\rangle / \left\langle u_\parallel^2(0) \right\rangle / (\langle u_\perp^2(t) \rangle / \langle u_\perp^2(0) \rangle)$. The results of Larsson *et al.* (2013) for the far region are also included for reference. The changes in anisotropy against $\overline{\rho}/\rho_0$ for RDT are closer to the DNS results rather than the LIA result. Here, it is worth mentioning the difference between RDT and LIA. First, the changes in the TKE in the near regions are associated with the energy transfer from the acoustic potential energy in LIA. However, such changes are not incorporated into RDT. Thus, the predictive capabilities of the RDT analysis for turbulence-shock interaction are limited only for the vicinity of the shock wave. In the vicinity of the shock wave, RDT result qualitatively agrees with the DNS result (Larsson & Lele, 2009) in that the parallel component of the velocity fluctuations are amplified more than the perpendicular component. However, LIA result shows the opposite result for $M_s = 2.0$ (Lee *et al.*, 1997). This means that RDT is more accurate in the vicinity of the shock wave, whereas it cannot predict the statistical quantities for the far field. Then, RDT does not take into account of the entropy fluctuations. It is known that the entropy fluctuations are more significant than acoustic fluctuations for high Mach number flows. Thus, the present RDT analysis is no longer valid for the inflow having the entropy fluctuations.

Figure 5.6 shows the changes in $\left\langle u_\parallel^2(t) \right\rangle$ and $\langle u_\perp^2(t) \rangle$. As shown in figure 5.6, the changes in the variance of each velocity component depend on the initial degree of anisotropy, For the changes in $\langle u_\perp^2(t) \rangle$, Ansatzes 1 and 2 yield different amplifications. When the isotropic initial conditions are considered, the anisotropy of the velocity components is significant; however, the anisotropy of

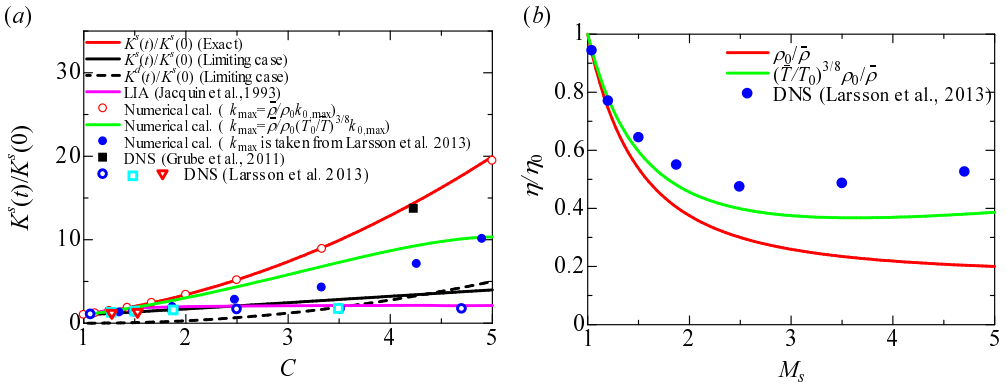

Figure 5.4: The amplification of TKE versus the inviscid RDT solution for the initial homogeneous isotropic turbulence. Also included are the changes in TKE from the LIA (near field) result of Jacquin *et al.* (1993) and the DNS result of Grube *et al.* (2011) with the initial conditions $Re_\lambda = 26$, $M_t = 0.52$, and $M_1 = 3.46$, and Larsson *et al.* (2013) with the initial condition $Re_\lambda \approx 40$, where M_1 is the Mach number of the upstream of a shock wave.

the velocity components is not significant when the initial anisotropy is strong. However, this strong anisotropy cannot be seen in fully developed grid turbulence, as already shown in figure 5.5 (b). Thus, the anisotropy of the velocity components may be a general consequence of homogeneous isotropic turbulence–shock wave interactions.

As shown in the DNS of Grube *et al.* (2011), there is a slight contribution from the nonlinear term in the energy budget; however, note that the compressible contribution is much larger than the nonlinear effect. In addition, there is a slight contribution of baroclinic effect. Following Kevlahan & Hunt (1997), we simply evaluate the evolution of the nonlinear term of the solenoidal mode by means of the primitive perturbation method. Non-dimensionalizing the equation for $\hat{u}_i^s(\boldsymbol{\chi}, t)$, and $\boldsymbol{\chi}$ by the initial integral scale and the initial r.m.s. velocity u_0,

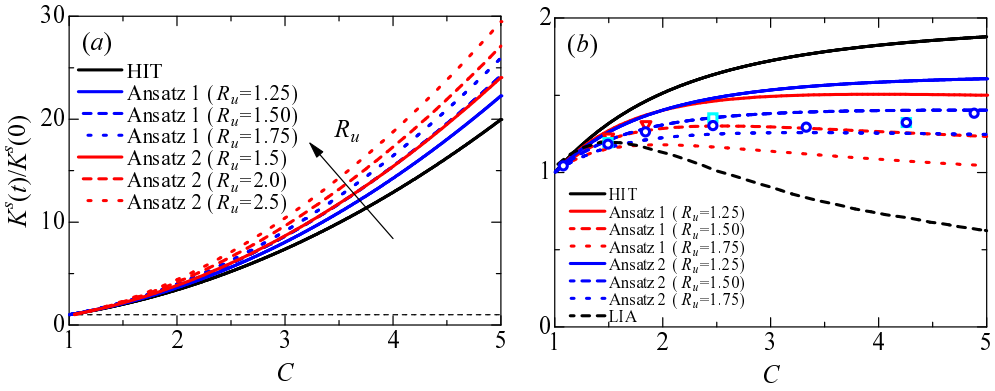

Figure 5.5: (a) The amplification of TKE versus the inviscid RDT solution for the initial homogeneous axisymmetric turbulence. (b) The changes in $\left\langle u_{\parallel}^2(t)\right\rangle / \left\langle u_{\parallel}^2(0)\right\rangle / (\langle u_{\perp}^2(t)\rangle / \langle u_{\perp}^2(0)\rangle)$. The symbols are taken from the DNS of Larsson *et al.* (2013); their results correspond to the post-shock turbulence anisotropy in the far field.

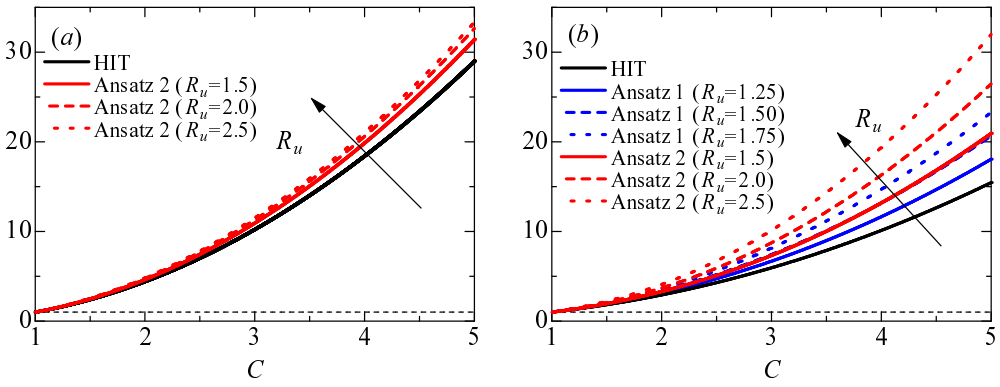

Figure 5.6: The amplification of velocity variances versus the inviscid RDT solution. (a) The variance of parallel velocity components, $\left\langle u_{\parallel}^2(t)\right\rangle / \left\langle u_{\parallel}^2(0)\right\rangle$, and (b) the variance in perpendicular velocity components, $\langle u_{\perp}^2(t)\rangle / \langle u_{\perp}^2(0)\rangle$. Note that the changes in variance of the parallel velocity components for Ansatz 1 are the same as those for the initial homogeneous isotropic turbulence, regardless of the initial anisotropy.

(5.18) and (5.19) become

$$\begin{aligned}\frac{d\hat{u}_i^s(\boldsymbol{\chi},t)}{dt} &= -\frac{\chi^2}{Re_L\left(1-\frac{t}{\delta}\right)^{n(\kappa-1)-1}}\hat{u}_i^s(\boldsymbol{\chi},t) \\ &+ \left[\Pi_{i1}(\boldsymbol{\chi}) - P_{i1}(\boldsymbol{\chi})\right]\frac{-1}{\delta\left(1-\frac{t}{\delta}\right)}\hat{u}_1^s(\boldsymbol{\chi},t) + N_i^s\left(\hat{\boldsymbol{u}}(\boldsymbol{\chi},t),\boldsymbol{\chi},t\right),\end{aligned} \tag{5.77}$$

$$\chi_1(t) = \frac{k_1}{1-\frac{t}{\delta}},\ \chi_2(t) = k_2,\ \chi_3(t) = k_3, \tag{5.78}$$

where $\delta = (u_0/L)/\mid S_1 \mid \ll 1$ is the ratio of the strain rate of the energy-containing eddies to the strength of compression, and $Re_L = u_0 L/\nu$ is the Reynolds number. $N_i^s\left(\hat{\boldsymbol{u}}(\boldsymbol{\chi},t),\boldsymbol{\chi},t\right)$ is the nonlinear term. Furthermore, we change the variable $\tau = t/\delta$ in the dimensionless equations, and the RDT equations become

$$\begin{aligned}\frac{d\hat{u}_i^s(\boldsymbol{\chi},\tau)}{d\tau} &= -\frac{\delta\chi^2}{Re_L(1-\tau)^{n(\kappa-1)-1}}\hat{u}_i^s(\boldsymbol{\chi},\tau) \\ &+ \left[\Pi_{i1}(\boldsymbol{\chi}) - P_{i1}(\boldsymbol{\chi})\right]\frac{-1}{(1-\tau)}\hat{u}_1^s(\boldsymbol{\chi},\tau) + \delta P_{ij}(\boldsymbol{\chi})N_j\left(\hat{\boldsymbol{u}}(\boldsymbol{\chi},t),\boldsymbol{\chi},\tau\right),\end{aligned} \tag{5.79}$$

$$\chi_1(\tau) = \frac{k_1}{1-\tau},\ \chi_2(\tau) = k_2,\ \chi_3(\tau) = k_3. \tag{5.80}$$

Expanding $\hat{u}_i(\boldsymbol{\chi},t)$ as a perturbation series in the ordering parameter δ, we obtain

$$\hat{u}_i(\boldsymbol{\chi},t) = \hat{u}_i^{(0)}(\boldsymbol{\chi},t) + \delta\hat{u}_i^{(1)}(\boldsymbol{\chi},t) + O\left(\delta^2\right). \tag{5.81}$$

Equating the powers of δ, the zeroth-order equation implies neglecting the nonlinear terms, which are of order δ (while retaining the viscous terms), which leads to the following solutions:

$$\hat{u}_1^{s(0)}(\boldsymbol{\chi},\tau) = \beta_1(\boldsymbol{k},\tau)\,\hat{u}_1^s(\boldsymbol{k},0)\,f_v(\boldsymbol{k},\tau), \tag{5.82}$$

$$\hat{u}_2^{s(0)}(\boldsymbol{\chi},\tau) = \beta_2(\boldsymbol{k},\tau)\,\hat{u}_1^s(\boldsymbol{k},0)\,f_v(\boldsymbol{k},\tau) + \hat{u}_2^s(\boldsymbol{k},0)\,f_v(\boldsymbol{k},\tau), \tag{5.83}$$

$$\hat{u}_3^{s(0)}(\boldsymbol{\chi},\tau) = \beta_3(\boldsymbol{k},\tau)\,\hat{u}_1^s(\boldsymbol{k},0)\,f_v(\boldsymbol{k},\tau) + \hat{u}_3^s(\boldsymbol{k},0)\,f_v(\boldsymbol{k},\tau), \tag{5.84}$$

where $\beta_i(\boldsymbol{k},\tau)$ are given by

$$\beta_1(\boldsymbol{k},\tau) = \frac{k^2(1-\tau)}{k_1^2 + k_{23}^2(1-\tau)^2}, \tag{5.85}$$

$$\beta_i(\boldsymbol{k},\tau) = -\frac{k_1 k_i \tau(2-\tau)}{k_1^2 + k_{23}^2(1-\tau)^2} \quad (i = 2 \text{ or } 3), \tag{5.86}$$

and $f_v(\boldsymbol{k},\tau)$ is the viscous decay factor, which is given by

$$f_v(\boldsymbol{k},\tau) = \exp\left[\frac{1}{Re_L}\left[\frac{k_1^2\left((1-\tau)^{n(1-\kappa)}-1\right)}{n(1-\kappa)} + \frac{k_{23}^2\left((1-\tau)^{n(1-\kappa)+2}-1\right)}{n(1-\kappa)+2}\right]\right]. \tag{5.87}$$

The nonlinear terms of the solenoidal mode are expanded in terms of $\hat{\boldsymbol{u}}^{(0)}(\boldsymbol{\chi},t)$ as

$$\begin{aligned} N_i^s(\boldsymbol{\chi},\tau) &= -\imath P_{ij}(\boldsymbol{\chi}) \int_{\boldsymbol{\chi}=\boldsymbol{p}+\boldsymbol{q}} d\boldsymbol{p}\; q_n \hat{u}_n(\boldsymbol{p},\tau)\,\hat{u}_j(\boldsymbol{q},\tau) \\ &= P_{ij}(\boldsymbol{\chi})\, N_j^{(0)}\left(\hat{\boldsymbol{u}}^{(0)}(\boldsymbol{\chi},\tau),\boldsymbol{\chi},\tau\right) + O(\delta), \end{aligned} \tag{5.88}$$

where $\boldsymbol{\chi} = \boldsymbol{p} + \boldsymbol{q}$ is called a resonant triad condition, which is the hallmark of incompressible fluids, whereas $\boldsymbol{\chi} = \boldsymbol{p} + \boldsymbol{q} + \boldsymbol{r}$ appears in compressible fluids without the assumption of $\overline{\rho} \gg \rho'$. Here, the zeroth- and first-order nonlinear terms are shown in figure 5.7 using the diagram representation. In the diagram representation of the perturbation series, the nonlinear terms can be written by representing the main constituents such as $\hat{\boldsymbol{u}}^{(0)}$, $G^{(0)}$ and the projectors (5.14). As shown in figure 5.7, there are four convolutions in the zeroth-order nonlinear term. The first-order correction $\hat{u}_i^{s(1)}(\boldsymbol{\chi},\tau)$ to the RDT approximation is the solution to the equations

$$\begin{aligned} \frac{d\hat{u}_i^{s(1)}(\boldsymbol{\chi},\tau)}{d\tau} &= -\frac{\delta\chi^2}{Re_L(1-\tau)^{n(\kappa-1)-1}}\hat{u}_i^{s(1)}(\boldsymbol{\chi},\tau) \\ &\quad + \left[\Pi_{i1}(\boldsymbol{\chi}) - P_{i1}(\boldsymbol{\chi})\right]\frac{-1}{(1-\tau)}\hat{u}_1^{s(1)}(\boldsymbol{\chi},\tau) + P_{ij}(\boldsymbol{\chi})\, N_j^{(0)}\left(\hat{\boldsymbol{u}}(\boldsymbol{\chi},t),\boldsymbol{\chi},\tau\right), \end{aligned} \tag{5.89}$$

where

$$\hat{u}_i^{s(1)}(\boldsymbol{\chi},\tau) = \int_0^\tau ds\; G_{im}^{s(0)}(\boldsymbol{\chi},\tau,s)\, P_{mj}(\boldsymbol{\chi})\, N_j^{(0)}\left(\hat{\boldsymbol{u}}^{(0)}(\boldsymbol{\chi},s),\boldsymbol{\chi},s\right) \tag{5.90}$$

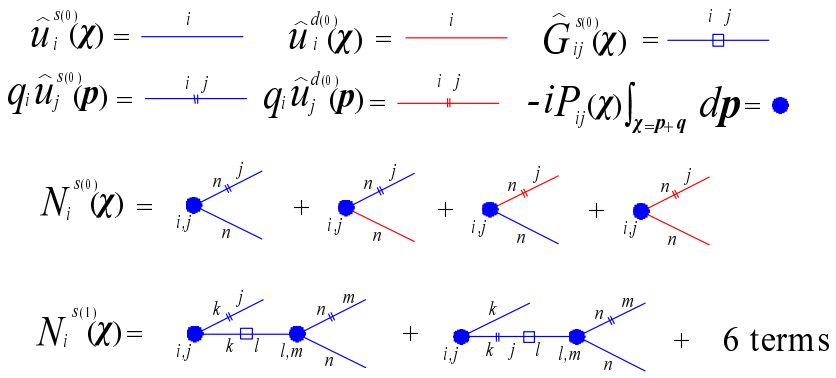

Figure 5.7: Diagram representation of the nonlinear terms. Blue lines correspond to the solenoidal mode. Red lines correspond to the dilatational mode. $\hat{\boldsymbol{u}}^{s(0)}$ correspond to the RDT solutions (5.82), (5.83) and (5.84).

where

$$G_{1m}^{s(0)}\left(\boldsymbol{\chi},\tau,s\right)=\beta_1\left(\boldsymbol{k},\tau\right)\beta_1^{-1}\left(\boldsymbol{k},s\right)f_v\left(\boldsymbol{k},\tau\right)f_v^{-1}\left(\boldsymbol{k},s\right)P_{1m}\left(\boldsymbol{\chi}\right), \tag{5.91}$$

$$\begin{aligned}G_{im}^{s(0)}\left(\boldsymbol{\chi},\tau,s\right)=&\left(\beta_i\left(\boldsymbol{k},\tau\right)-\beta_i\left(\boldsymbol{k},s\right)\right)\beta_1^{-1}\left(\boldsymbol{k},s\right)f_v\left(\boldsymbol{k},\tau\right)f_v^{-1}\left(\boldsymbol{k},s\right)P_{1m}\left(\boldsymbol{\chi}\right)\\&+f_v\left(\boldsymbol{k},\tau\right)f_v^{-1}\left(\boldsymbol{k},s\right)P_{im}\left(\boldsymbol{\chi}\right),\ \left(i=2\text{ or }3\right).\end{aligned} \tag{5.92}$$

In the zeroth nonlinear term, the largest contribution to the first-order correction $\hat{u}_i^{s(1)}\left(\boldsymbol{\chi},\tau\right)$ to the RDT approximations is the convolution of the solenoidal modes when the initial conditions consist of the solenoidal mode. In fact, the contribution of the dilatational mode to the amplification of TKE is less than that of the solenoidal mode (Jacquin *et al.*, 1993). Thus, the evolutions of both the solenoidal mode and the dilatational mode are primarily caused by the change in the solenoidal mode (blue lines in figure 5.7), and the contribution of the first-order correction can be interpreted as an indirect effect of the Rankine-Hugoniot relation throughout the perturbation manner.

Regarding the answer to the first question of Andreopoulos *et al.* (2000), in this study, we cannot concretely determine how much of the TKE amplification after the interaction is caused solely by the Rankine–Hugoniot relation, because some causes of TKE amplification were neglected, e.g. the curved shock effect,

the baroclinic effect, and so on. However, present RDT analysis implies that the amplification of TKE after the interaction is a direct consequence of the Rankine–Hugoniot relation, because the RDT governing equations for one-dimensional compression satisfy the Rankine–Hugoniot relation as to the mean density and mean pressure, and the effect of the nonlinear term contributes to the amplification of TKE through the perturbation manner. Thus, the effect of the nonlinear term can be interpreted as an indirect consequence via the Rankine–Hugoniot relation.

5.5.3 Vorticity variances

When the isotropic initial conditions are considered, the variances of parallel and perpendicular vorticity after compression are given by

$$\left\langle \omega_{\parallel}^{2}\left(t\right)\right\rangle =\int d\boldsymbol{\chi}\;\Omega_{\parallel}\left(\boldsymbol{\chi},t\right)=C\left\langle \omega_{\parallel}^{2}\left(0\right)\right\rangle =\frac{C}{3}\left\langle \boldsymbol{\omega}^{2}\left(0\right)\right\rangle , \tag{5.93}$$

$$\left\langle \omega_{\perp}^{2}\left(t\right)\right\rangle =\int d\boldsymbol{\chi}\;\Omega_{\perp}\left(\boldsymbol{\chi},t\right)=\frac{C^{3}}{3}\left\langle \boldsymbol{\omega}^{2}\left(0\right)\right\rangle , \tag{5.94}$$

and the enstrophy is given by

$$\left\langle \boldsymbol{\omega}^{2}\left(t\right)\right\rangle =\int d\boldsymbol{\chi}\;\chi^{2}\Phi_{ll}\left(\boldsymbol{\chi},t\right)=\frac{C\left(2C^{2}+1\right)}{3}\left\langle \boldsymbol{\omega}^{2}\left(0\right)\right\rangle . \tag{5.95}$$

Regarding Ansatzes 1 and 2, the changes in each vorticity variance and enstrophy are described in Appendix C. As shown in figure 5.8, the variance of the perpendicular vorticity, $\langle\omega_{\perp}^{2}\rangle$, is amplified more than that of the parallel vorticity, $\left\langle\omega_{\parallel}^{2}\right\rangle$. Similar results have been obtained in the DNSs of Lee *et al.* (1993, 1997), Larsson & Lele (2009), and Grube *et al.* (2011). Regarding the limiting case of inviscid RDT analysis, $\left\langle\omega_{\parallel}^{2}\right\rangle$ does not change throughout the interaction. In the experiments of Agui *et al.* (2005), they showed that $\left\langle\omega_{\parallel}^{2}\right\rangle$ was slightly reduced after the interaction. Using RDT analysis, their results may be interpreted as being caused by the lack of the resolution (which may correspond to the limiting case in the RDT analysis). In fact, high-resolution DNS of Grube *et al.* (2011) showed slight amplification of $\left\langle\omega_{\parallel}^{2}\right\rangle$.

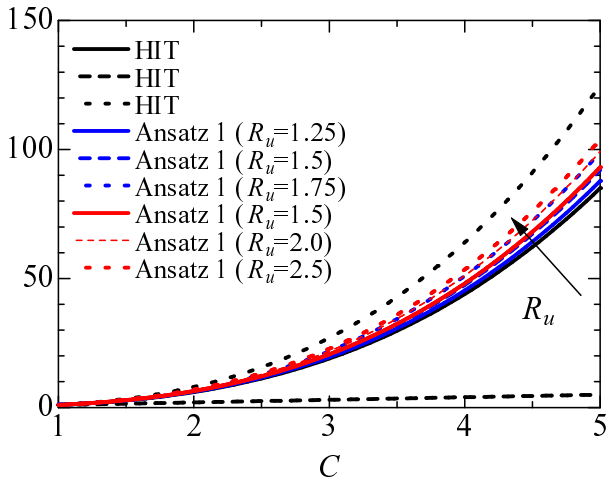

Figure 5.8: The amplification of vorticity variances in inviscid RDT. The black solid, dashed, and dotted lines correspond to the changes in $\langle \boldsymbol{\omega}^2(t)\rangle / \langle \boldsymbol{\omega}^2(0)\rangle$, $\left\langle \omega_\parallel^2(t)\right\rangle / \left\langle \omega_\parallel^2(0)\right\rangle$ and $\langle \omega_\perp^2(t)\rangle / \langle \omega_\perp^2(0)\rangle$, respectively, for the initial homogeneous isotropic turbulence. The blue and red lines correspond to the changes in $\langle \boldsymbol{\omega}^2(t)\rangle / \langle \boldsymbol{\omega}^2(0)\rangle$ for the initial homogeneous axisymmetric turbulence of Ansatzes 1 and 2, respectively.

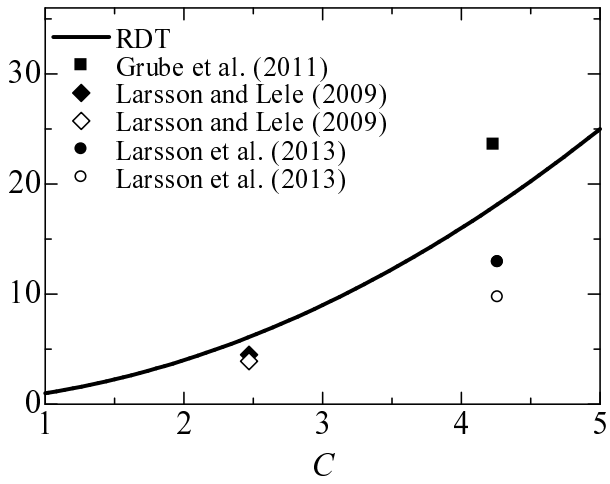

Figure 5.9: The change in vorticity anisotropy $\langle\omega_\perp^2\rangle / \left\langle\omega_\parallel^2\right\rangle$. We also present the DNS results of Larsson & Lele (2009), Larsson *et al.* (2013) and Grube *et al.* (2011). The black and white diamonds correspond to the DNS results of the initial conditions $M_s = 1.87$ and $M_t = 0.22$, and grids with 1040×384^2 and 174×64^2, respectively (Larsson & Lele, 2009). The black and white circles correspond to the DNS results of the initial conditions $Re_\lambda = 40$ and $Re_\lambda = 74$ with $M_s = 3.5$ and $M_t = 0.16$, respectively (Larsson *et al.*, 2013). The initial conditions of Grube *et al.* (2011) are the same as those in figure 5.4 (a).

Figure 5.9 shows the change in vorticity anisotropy. The results of Larsson & Lele (2009), Larsson *et al.* (2013), and Grube *et al.* (2011) are also shown. As discussed by Larsson & Lele (2009), the effect of resolution yields different results in the process of the return to isotropy behind a shock wave. In fact, the vorticity anisotropy of high-resolution DNS is closer to the RDT result than that of low resolution DNS. Compared to the anisotropy of the velocity field, the anisotropy of the vorticity fields is significant. This phenomenon is due to the anisotropy at small scales after the interaction.

For the answer to the second question of Andreopoulos *et al.* (2000), the amplification of vorticity relates to the changes in wavenumber and the amplification of energy at high wavenumbers. Because the enstrophy can be calculated from (5.95), the integrand is given by $\chi^2\Phi_{ii}(\boldsymbol{\chi}, t)$, which can be approximated by $C^2 k_1^2 \Phi_{ii}(\boldsymbol{\chi}, t)$ by neglecting the related term k_{23}^2. Thus, the vorticity fluctuations are amplified more than the velocity fluctuations with order $C^2\left(=(\overline{\rho}/\rho_0)^2\right)$. Then, as described later, the shock-induced compression transfers energy to the fluctuating components, and redistributes energy in the Fourier space. As a consequence of these effects, the energy at small eddies is amplified and contributes to the amplification of vorticity fluctuations.

5.5.4 Spectra

The one-dimensional energy spectrum for the χ_1 direction is given by

$$\Theta_{ij}(\chi_1, t) = \int_0^\infty \int_0^\infty \Phi_{ij}(\boldsymbol{\chi}, t)\, d\chi_2 d\chi_3 = \int_{\chi_1}^\infty \int_0^{2\pi} \Phi_{ij}(\boldsymbol{\chi}, t)\, \chi d\chi d\phi. \tag{5.96}$$

Although one-dimensional energy spectra can be calculated analytically, we investigated them numerically because of the cumbersome algebra. Figure 5.10 shows the one-dimensional energy spectra in exponential form for initial conditions with $R_u = 7/4$ for Ansatz 1. We confirmed that the main differences between the exponential form and the von Kármán form are apparent at high wavenumbers. Similar results are obtained for Ansatz 2, although differences between Ansatzes 1 and 2 are apparent at low wavenumbers.

Regardless of the initial forms of the energy spectra, the energy at high wavenumbers is amplified more than that at low wavenumbers. Regarding the

changes in energy spectra at low wavenumbers, the changes in $\Theta_{\perp}\left(\chi_{|},t\right)$ are larger than those in $\Theta_{\parallel}\left(\chi_{|},t\right)$. These results correspond to the changes in the integral length scales, as described later.

Regarding the changes in the normalized one-dimensional energy spectrum $\Theta_{\parallel}\left(\chi_{|},t\right)/\left\langle u_{\parallel}^{2}\left(t\right)\right\rangle$, RDT results qualitatively agree with the experimental results of Barre *et al.* (1996), and Agui *et al.* (2005); however, note that these results are different from the experimental results of Honkan & Andreopoulos (1992), who showed that the energy of large eddies is amplified more than that of small eddies. In RDT analysis, although turbulence is treated as homogeneous turbulence, inhomogeneous effects will appear in large eddy structures after interaction with a shock wave. However, RDT analysis may yield good results for changes in small eddies, because the local homogeneities can be assumed for high-Reynolds-number flows.

For the answer to the third question of Andreopoulos *et al.* (2000), the amplification of energy at high wavenumbers is due to the extension of wavenumber. In terms of energy exchange, the shock-induced compression transfers energy to the fluctuating components, and redistributes energy in the Fourier space. These energy transfers are seen at high wavenumbers; as a consequence, the distant triad interactions, $\max\left(k,p,q\right)/\min\left(k,p,q\right)\gg 1$, will be more dominant than the local triad interactions, $\max\left(k,p,q\right)/\min\left(k,p,q\right)\sim 1$, in the small eddies when nonlinear effects are considered. These conclusions are based on the basic principles of RDT analysis.

5.5.5 Turbulence characteristic length scales

The integral length scale $L_{ij,n}$ is defined by the integration of the cross-correlation coefficient $r_{ij}\left(\xi\boldsymbol{e}_{n}\right)$ from zero to infinity; it is given by

$$L_{ij,n}\left(t\right)=\int_{0}^{\infty}d\xi\ r_{ij}\left(\xi\boldsymbol{e}_{n}\right)=\frac{1}{\left\langle u_{i}u_{j}\right\rangle}\int_{0}^{\infty}d\xi\ \left\langle u_{i}\left(\boldsymbol{x}\right)u_{j}\left(\boldsymbol{x}+\xi\boldsymbol{e}_{n}\right)\right\rangle . \tag{5.97}$$

In homogeneous turbulence,

$$L_{ij,n}\left(t\right)=\frac{\pi}{\left\langle u_{i}u_{j}\right\rangle}\int_{-\infty}^{\infty}d\boldsymbol{\chi}_{m}\int_{-\infty}^{\infty}d\boldsymbol{\chi}_{l}\ \Phi_{ij}\left(\boldsymbol{\chi},t\right)|_{\chi_{n}=0}, \tag{5.98}$$

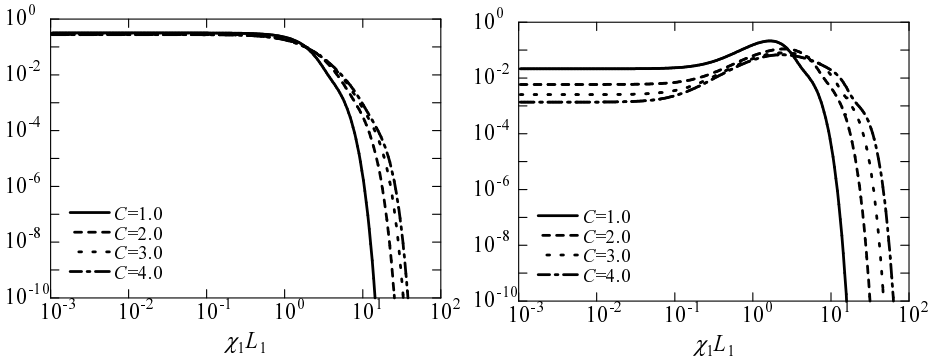

Figure 5.10: Normalized one-dimensional power spectra in the exponential form (left) $\Theta_{\parallel}\left(\chi_{|},t\right)/\left\langle u_{\parallel}^{2}\left(t\right)\right\rangle$ and (right) $\Theta_{\perp}\left(\chi_{|},t\right)/\left\langle u_{\perp}^{2}\left(t\right)\right\rangle$ for Ansatz 1 with $R_u = 7/4$ as an initial condition.

where $\boldsymbol{\chi}_m\,(=\chi_m \boldsymbol{e}_m)$ is the vector orthogonal to $\boldsymbol{\chi}_n\,(=\chi_n \boldsymbol{e}_n)$ and $\boldsymbol{\chi}_l\,(=\chi_l \boldsymbol{e}_l)$ is the vector orthogonal to both $\boldsymbol{\chi}_m$ and $\boldsymbol{\chi}_n$. Therefore, the integral length scale can be calculated from the planar integral.

When the isotropic initial conditions are considered, the longitudinal integral length scale (e.g. $L_{11,1} = L_{22,2} = L_{33,3}$) is defined as (Batchelor, 1953)

$$L_f = \frac{3\pi}{4K^s}\int_0^{\infty}\frac{E\left(k\right)}{k}dk, \tag{5.99}$$

where the lateral integral length scale is $L_g = \frac{1}{2}L_f$.

The analytical solutions of the integral length scales are presented in Appendix C. Figure 5.11 shows the changes in the integral length scales for the initial homogeneous isotropic turbulence. As shown in figure 5.11, most integral length scales [e.g. $L_{11,1}$, $L_{22,2}\,(=L_{33,3})$, and $L_{22,1}\,(=L_{33,1})$, $L_{11,2}\,(=L_{11,3})$] decrease after the compression, whereas $L_{22,3}\,(=L_{33,2})$ increases. In these integral length scales, $L_{22,1}\,(=L_{33,1})$ is significantly reduced after the compression. When the initial isotropic conditions are considered, there are no differences between $L_{11,1}$ and $L_{11,2}\,(=L_{11,3})$; however, one can see the differences between them for the initial homogeneous axisymmetric turbulence.

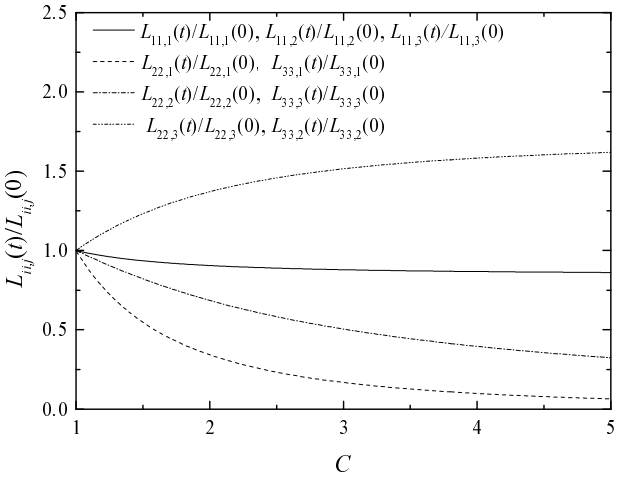

Figure 5.11: Changes in integral length scale in the inviscid RDT analysis.

The Taylor microscale $\lambda_{ii,j}$ is defined by

$$\lambda_{ii,j}(t) = \sqrt{\frac{\langle u_i^2 \rangle}{\left\langle \left(\frac{\partial u_i}{\partial x_j}\right)^2 \right\rangle}} = \sqrt{\frac{\int d\boldsymbol{\chi}\ \Phi_{ii}(\boldsymbol{\chi}, t)}{\int d\boldsymbol{\chi}\ \chi_j^2 \Phi_{ii}(\boldsymbol{\chi}, t)}} \text{ (no summation with respect to } i\text{)}. \tag{5.100}$$

When the isotropic initial conditions are considered, the square of the longitudinal Taylor microscale λ_f^2 is given by

$$\lambda_f^2 = 5\frac{\langle \boldsymbol{u}^2 \rangle}{\langle \boldsymbol{\omega}^2 \rangle}, \tag{5.101}$$

and the square of the lateral Taylor microscale is $\lambda_g^2 = \lambda_f^2/2$. The analytical solutions of the Taylor microscales are described in Appendix C. Figure 5.12 shows the changes in Taylor microscales for the initial homogeneous isotropic turbulence. As shown in figure 5.12, most Taylor microscales [e.g. $\lambda_{11,1}$, $\lambda_{22,2}$ $(= \lambda_{33,3})$, $\lambda_{22,1}$ $(= \lambda_{33,1})$ and $\lambda_{11,2}$ $(= \lambda_{11,3})$] decrease after the compression, whereas $\lambda_{22,3}$ $(= \lambda_{33,2})$ increases. Unlike the changes in the integral length scales, there is a difference between the changes in $\lambda_{11,1}$ and $\lambda_{22,1}$ $(= \lambda_{33,1})$. Regarding the length scales related to the parallel velocity components and the parallel direction, the reduction

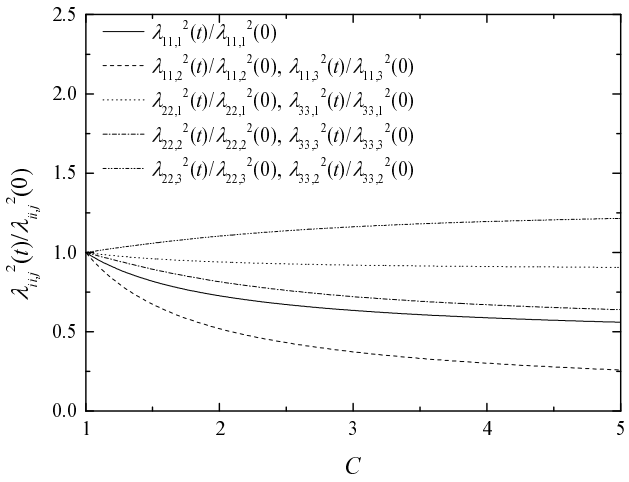

Figure 5.12: Changes in Taylor microscale in the inviscid RDT analysis.

of Taylor microscales is larger than that of the integral length scales. On the other hand, regarding the length scales related to the perpendicular components, the changes in the integral length scales are larger than those of the Taylor microscales.

To our knowledge, the issue of whether $L_{22,3}\,(= L_{33,2})$ and $\lambda_{22,3}\,(= \lambda_{33,2})$ are reduced or amplified has not been investigated in previous studies. In RDT analysis, these length scales are amplified after the compression. The other length scales are reduced after the compression. These results qualitatively agree with those of previous experiments (e.g. Agui *et al.* 2005) and DNSs (e.g. Lee *et al.* 1993; Hannappel & Friedrich 1995; Grube *et al.* 2011). The above-mentioned results are a part of the answer to the fourth question of Andreopoulos *et al.* (2000) related to the changes in the turbulent length scales. The changes in the dissipation length will be discussed later.

5.6 Results and Discussion for RDT analysis with non-zero viscosity

We investigated the changes in TKE dissipation and dissipation length scale using model spectra A ($Re_\lambda = 10^2$ and 10^4).

The non-zero viscous solutions take the form (Hanazaki & Hunt, 2004)

$$\hat{u}_i^s(\boldsymbol{\chi}, t) = D(t)\, \hat{u}_i^{s\ \mathrm{inv}}(\boldsymbol{\chi}, t), \tag{5.102}$$

where the superscript 'inv' denotes the inviscid solutions (5.30), (5.31) and (5.32). Here $D(t)$ is a function that satisfies

$$\left(\frac{d}{dt} + \nu(t)\chi^2\right) D(t) = 0. \tag{5.103}$$

With an initial condition $D(0) = 1$.

$$\begin{aligned} D(t) &= \exp\left(-\int_0^t ds\ \nu(s)\chi^2(s)\right) \\ &= \exp\left[-\frac{\nu_0}{S_1}\left[\frac{k_1^2}{n(1-\kappa)}\left((1+S_1 t)^{n(1-\kappa)} - 1\right)\right.\right. \\ &\quad \left.\left. + \frac{k_{23}^2}{n(1-\kappa)+2}\left((1+S_1 t)^{n(1-\kappa)+2} - 1\right)\right]\right]. \end{aligned} \tag{5.104}$$

Rapid shock-induced compression does not break the symmetry of the statistical quantities of turbulence, as shown in RDT analysis and as confirmed by DNS (Lee *et al.*, 1993, 1997). The energy spectral tensors with non-zero viscosity after the compression are expressed by

$$\Phi_\parallel(\boldsymbol{\chi}, t) = D^2(t)\, \Phi_\parallel^{\mathrm{inv}}(\boldsymbol{\chi}, t), \tag{5.105}$$

$$\Phi_\perp(\boldsymbol{\chi}, t) = D^2(t)\, \Phi_\perp^{\mathrm{inv}}(\boldsymbol{\chi}, t). \tag{5.106}$$

5.6.1 TKE dissipation rate

The ensemble averaged TKE dissipation rate in a homogeneous compressible flow can be decomposed into the solenoidal mode, ϵ^s, and the dilatational mode, ϵ^d (Bertoglio *et al.*, 2001),

$$\epsilon^s = \nu\left\langle \boldsymbol{\omega}^2 \right\rangle, \tag{5.107}$$

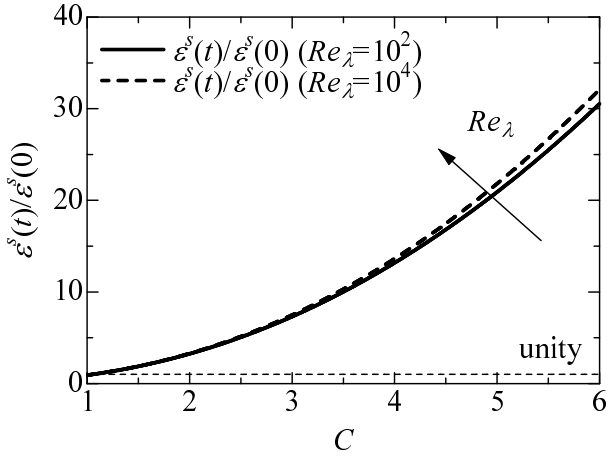

Figure 5.13: The amplification of TKE dissipation rate of the solenoidal mode.

$$\epsilon^d = \frac{4}{3}\nu \left\langle \left(\frac{\partial u_i^d}{\partial x_i} \right)^2 \right\rangle . \tag{5.108}$$

In weakly compressible homogeneous isotropic turbulence, Bertoglio *et al.* (2001) showed that ϵ^d is related to ϵ^s via $\epsilon^d = \alpha_1 M_t^2 \epsilon^s$, where $\alpha_1 \approx 0.5$. Thus, the evolution of the dilatational TKE dissipation rate is assumed to be weak for one-dimensional compression when the initial velocity fields consist only of the solenoidal mode.

Figure 5.13 shows the changes in the TKE dissipation rate of the solenoidal mode. After the compression, the TKE dissipation rate of the solenoidal mode is amplified and there is a slight Reynolds dependency. These results qualitatively agree with the experiments of Agui *et al.* (2005).

For the answer to the fifth question of Andreopoulos *et al.* (2000), the TKE dissipation rate of the solenodal mode is amplified after the compression. The TKE dissipation rate of the dilatational mode is also amplified after the compression because it is related to the amplification of the velocity fluctuation of the dilatational mode.

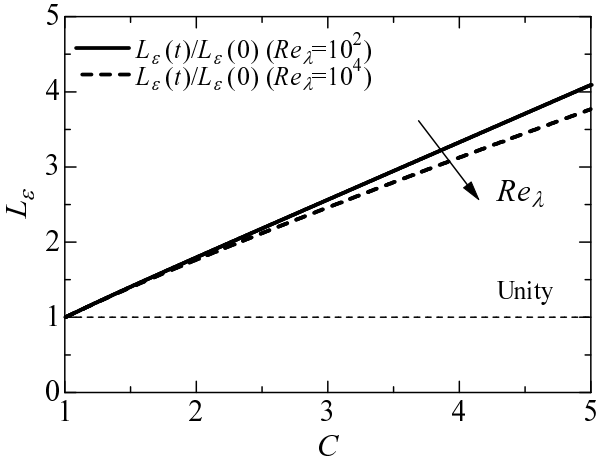

Figure 5.14: Changes in the dissipation scale.

5.6.2 Dissipation length scale

The dissipation length scale is defined by

$$L_\epsilon = \frac{K^{\frac{3}{2}}}{\epsilon}. \tag{5.109}$$

Figure 5.14 shows the changes in L_ϵ. L_ϵ is amplified after the compression, and there is a slight Reynolds number dependency. The obtained results qualitatively agree with the experiments of Honkan & Andreopoulos (1992) and the DNS of Lee *et al.* (1997); however, Hannappel & Friedrich (1995) showed the opposite results. Because the dissipation length scale is a ratio of the amplification of the TKE and the amplification of the TKE dissipation rate, the changes in L_ϵ may be related to both the initial strength of the turbulent Mach number and the initial Reynolds number.

5.7 Conclusions

The interactions between turbulence and a shock wave were analytically investigated by means of RDT analysis for initial homogeneous isotropic and axisymmetric turbulence.

We attempted to answer the questions identified by Andreopoulos *et al.* (2000) within the linear theoretical framework. The main results are as follows:

1. How much of the amplification of turbulence interacted with a shock wave is caused entirely by the Rankine–Hugoniot conditions?
   Because the obtained results in RDT are based on the Rankine-Hugoniot relation, the effect of shock-induced compression can be interpreted as a direct consequence of the Rankine-Hugoniot relation. Nonlinear effects may have appeared as an indirect consequence of the Rankine–Hugoniot relation via the perturbation manner. The convolution of the solenoidal modes are dominant when the initial solenoidal velocity fields are given. Although RDT analysis does not consider the baroclinic effects and curved shock effects, these effects are considered to be smaller than those of the shock-induced compression and nonlinear effects. Thus, the amplifications of TKE are caused primarily by the Rankine-Hugoniot relation.

2. Why are vorticity fluctuations amplified more than velocity fluctuations?
   The amplification of vorticity relates to changes in wavenumber and the amplification of energy at high wavenumbers. Because the enstrophy can be calculated from the integral $\frac{1}{2}\left\langle \boldsymbol{\omega}^2\left(t\right)\right\rangle = \frac{1}{2}\int d\boldsymbol{\chi}\ \Omega_{ii}\left(\boldsymbol{\chi},t\right)$, the integrand is given by $\Omega_{ii}\left(\boldsymbol{\chi},t\right) = \chi^2\Phi_{ii}\left(\boldsymbol{\chi},t\right)$, which can be approximated by $C^2k_1^2\Phi_{ii}\left(\boldsymbol{\chi},t\right)$ by neglecting the related term k_{23}^2. Thus, vorticity fluctuations are more amplified than velocity fluctuations with order $C^2\left(=\left(\overline{\rho}/\rho_0\right)^2\right)$.

3. Why is the energy of small eddies amplified more than that of large eddies?
   The amplification of energy at high wavenumbers is due to the extension of wavenumber. Then, the forms of energy spectra may be important. The main difference is seen in the region of the exponential form at high wavenumbers (unlike the power law form).

4. Are the length scales of the incoming turbulence reduced or amplified through such interactions?
   The integral length scales and the Taylor microscales are reduced for most cases. However, $L_{22,3}\left(=L_{33,2}\right)$ and $\lambda_{22,3}\left(=\lambda_{33,2}\right)$ are amplified. After the compression, the dissipation length scale is amplified and there is a slight

Reynolds number dependency. Because the dissipation length scales are the ratio of the amplification of TKE to the amplification of the TKE dissipation rate, the changes of dissipation length scale may be related to the initial strength of the turbulent Mach number and initial Reynolds number.

5. Is the TKE dissipation rate reduced?
   The TKE dissipation rate of the solenoidal mode is amplified after compression, and there is a slight Reynolds number dependency. Although kinematic viscosity is a decreasing function of $\overline{\rho}/\rho_0$, the increase in the enstrophy is larger than the decrease in the kinematic viscosity.

When the initial velocity fields are given by the homogeneous axisymmetric turbulence, the amplifications of the velocity and vorticity variances depend on both the initial degree of anisotropy and the angular distribution of the energy spectral tensor. The changes in parallel velocity variances depend on the energy distribution of the wave mode. Thus, different results are obtained between Ansatzes 1 and 2. Regardless of the initial energy spectra, the energies at high wavenumber are amplified more than those at low wavenumbers.

Finally, we summarize quantitative and qualitative comparison between the RDT and results of experiments and DNSs. The TKE is amplified after the interaction for RDT, experiments and DNSs. The r.m.s value of shock-induced compression direction increases and is qualitatively consistent with experiments including the present experiment and DNSs. As to the quantitative assessment, as the grid resolution increases, the changes in turbulence (e.g. TKE and vorticity variances) in DNSs (Grube *et al.*, 2011; Larsson *et al.*, 2013) become close to the RDT result. Then, the energy at high wavenumbers amplified , so that the increase in velocity fuctuation is caused by the increase in energy at high wavenumbers. This is qualitatively consistent with the present experiment, experiment of Barre *et al.* (1996) and DNS of Grube *et al.* (2011). However, needless to say, the detailed changes in turbulence is necessary since RDT is linear theory.

Chapter 6

Conclusions

Since the detailed conclusion is described in each chapter, this chapter summarizes briefly the main conclusions, assignments and the required future works.

Turbulence kinetic energy decay law and invariants in grid turbulence were discussed in chapter 3. The main results are as follows: For the moderate Reynolds numbers, grid turbulence behaves like Saffman turbulence, i.e. TKE exponent is close to Saffman's theoretical value 5/6 and the invariants $u_{r.m.s}^2 L_{uu}^3$ and $v_{r.m.s}^2 L_{vv}^3$ are constant for $x/M > 50$. There are no differences in the TKE decay exponents for different grid geometries. However, turbulence generated by cylindrical grids tends to develop fully at further distances than that generated by square grids. Then, $u_{r.m.s}^2 L_{uu}^5$ and $v_{r.m.s}^2 L_{vv}^5$, which correspond to Loitsianskii's integral, and $u_{r.m.s}^2 L_{uu}^2$ and $v_{r.m.s}^2 L_{vv}^2$, which correspond to the complete self-similarity of the energy spectrum, do not become constant at moderate Reynolds numbers. Sinhuber *et al.* (2015) conducted experiments of grid turbulence for higher Re_M and also argued that the TKE decay law is Saffman turbulence. However, their experiments were limited in the region $x/M \leq 30$. Thus, further experiments will be important, as mentioned by Djenidi *et al.* (2015).

Characteristics of divergence-free grid turbulence interacting with a shock wave was discussed in chapter 4. The originality is the present experiment is in the first experiment on the low-Mach number grid turbulence interacting with a shock wave. To the best of my knowledge, there is no study on the changes in divergence-free turbulence interacting with a shock wave. In the previous studies, the interaction with turbulence of $M_U \gg 0.3$ have been carried out

(Agui *et al.*, 2005). However, as pointed by Yoshizawa (1993), the changes in turbulence depend on the flow properties. Therefore, it is important to perform the interaction between a shock wave and divergence-free grid turbulence. The main results are as follows: The r.m.s value of the streamwise velocity fluctuations increases after the interaction and the streamwise integral length scale decreases after the interaction. Furthermore, the spectral analysis also shows that the energy at high wavenumbers increases after the interaction. As an important future work, the study on the interaction between divergence-free turbulence and a planar shock wave is necessary to deepen its mechanism.

In the present experiment as mentined in chapter 4, a spherical shock wave follows an expansion fan and therefore it is difficult to understand pure interaction between turbulence and a planar shock wave since there are additional effects on changes in turbulence due to the expansion fan. To begin with, there are a lot of open questions with regard to turbulence-shock wave interaction (Andreopoulos *et al.*, 2000). To deepen the mechanism of the interaction, the rapid distortion theory (RDT) analysis was carried out. The interactions between homogeneous turbulence and a planar shock wave were analytically investigated using rapid distortion theory (RDT) and were discussed in chapter 5. Here, I attempted to answer the questions identified by Andreopoulos *et al.* (2000) within the linear theoretical framework. The main results are as follows: TKE increases after the interaction and RDT results imply that its increase depends on the grid resolution. As the grid resolution increases, the changes in turbulence in DNSs (Grube *et al.*, 2011; Larsson *et al.*, 2013) become close to the RDT result. The effects of shock-induced compression can be interpreted as a direct consequence of the Rankine-Hugoniot relation because the obtained results in RDT are based on the Rankine-Hugoniot relation. Nonlinear effects may have appeared as an indirect consequence of the Rankine-Hugoniot relation via the perturbation manner. The results suggest that the amplification of TKE is caused primarily by the Rankine-Hugoniot relation. The vorticity fluctuations increase and its amplifications relate to changes in wavenumber and the amplification of energy at high wavenumbers. This is qualitatively consistent with the present experiment, experiment of Barre *et al.* (1996) and DNS of Grube *et al.* (2011). As to the changes in length scales,

the most length scales are reduced, but $L_{22,3}\,(= L_{33,2})$ and $\lambda_{22,3}\,(= \lambda_{33,2})$ are amplified. The TKE dissipation rate of the solenoidal mode is amplified and there is a slight Reynolds number dependency. For the initial axisymmetric turbulence, the amplifications of the velocity and vorticity variances depend on both the initial degree of anisotropy and the angular distribution of the energy spectral tensor. The analytical results qualitatively agree with the present experiments. Since RDT is based on a linear theory, the detailed changes in turbulence after the interaction should be carefully examined using DNS in the future.

Appendix A

Here, we describe how to solve ODEs. This calculation method is valid for almost all RDT equations (e.g. stratified turbulence, rotational turbulence, pure shear strain and axisymmetric strain) and for the first step for closures such as DIA families (e.g. weakly compressible homogeneous isotropic turbulence, stratified turbulence, low Re_m MHD turbulence and so on); however, this method is not valid for solving the dilatational mode RDT solution.

Using the eigenvalues, the transformation matrix $\boldsymbol{B}$ is given by

$$\boldsymbol{B} = \begin{bmatrix} 0 & \frac{k_{23}}{k_2}\imath & -\frac{k_{23}}{k_3}\imath \\ -\frac{k_3}{k_2} & 1 & \frac{k_2}{k_3} \\ 1 & \frac{k_3}{k_2} & 1 \end{bmatrix}, \tag{1}$$

and the determinant of $\boldsymbol{B}$ is given by

$$\mathrm{Det}\boldsymbol{B} = \frac{2k_{23}^3\imath}{k_2^2 k_3}. \tag{2}$$

The inverse transformation matrix is given by

$$\boldsymbol{B}^{-1} = \frac{1}{k_{23}} \begin{bmatrix} 0 & -\frac{k_2 k_3}{k_{23}} & \frac{k_2^2}{k_{23}} \\ -\frac{k_2}{2}\imath & \frac{k_2^2}{2k_{23}} & \frac{k_2 k_3}{2k_{23}} \\ \frac{k_3}{2}\imath & \frac{k_2 k_3}{2k_{23}} & \frac{k_3^2}{2k_{23}} \end{bmatrix}. \tag{3}$$

The diagonal matrix $\boldsymbol{D}$ consisting of the eigenvalues is given by

$$\boldsymbol{D} = \frac{S_1}{k_1^2 + k_{23}^2\left(1+S_1 t\right)^2} \begin{bmatrix} 0 & 0 & 0 \\ 0 & -k_{23}^2\left(1+S_1 t\right) + \imath k_1 k_{23} & 0 \\ 0 & 0 & -k_{23}^2\left(1+S_1 t\right) - \imath k_1 k_{23} \end{bmatrix}. \tag{4}$$

Because $\boldsymbol{B}^{-1}$ is not a function of t, after multiplying $\boldsymbol{B}^{-1}$ by (5.28) from the left side, one obtains

$$\frac{d}{dt}\underbrace{B_{\alpha i}^{-1}\hat{u}_i^s}_{y_\alpha} = B_{\alpha i}^{-1}A_{i\beta}\underbrace{B_{\beta\gamma}B_{\gamma j}^{-1}}_{\delta_{\beta j}}\hat{u}_j^s = D_{\alpha\gamma}\underbrace{B_{\gamma j}^{-1}\hat{u}_j^s}_{y_\gamma}. \tag{5}$$

For each component, we have

$$\frac{dy_1(\boldsymbol{\chi},t)}{dt} = 0, \tag{6}$$

$$\frac{dy_2(\boldsymbol{\chi},t)}{dt} = \frac{S_1}{k_1^2+k_{23}^2(1+S_1t)^2}\left(-k_{23}^2(1+S_1t)+\imath k_1k_{23}\right)y_2(\boldsymbol{\chi},t), \tag{7}$$

$$\frac{dy_3(\boldsymbol{\chi},t)}{dt} = \frac{S_1}{k_1^2+k_{23}^2(1+S_1t)^2}\left(-k_{23}^2(1+S_1t)-\imath k_1k_{23}\right)y_3(\boldsymbol{\chi},t). \tag{8}$$

The solution of $\boldsymbol{y}$ can be obtained after some algebra using the separation of variables:

$$\begin{bmatrix} y_1(\boldsymbol{\chi},t)\\ y_2(\boldsymbol{\chi},t)\\ y_3(\boldsymbol{\chi},t)\end{bmatrix} = \begin{bmatrix} y_1(\boldsymbol{k},0)\\ y_2(\boldsymbol{k},0)\frac{k_1^2+k_{23}^2(1+S_1t)+\imath k_1k_{23}S_1t}{k_1^2+k_{23}^2(1+S_1t)^2}\\ y_3(\boldsymbol{k},0)\frac{k_1^2+k_{23}^2(1+S_1t)+\imath k_1k_{23}S_1t}{k_1^2+k_{23}^2(1+S_1t)^2}\end{bmatrix}. \tag{9}$$

Initial components $\boldsymbol{y}(\boldsymbol{k},0)$ can be obtained via $\boldsymbol{y}(\boldsymbol{k},0) = \boldsymbol{B}^{-1}\hat{\boldsymbol{u}}^s(\boldsymbol{k},0)$, which are given by

$$\begin{bmatrix} y_1(\boldsymbol{k},0)\\ y_2(\boldsymbol{k},0)\\ y_3(\boldsymbol{k},0)\end{bmatrix} = \begin{bmatrix} -\frac{k_2k_3}{k_{23}^2}\hat{u}_2(\boldsymbol{k},0)+\frac{k_2^2}{k_{23}^2}\hat{u}_3(\boldsymbol{k},0)\\ -\frac{k_2\imath}{2k_{23}}\hat{u}_1(\boldsymbol{k},0)+\frac{k_2^2}{2k_{23}^2}\hat{u}_2(\boldsymbol{k},0)+\frac{k_2k_3}{2k_{23}^2}\hat{u}_3(\boldsymbol{k},0)\\ -\frac{k_3\imath}{2k_{23}}\hat{u}_1(\boldsymbol{k},0)+\frac{k_2k_3}{2k_{23}^2}\hat{u}_2(\boldsymbol{k},0)+\frac{k_3^2}{2k_{23}^2}\hat{u}_3(\boldsymbol{k},0)\end{bmatrix}. \tag{10}$$

From the relation $\hat{\boldsymbol{u}}^s(\boldsymbol{\chi},t) = \boldsymbol{B}\boldsymbol{y}(\boldsymbol{\chi},t)$, we obtain

$$\begin{aligned}\begin{bmatrix} \hat{u}_1^s(\boldsymbol{\chi},t)\\ \hat{u}_2^s(\boldsymbol{\chi},t)\\ \hat{u}_3^s(\boldsymbol{\chi},t)\end{bmatrix} &= \begin{bmatrix} P\hat{u}_1^s(\boldsymbol{k},0)-\frac{k_2Q}{k_{23}}\hat{u}_2^s(\boldsymbol{k},0)-\frac{k_3Q}{k_{23}}\hat{u}_3^s(\boldsymbol{k},0)\\ \frac{k_2Q}{k_{23}}\hat{u}_1^s(\boldsymbol{k},0)+\frac{k_3^2+k_2^2P}{k_{23}^2}\hat{u}_2^s(\boldsymbol{k},0)+\frac{k_2k_3}{k_{23}^2}(P-1)\hat{u}_3^s(\boldsymbol{k},0)\\ \frac{k_3Q}{k_{23}}\hat{u}_1^s(\boldsymbol{k},0)+\frac{k_2k_3}{k_{23}^2}(P-1)\hat{u}_2^s(\boldsymbol{k},0)+\frac{k_2^2+k_3^2P}{k_{23}^2}\hat{u}_3^s(\boldsymbol{k},0)\end{bmatrix}\\ &= \begin{bmatrix} \frac{k^2(1+S_1t)}{k_1^2+k_{23}^2(1+S_1t)^2}\hat{u}_1^s(\boldsymbol{k},0)\\ \frac{k_1k_2S_1t(2+S_1t)}{k_1^2+k_{23}^2(1+S_1t)^2}\hat{u}_1^s(\boldsymbol{k},0)+\hat{u}_2^s(\boldsymbol{k},0)\\ \frac{k_1k_2S_1t(2+S_1t)}{k_1^2+k_{23}^2(1+S_1t)^2}\hat{u}_1^s(\boldsymbol{k},0)+\hat{u}_3^s(\boldsymbol{k},0)\end{bmatrix},\end{aligned} \tag{11}$$

where P and Q are defined by (5.33) and (5.34), respectively.

Appendix B

The coefficients in (5.60)

$$\mathscr{R}_1 = \frac{1}{\pi}\mathrm{Fn}^{-2}\left(R_u, \beta\right) \tag{12}$$

$$\mathscr{R}_2 = \frac{\beta}{\pi}\mathrm{Fn}^{-2}\left(R_u, \beta\right) \tag{13}$$

$$\mathscr{B}_1 = \frac{1}{\pi^4}\left(-1 + \frac{2}{R_u}\right)\mathrm{Fn}^{-5}\left(R_u, \beta\right) \tag{14}$$

$$\mathscr{B}_2 = \frac{2\beta^{\frac{5}{2}}}{\pi^4}\left(1 - \frac{1}{R_u}\right)\mathrm{Fn}^{-5}\left(R_u, \beta\right) \tag{15}$$

where the function $\mathrm{Fn}\left(R_u, \beta\right)$ is

$$\mathrm{Fn}\left(R_u, \beta\right) = \left(-1 + \frac{2}{R_u}\right) + 2\beta^{\frac{1}{2}}\left(1 - \frac{1}{R_u}\right). \tag{16}$$

The coefficients in (5.63)

$$\mathscr{R}_1 = \frac{1}{\sqrt{\pi}}\frac{\Gamma\left(\frac{1}{3}\right)}{\Gamma\left(\frac{5}{6}\right)}\mathrm{Fn}^{-1}\left(R_u, \beta\right), \tag{17}$$

$$\mathscr{R}_2 = \sqrt{\frac{\beta}{\pi}}\frac{\Gamma\left(\frac{1}{3}\right)}{\Gamma\left(\frac{5}{6}\right)}\mathrm{Fn}^{-1}\left(R_u, \beta\right), \tag{18}$$

$$\mathscr{B}_1 = \frac{55}{36\pi^4}\frac{\Gamma^4\left(\frac{1}{3}\right)}{\Gamma^4\left(\frac{5}{6}\right)}\left(-1+\frac{2}{R_u}\right)\mathrm{Fn}^{-5}\left(R_u,\beta\right), \tag{19}$$

$$\mathscr{B}_2 = \frac{55\beta^{\frac{5}{2}}}{18\pi^4}\frac{\Gamma^4\left(\frac{1}{3}\right)}{\Gamma^4\left(\frac{5}{6}\right)}\left(1-\frac{1}{R_u}\right)\mathrm{Fn}^{-5}\left(R_u,\beta\right). \tag{20}$$

where $\Gamma\left(t\right)$ is the gamma function.

The coefficients in (5.67)

$$\mathscr{L}_0 = \frac{21^2}{\pi}\mathrm{Gn}^{-2}\left(R_u,\beta\right), \tag{21}$$

$$\mathscr{L}_2 = \frac{21^2\beta}{\pi}\mathrm{Gn}^{-2}\left(R_u,\beta\right), \tag{22}$$

$$\mathscr{F}_0 = \frac{21^4}{\pi^4}\left(17+\frac{4}{R_u}\right)\mathrm{Gn}^{-5}\left(R_u,\beta\right), \tag{23}$$

$$\mathscr{F}_2 = \frac{20\times 21^4\beta^{\frac{5}{2}}}{\pi^4}\left(\frac{1}{R_u}-1\right)\mathrm{Gn}^{-5}\left(R_u,\beta\right), \tag{24}$$

where the function $\mathrm{Gn}\left(R_u,\beta\right)$ is

$$\mathrm{Gn}\left(R_u,\beta\right) = 4\left(\frac{1}{R_u}+\frac{17}{4}\right)+10\beta^{\frac{1}{2}}\left(1-\frac{1}{R_u}\right). \tag{25}$$

Unlike Ansatz 1, one must pay attention to the values of β and R_u so as to satisfy the non–negative Hermitian form of $\Phi_{ij}\left(\boldsymbol{k}\right)$. In this study, we chose $\beta = 1$ for simplicity.

The coefficients in (5.68)

In the von Kármán type, the four coefficients are given by

$$\mathscr{L}_0 = \frac{21}{\sqrt{\pi}}\frac{\Gamma\left(\frac{1}{3}\right)}{\Gamma\left(\frac{5}{6}\right)}\mathrm{Gn}\left(R_u,\beta\right)^{-1}, \tag{26}$$

$$\mathscr{L}_2 = \frac{21\sqrt{\beta}}{\sqrt{\pi}} \frac{\Gamma\left(\frac{1}{3}\right)}{\Gamma\left(\frac{5}{6}\right)} \mathrm{Gn}\left(R_u, \beta\right)^{-1}, \tag{27}$$

$$\mathscr{F}_0 = \frac{1188495}{\pi^4} \frac{\Gamma^4\left(\frac{1}{3}\right)}{\Gamma^4\left(\frac{5}{6}\right)} \left(\frac{1}{R_u} + \frac{17}{4}\right) \mathrm{Gn}^{-5}\left(R_u, \beta\right), \tag{28}$$

$$\mathscr{F}_2 = \frac{1188495\beta^{\frac{5}{2}}}{\pi^4} \frac{\Gamma^4\left(\frac{1}{3}\right)}{\Gamma^4\left(\frac{5}{6}\right)} \left(\frac{5}{R_u} - 5\right) \mathrm{Gn}^{-5}\left(R_u, \beta\right). \tag{29}$$

Appendix C

Velocity variances

When the initial velocity fields are in homogeneous axisymmetric turbulence of Ansatz 1 (model spectrum B), the variances of perpendicular and parallel components, $\left\langle u_{\parallel}^2 \right\rangle$ and $\langle u_{\perp}^2 \rangle$, are given by

$$\left\langle u_{\parallel}^2 (t) \right\rangle = \frac{3\pi^{\frac{3}{2}}}{4} \left(\frac{\mathscr{B}_1}{\mathscr{R}_1^{\frac{5}{2}}} + \frac{\mathscr{B}_2}{\mathscr{R}_2^{\frac{5}{2}}} \right) \frac{C^3}{C^2-1} \left[1 + \left(C^2 - 2 \right) \frac{\tan^{-1}\sqrt{C^2-1}}{\sqrt{C^2-1}} \right], \tag{30}$$

$$\left\langle u_{\perp}^2 (t) \right\rangle = \frac{C\pi^{\frac{3}{2}}}{4} \left(\frac{3\mathscr{B}_1}{\mathscr{R}_1^{\frac{5}{2}}} + \frac{\mathscr{B}_2}{\mathscr{R}_2^{\frac{5}{2}}} \right) + \frac{3\pi^{\frac{3}{2}}}{8} \left(\frac{\mathscr{B}_1}{\mathscr{R}_1^{\frac{5}{2}}} + \frac{\mathscr{B}_2}{\mathscr{R}_2^{\frac{5}{2}}} \right) \frac{C^3}{C^2-1} \left[-1 + C^2 \frac{\tan^{-1}\sqrt{C^2-1}}{\sqrt{C^2-1}} \right], \tag{31}$$

and TKE is given by

$$K^s (t) = \frac{C\pi^{\frac{3}{2}}}{4} \left(\frac{3\mathscr{B}_1}{\mathscr{R}_1^{\frac{5}{2}}} + \frac{\mathscr{B}_2}{\mathscr{R}_2^{\frac{5}{2}}} \right) + \frac{3\pi^{\frac{3}{2}}}{4} \left(\frac{\mathscr{B}_1}{\mathscr{R}_1^{\frac{5}{2}}} + \frac{\mathscr{B}_2}{\mathscr{R}_2^{\frac{5}{2}}} \right) C^3 \frac{\tan^{-1}\sqrt{C^2-1}}{\sqrt{C^2-1}}. \tag{32}$$

When the initial velocity fields are in homogeneous axisymmetric turbulence for Ansatz 2 (model spectrum C), the variances of perpendicular and parallel velocity components, $\left\langle u_{\parallel}^2 \right\rangle$ and $\langle u_{\perp}^2 \rangle$, are given by

$$\begin{aligned} \left\langle u_{\parallel}^2 \right\rangle = {} & \frac{3\pi^{\frac{3}{2}}}{4} \frac{\mathscr{F}_0}{\mathscr{L}_0^{\frac{5}{2}}} \left[\frac{C^3}{C^2-1} + C^3 \frac{C^2-2}{C^2-1} \frac{\tan^{-1}\sqrt{C^2-1}}{\sqrt{C^2-1}} \right] \\ & + \frac{3\pi^{\frac{3}{2}}}{8} \frac{\mathscr{F}_2}{\mathscr{L}_2^{\frac{5}{2}}} \left[-C^3 \frac{C^2+8}{\left(C^2-1\right)^2} + C^3 \frac{5-C^2}{C^2-1} \frac{\tan^{-1}\sqrt{C^2-1}}{\sqrt{C^2-1}} \right. \\ & \left. + \frac{9C^3}{\left(C^2-1\right)^2} \frac{\tan^{-1}\sqrt{C^2-1}}{\sqrt{C^2-1}} \right], \end{aligned} \tag{33}$$

$$\left\langle u_{\perp}^{2}\right\rangle =\frac{3\pi^{\frac{3}{2}}}{8}\frac{\mathscr{F}_{0}}{\mathscr{L}_{0}^{\frac{5}{2}}}\left[\frac{C^{3}-2C}{C^{2}-1}+\frac{C^{5}}{C^{2}-1}\frac{\tan^{-1}\sqrt{C^{2}-1}}{\sqrt{C^{2}-1}}\right] +\frac{3\pi^{\frac{3}{2}}}{16}\frac{\mathscr{F}_{2}}{\mathscr{L}_{2}^{\frac{5}{2}}}\left[4C+\frac{7C^{5}+2C^{3}}{\left(C^{2}-1\right)^{2}}-\frac{C^{5}\left(C^{2}+8\right)}{\left(C^{2}-1\right)^{2}}\frac{\tan^{-1}\sqrt{C^{2}-1}}{\sqrt{C^{2}-1}}\right], \tag{34}$$

and TKE is given by

$$K^{s}\left(t\right)=\frac{3\pi^{\frac{3}{2}}}{4}\left(\frac{\mathscr{F}_{0}}{\mathscr{L}_{0}^{5}}+\frac{\mathscr{F}_{2}}{\mathscr{L}_{2}^{5}}\right)C+\frac{3\pi^{\frac{3}{2}}}{4}\frac{\mathscr{F}_{0}}{\mathscr{L}_{0}^{5}}C^{3}\frac{\tan^{-1}\sqrt{C^{2}-1}}{\sqrt{C^{2}-1}} +\frac{3\pi^{\frac{3}{2}}}{16}\frac{\mathscr{F}_{2}}{\mathscr{L}_{2}^{5}}\left(\frac{12C^{3}}{C^{2}-1}\frac{\tan^{-1}\sqrt{C^{2}-1}}{\sqrt{C^{2}-1}}-\frac{7C^{3}+5C}{C^{2}-1}\right). \tag{35}$$

Vorticity variances

When model spectrum B (the exponential form of Ansatz 1) is used as an initial condition, the variances of perpendicular and parallel vorticity are given by

$$\left\langle \omega_{\parallel}^{2}\left(t\right)\right\rangle =\left(\frac{5\pi^{\frac{3}{2}}}{2}\frac{\mathscr{B}_{1}}{\mathscr{R}_{1}^{\frac{7}{2}}}+\frac{5\pi^{\frac{3}{2}}}{4}\frac{\mathscr{B}_{2}}{\mathscr{R}_{2}^{\frac{7}{2}}}\right)C, \tag{36}$$

$$\left\langle \omega_{\perp}^{2}\left(t\right)\right\rangle =\frac{\pi^{\frac{3}{2}}C^{3}}{8}\left(\frac{5\mathscr{B}_{1}}{\mathscr{R}_{1}^{\frac{7}{2}}}+\frac{3\mathscr{B}_{2}}{\mathscr{R}_{2}^{\frac{7}{2}}}\right)+\frac{15\pi^{\frac{3}{2}}C^{3}}{8}\left(\frac{\mathscr{B}_{1}}{\mathscr{R}_{1}^{\frac{7}{2}}}+\frac{\mathscr{B}_{2}}{\mathscr{R}_{2}^{\frac{7}{2}}}\right), \tag{37}$$

and the enstrophy is given by

$$\left\langle \boldsymbol{\omega}^{2}\left(t\right)\right\rangle =5\pi^{\frac{3}{2}}\frac{\mathscr{B}_{1}}{\mathscr{R}_{1}^{\frac{7}{2}}}\left(C^{3}+\frac{C}{2}\right)+\frac{\pi^{\frac{3}{2}}}{2}\frac{\mathscr{B}_{2}}{\mathscr{R}_{2}^{\frac{7}{2}}}\left(9C^{3}+\frac{5}{2}C\right). \tag{38}$$

When model spectrum C (the exponential form of Ansatz 2) is used as an initial condition, the variances of perpendicular and parallel vorticity are given by

$$\left\langle \omega_{\parallel}^{2}\left(t\right)\right\rangle =\frac{5\pi^{\frac{3}{2}}C}{2}\left(\frac{\mathscr{F}_{0}}{\mathscr{L}_{0}^{\frac{7}{2}}}+\frac{\mathscr{F}_{2}}{\mathscr{L}_{2}^{\frac{7}{2}}}\right), \tag{39}$$

$$\left\langle \omega_{\perp}^{2}\left(t\right)\right\rangle =\frac{5\pi^{\frac{3}{2}}C^{3}}{2}\frac{\mathscr{F}_{0}}{\mathscr{L}_{0}^{\frac{7}{2}}}+\frac{5\pi^{\frac{3}{2}}C^{3}}{8}\frac{\mathscr{F}_{2}}{\mathscr{L}_{2}^{\frac{7}{2}}}, \tag{40}$$

and the enstrophy is given by

$$\left\langle \boldsymbol{\omega}^2(t) \right\rangle = 5\pi^{\frac{3}{2}} \left(C^3 + \frac{C}{2} \right) \frac{\mathscr{F}_0}{\mathscr{L}_0^{\frac{7}{2}}} + \frac{5\pi^{\frac{3}{2}}}{4} \left(C^3 + 2C \right) \frac{\mathscr{F}_2}{\mathscr{L}_2^{\frac{7}{2}}}. \tag{41}$$

Integral length scales

When the isotropic initial conditions are considered, from (5.44), (5.47), and (5.98), one-dimensional compressed integral length scales are given by

$$L_{\parallel,|}(t) = L_{11,1}(t) = \frac{4L_f(0)}{3} \frac{C^2 - 1}{C\left[1 + (C^2 - 2)\frac{\tan^{-1}\sqrt{C^2-1}}{\sqrt{C^2-1}}\right]}, \tag{42}$$

$$L_{\parallel,\perp}(t) = L_{11,2}(t) = L_{11,3}(t) = \frac{4L_g(0)}{3} \frac{C^2 - 1}{C\left[1 + (C^2 - 2)\frac{\tan^{-1}\sqrt{C^2-1}}{\sqrt{C^2-1}}\right]}, \tag{43}$$

$$\begin{aligned} L_{\perp\perp,\perp}(t) &= L_{22,2}(t) = L_{33,3}(t) \\ &= \frac{4L_f(0)}{3} \frac{1}{\left[1 + \frac{C^2}{2(C^2-1)}\left(-1 + C^2\frac{\tan^{-1}\sqrt{C^2-1}}{\sqrt{C^2-1}}\right)\right]}, \end{aligned} \tag{44}$$

$$L_{\perp\perp,|}(t) = L_{22,1}(t) = L_{33,1}(t) = \frac{4L_g(0)}{3} \frac{1}{C\left[1 + \frac{C^2}{2(C^2-1)}\frac{\tan^{-1}\sqrt{C^2-1}}{\sqrt{C^2-1}}\right]}, \tag{45}$$

$$L_{22,3}(t) = L_{33,2}(t) = \frac{4L_g(0)}{3} \frac{C}{1 + \frac{C^2}{2(C^2-1)}(-1 + C^2)\frac{\tan^{-1}\sqrt{C^2-1}}{\sqrt{C^2-1}}}. \tag{46}$$

Taylor microscales

When the isotropic initial conditions are considered, squared Taylor microscales after the compression are given by

$$\lambda^2_{\parallel,|}(t) = \lambda^2_{11,1}(t) = \frac{\lambda_f^2}{5} \frac{C^2 - 1}{C^2} \frac{1 + (C^2 - 2)\frac{\tan^{-1}\sqrt{C^2-1}}{\sqrt{C^2-1}}}{3\left(-1 + \frac{\tan^{-1}\sqrt{C^2-1}}{\sqrt{C^2-1}}\right) + \sqrt{C^2-1}\tan^{-1}\sqrt{C^2-1}}, \tag{47}$$

$$\lambda^2_{\parallel,\perp}(t) = \lambda^2_{11,2}(t) = \lambda^2_{11,3}(t) = \frac{4\lambda_g^2}{5}\left(C^2-1\right)\frac{1+\left(C^2-2\right)\frac{\tan^{-1}\sqrt{C^2-1}}{\sqrt{C^2-1}}}{C^2+2+C^2\left(C^2-4\right)\frac{\tan^{-1}\sqrt{C^2-1}}{\sqrt{C^2-1}}}, \tag{48}$$

$$\lambda^2_{\perp\perp,|}(t) = \lambda^2_{22,1}(t) = \lambda^2_{33,1}(t) = \frac{4\lambda_g^2}{5}\frac{1+\frac{C^2}{2(C^2-1)}\left(-1+C^2\frac{\tan^{-1}\sqrt{C^2-1}}{\sqrt{C^2-1}}\right)}{C^2\left[\frac{2}{3}+\frac{C^4}{\left(C^2-1\right)^2}\left(2+\frac{1}{C^2}-3\frac{\tan^{-1}\sqrt{C^2-1}}{\sqrt{C^2-1}}\right)\right]}, \tag{49}$$

$$\lambda^2_{\perp\perp,\perp}(t) = \lambda^2_{22,2}(t) = \lambda^2_{33,3}(t) = \frac{\lambda_f^2}{5}\frac{1+\frac{C^2}{2(C^2-1)}\left(-1+C^2\frac{\tan^{-1}\sqrt{C^2-1}}{\sqrt{C^2-1}}\right)}{\frac{1}{6}+\frac{3}{8}\frac{C^4}{\left(C^2-1\right)^2}\left[-3+\left(C^2+2\right)\frac{\tan^{-1}\sqrt{C^2-1}}{\sqrt{C^2-1}}\right]}, \tag{50}$$

$$\lambda^2_{22,3}(t) = \lambda^2_{33,2}(t) = \frac{2\lambda_g^2}{5}\frac{1+\frac{C^2}{2(C^2-1)}\left(-1+C^2\frac{\tan^{-1}\sqrt{C^2-1}}{\sqrt{C^2-1}}\right)}{\frac{1}{2}+\frac{1}{8}\frac{C^4}{\left(C^2-1\right)^2}\left[-3+\left(C^2+2\right)\frac{\tan^{-1}\sqrt{C^2-1}}{\sqrt{C^2-1}}\right]}. \tag{51}$$

References

Agui, J.H., Briassulis, G. & Andreopoulos, J. (2005). Studies of interactions of a propagating shock wave with decaying grid turbulence: velocity and vorticity fields. *J. Fluid Mech.*, **524**, 143–195. 3, 4, 67, 68, 72, 76, 79, 84, 99, 110, 114, 117, 119, 124

Andreopoulos, J., Agui, J.H. & Briassulis, G. (2000). Shock wave-turbulence interaction. *Annu. Rev. Fluid Mech.*, **524**, 309–345. 6, 7, 82, 83, 109, 113, 114, 117, 119, 121, 124

Antonia, R.A., Smalley, R.J., Zhou, T., Anselmet, F. & Danaila, L. (2003). Similarity of energy structure functions in decaying homogeneous isotropic turbulence. *J. Fluid Mech.*, **487**, 245–269. 2, 57

Antonia, R.A., Lee, S.K., Djenidi, L., Lavoie, P. & Danaila, L. (2013). Invariants for slightly heated decaying grid turbulence. *J. Fluid Mech.*, **727**, 379–406. 33

Armstrong, J.W., Rickett, B.J. & Spranger, S.R. (1995). Electro density power spectrum in the local interstellar medium. *Astrophys. J.*, **443**, 209–221. 14, 19, 81

Barre, S., Alem, D. & Bonnet, J.P. (1996). Experimental study of a normal shock/homogeneous turbulence interaction. *AIAA*, **34**, 968–974. 4, 72, 103, 114, 122, 124

Batchelor, G.K. (1946). The theory of axisymmetric turbulence. *Proc. Roy. Soc. Lond. A.*, **186**, 480–502. 91

Batchelor, G.K. (1948). Energy decay and self-preserving correlation functions in isotropic turbulence. *Quart. Appl. Math.*, **6**, 97–114. 27

Batchelor, G.K. (1949). The role of big eddies in homogeneous turbulence. *Proc. Roy. Soc. Lond. A*, **195**, 513–532. 26

Batchelor, G.K. (1953). *The theory of homogeneous turbulence*. Cambridge University Press. 2, 26, 28, 42, 91, 93, 115

Batchelor, G.K. (1967). *An introduction to Fluid Dynamics*. Cambridge University Press. 9

Batchelor, G.K. & Proudman, I. (1954). The effect of rapid distortion of a fluid in turbulent motion. *Quart. J. Mech. Appl. Math.*, **7**, 83–103. 23

Batchelor, G.K. & Proudman, I. (1956). The large-scale structure of homogeneous turbulence. *Phil. Trans. Roy. Soc. A*, **248**, 369–405. 17, 28, 31

Batchelor, G.K. & Townsend, A.A. (1948a). Decay of isotropic turbulence in the initial period. *Proc. Roy. Soc. Lond. A*, **193**, 539–558. 2

Batchelor, G.K. & Townsend, A.A. (1948b). Decay of turbulence in the final period. *Proc. Roy. Soc. Lond. A*, **194**, 527–543. 2, 32, 34

Bennett, J.C. & Corrsin, S. (1978). Small Reynolds number nearly isotropic turbulence in a straight duct and a contraction. *Phys. Fluids*, **21**, 2129–2140. 32, 34, 40

Bertoglio, J.P., Bataille, F. & Marion, J.D. (2001). Two–point closures for weakly compressible turbulence. *Phys. Fluids*, **13**, 290–310. 118, 119

Briassulis, G., Agui, J.H., Andreopoulos, J. & Watkins, C.B. (1996). A shock tube research facility for high-resolution measurements of compressible turbulence. *Expl. Therm. Fluid Sci.*, **13**, 430–446. 3, 76

Briassulis, G., Agui, J.H., Andreopoulos, J. & Watkins, C.B. (2001). The structure of weakly compressible grid-generated turbulence. *J. Fluid Mech.*, **432**, 219–283. 63

Burattini, P., Lavoie, P., Agrawal, A., Djenidi, L. & Antonia, R.A. (2006). Power law of decaying homogeneous isotropic turbulence at low Reynolds number. *Phys. Rev. E.*, **73**, 066304. 33

Cambon, C. & Teissèdre, C. (1985). Application des harmoniques sphériques à la représentation et au calcul des grandeurs cinématiques en turbulence homogène anisotrope. *C. R. Acad. Sci. Paris II*, **301**, 65–68. 95

Cambon, C., Mansour, N.N. & Godeferd, F.S. (1997). Energy transfer in rotating turbulence. *J. Fluid Mech.*, **337**, 303–332. 99

Chandrasekhar, S. (1950). The theory of axisymmetric turbulence. *Phil. Tran. Roy. Soc. Lond. A*, **242**, 557–577. 91

Chasnov, J.R. (1993). Computation of the loitsyansky integral in decaying isotropic turbulence. *Phys. Fluids.*, **5**, 2579–2587. 31

Comte-Bellot, G. & Corrsin, S. (1966). The use of a contraction to improve isotropy in grid-generated turbulence. *J. Fluid Mech.*, **25**, 657–682. 2, 29, 32, 40, 46

Craik, A.D.D. & Criminale, W.O. (1986). Evolution of wavelike disturbances in shear flows: a class of exact solutions of navier–stokes equations. *Proc. R. Soc. Lond. A.*, **406**, 13–26. 86

Davidson, P.A. (2004). *Turbulence: an introduction for scientists and engineers*. Oxford University Press. 2, 13, 18, 22, 26, 27, 94

Davidson, P.A. (2011). The minimum energy decay rate in quasi-isotropic grid turbulence. *Phys. Fluid*, **23**, 085108. 18, 27, 30, 31, 32, 33

Djenidi, L., Kamruzzaman, M. & Antonia, R.A. (2015). Power-law exponent in the transition period of decay in grid turbulence. *J. Fluid Mech.*, **779**, 544–555. 123

Donzis, D.A. (2012). Shock structure in shock-turbulence interactions. *Phys. Fluid*, **24**, 126101. 5

Dryden, H.L. (1943). A review of the statistical theory of turbulence. *Quart. Appl. Math.*, **1**, 7–42. 27, 32, 46

Durbin, P.A. & Pettersson Reif, B.A. (2010). *Statistical theory and modeling for turbulent flows*. Wiley. 23, 25

Durbin, P.A. & Zeman, O. (1992). Rapid distortion theory for homogeneous compressed turbulence with application to modelling. *J. Fluid Mech.*, **242**, 349–370. 24, 83

Frisch, U. (1995). *Turbulence: the legacy of AN Kolmogorov*. Cambridge university press. 19

Fung, J.C.H. (1990). *Kinematic simulation of turbulent flow and particle motions*. Ph.D. thesis, University of Cambridge. 23

Gad-El-Hak, M. & Corrsin, S. (1974). Measurements of the nearly isotropic turbulence behind a uniform jet grid. *J. Fluid Mech.*, **62**, 115–143. 28, 33, 34

George, W.K. (1992). The decay of homogeneous isotropic turbulence. *Phys. Fluids*, **4**, 1492–1509. 27, 32, 33

George, W.K. & Davidson, L. (2004). Role of initial conditions in establishing asymptotic flow behavior. *AIAA J.*, **42**, 438–446. 33

Grube, N.E., Taylor, E.M. & Martin, M.P. (2011). Numerical investigation of shock wave/isotropic turbulence interaction. In *49th AIAA Aerospace Sciences Meeting*. 5, 78, 84, 104, 105, 110, 112, 113, 117, 122, 124

Hanazaki, H. & Hunt, J.C.R. (1996). Linear processes in unsteady stably stratified turbulence. *J. Fluid. Mech.*, 303–337. 91

Hanazaki, H. & Hunt, J.C.R. (2004). Structure of unsteady stably stratified turbulence with mean shear. *J. Fluid. Mech.*, 1–42. 91, 118

Hannappel, R. & Friedrich, R. (1995). Direct numerical simulation of a Mach 2 shock interacting with isotropic turbulence. *Appl. Sci. Reas.*, **54**, 205–221. 4, 72, 117, 120

Hinze, J.O. (1959). *Turbulence*. McGraw-Hill Press. 2, 26, 36

Honkan, A. & Andreopoulos, J. (1992). Rapid compression of grid-generated turbulence by a moving shock wave. *Phys. Fluid*, **4**, 2562–2572. 3, 76, 79, 84, 114, 120

Huang, M.J. & Leonard, A. (1994). Power-law decay of homogeneous turbulence at low Reynolds numbers. *Phys. Fluids.*, **6**, 3765–3775. 33

Hunt, J.C.R. (1973). A theory of turbulent flow round two-dimensional bluff bodies. *J. Fluid Mech*, **61**, 625–706. 23

Hunt, J.C.R. & Carruthers, D.J. (1990). Rapid Distortion Theory and the 'problems' of turbulence. *J. Fluid Mech*, **212**, 497–532. 87

Hunt, J.C.R. & Kevlahan, N. (1993). Rapid distortion theory and the structure of turbulence. *New approaches and concepts in turbulence*, 285–316. 87

Iida, O., Iwatsuki, M. & Nagano, Y. (2000). Vortical turbulence structure and transport mechanism in a homogeneous shear flow. *Phys. Fluids*, **12**, 2895–2905. 23, 25

Ishida, T., Davidson, P.A. & Kaneda, Y. (2006). On the decay of isotropic turbulence. *J. Fluid Mech.*, **564**, 455–475. 2, 17, 27, 28

Ishihara, T., Kaneda, Y., Yokokawa, M., Itakura, K. & Uno, A. (2005). Energy spectrum in the near dissipation range of high resolution DNS of turbulence. *J. Phys. Soc. Jpn.*, **74**, 1464–1471. 22

Ishihara, T., Kaneda, Y., Yokokawa, M., Itakura, K. & Uno, A. (2007). Small-scale statistics in high-resolution direct numerical simulation of turbulence: Reynolds number dependence of one-point velocity gradient statistics. *J. Fluid Mech.*, **592**, 335–366. 44

Jacquin, L., Cambon, C. & Blin, E. (1993). Turbulence amplification by a shock wave and Rapid Distortion Theory. *Phys. Fluid*, **5**, 2539–2550. 6, 78, 91, 103, 104, 105, 109

KANEDA, Y. (1981). Renormalized expansions in the theory of turbulence with the use of Lagrangian position function. *J. Fluid Mech.*, **107**, 131–145. 19

KANEDA, Y., ISHIHARA, M., T.AND YOKOKAWA, ITAKURA, K. & UNO, A. (2003). Energy dissipation rate and energy spectrum in high resolution direct numerical simulations of turbulence in a periodic box. *Phys. Fluids*, **15**, 21–24. 2, 17, 47, 53, 54

KANG, H.S., CHESTER, S. & MENEVEAU, C. (2003). Decaying turbulence in an active-grid-generated flow and comparisons with large-eddy simulation. *J. Fluid Mech.*, **480**, 129–160. 33

KARMAN, T.V. & HOWARTH, L. (1938). On the statistical theory of isotropic turbulence. *Proc. Roy. Soc. Lond. A*, **164**, 192–215. 11, 16

KARMAN, T.V. & LIN, C.C. (1949). On the concept of similiarity in the theory of isotropic turbulence. *Rev. Mod. Phys.*, **21**, 516–519. 27

KELLER, J. & MERZKIRCH, W. (1990). Interaction of a normal shock wave with a compressible turbulent flow. *Exps. Fluid.*, **8**, 241–248. 3, 67, 72

KEVLAHAN, N.K.R. (1997). The vorticity jump across a shock in a non–uniform flow. *J. Fluid. Mech.*, **341**, 371–384. 88, 91

KEVLAHAN, N.K.R. & HUNT, J.C.R. (1997). Nonlinear interactions in turbulence with strong irrotational straining. *J. Fluid. Mech.*, **337**, 333–364. 87, 88, 105

KIDA, S. & YANASE, S. (1999). *Turbulence Dynamics*. Asakura Shoten, Tokyo. 24

KOLMOGOROV, A.N. (1941a). Dissipation of energy in the locally isotropic turbulence. *Dokl. Akad. Nauk. SSSR*, **32**, 15–17. 2, 19

KOLMOGOROV, A.N. (1941b). The local structure of turbulence in incompressible viscous fluid for very large Reynolds numbers. *Dokl. Akad. Nauk. SSSR*, **31**, 301–305. 2, 19, 20

Kolmogorov, A.N. (1941c). On the degeneration of isotropic turbulence in an incompressible viscous fluid. *Dokl. Akad. Nauk. SSSR*, **31**, 538–540. 16, 32

Korneyev, A.I. & Sedov, L.I. (1976). Theory of isotropic turbulence and its comparison with experimental data. *Fluid Mech. Sev. Res.*, **5**, 37–47. 27

Krogstad, P.Å. & Davidson, P.A. (2010). Is grid turbulence Saffman turbulence? *J. Fluid Mech.*, **642**, 373–394. 6, 28, 29, 30, 32, 39, 42, 43, 45, 46, 48, 49, 52, 53, 54, 55, 58, 61

Landau, L.D. & Lifshitz, E.M. (1959). *Fluid Mechanics*. Cambridge: 1st Ed. Pergamon Press. 16, 17

Larsson, J. & Lele, S.K. (2009). Direct numerical simulation of canonical shock/turbulence interaction. *Phys. Fluids*, **21**, 126101. 5, 84, 102, 103, 104, 110, 112, 113

Larsson, J., Bermejo-Moreno, I. & Lele, S.K. (2013). Reynolds– and Mach–number effects in canonical shock–turbulence interaction. *J. Fluid Mech.*, **717**, 293–321. 5, 75, 79, 103, 104, 105, 106, 112, 113, 122, 124

Lavoie, P., Burattini, P., Djenidi, L. & Antonia, R.A. (2005). Effects of initial conditions on decaying grid turbulence at low R_λ. *Exps. Fluids*, **39**, 865–874. 42

Lavoie, P., Djenidi, L. & Antonia, R.A. (2007). Effects of initial conditions in decaying turbulence generated by passive grids. *J. Fluid Mech.*, **585**, 395–420. 2, 29, 32, 34, 39, 40, 42, 43, 45, 46, 47

Lee, L., Lele, S.K. & Moin, P. (1993). Direct numerical simulation of isotropic turbulence interacting with a weak shock wave. *J. Fluid Mech.*, **251**, 533–562. 4, 5, 72, 84, 110, 117, 118

Lee, L., Lele, S.K. & Moin, P. (1997). Interaction of isotropic turbulence with shock wave: effect of shock strength. *J. Fluid Mech.*, **340**, 225–247. 5, 103, 104, 110, 118, 120

Lee, M.J., Kim, J. & Moin, P. (1990). Structure of turbulence at high shear rate. *J. Fluid Mech.*, **216**, 561–583. 23, 24

Lesieur, M. (2008). *Turbulence in Fluids*. Cambridge: 4th Ed. Springer. 26

Lesieur, M. & Ossia, S. (2000). 3D isotropic turbulence at very high Reynolds numbers: EDQNM study. *J. Turbulence*, **1**, 1–25. 27, 28, 32

Lesieur, M. & Schertzer, D. (1978). Self similar decay of high Reynolds number turbulence. *J. de Mecanique*, **17**, 609–646. 17

Leslie, D.C. (1973). *Developments in the theory of turbulence*. Oxford University Press. 19

Liang, S.M., Hsu, J.L. & Wang, J.S. (2001). Numerical study of cylindrical blast wave propagation and reflection. *AIAA J.*, **39**, 1152–1158. 66

Loitsianskii, L.G. (1939). Some basic laws of isotropic turbulent flow. *Rep. Cent. Aero Hydrodyn. Inst.(Moscow)*, **1079**, 1–36. 16, 17

Lundgren, J.L. (1982). Strained spiral vortex model for turbulent fine structure. *Phys. Fluids.*, **25**, 2193–2203. 22

Mahesh, K., Lele, S.K. & Moin, P. (1994). The response of anisotropic turbulence to Rapid homogeneous one-dimensional compression. *Phys. Fluid*, **6**, 1052–1062. 6, 89

Mahesh, K., Lele, S.K. & Moin, P. (1997). The influence of entropy fluctuations on the interaction of turbulence with a shock wave. *J. Fluid Mech.*, **84**, 497–516. 5, 103

Makita, H. (1991). Realization of a large-scale turbulence field in a small wind tunnel. *Fluid Dyn. Res.*, **8**, 53–64. 2, 33

Marion, J.D., Bertoglio, J.P. & Mathieu, J. (1988). Spectral study of weakly compressible isotropic turbulence: Part i: Direct interaction approximation. *C. R. Acad. Sci. Paris, Serie II*, **307**, 1487–1492. 83, 86, 91

Matsumoto, A., Nagano, Y. & Tsuji, T. (1994). Effects of mean shear on homogeneous turbulence. *Trans. JSME*, **60**, 1653–1660. 23, 24

McComb, W.D. (1989). *The Physics of Fluid Turbulence*. Clarendon Press. 19

McComb, W.D. (2014). *Homogeneous, Isotropic turbulence*. Oxford Press. 19

Miville-Deschenes, M.A., Joncas, G., Falgarone, E. & Boulanger, F. (2003). High resolution 21 cm mapping of the Ursa Major Galatic cirrus: power spectra of the high–latitude Hi gas. *Astron. Astrophys.*, **411**, 109–121. 81

Mohamedo, M.H. & LaRue, H.C. (1990). The decay power law in grid-generated turbulence. *J. Fluid Mech*, **219**, 195–214. 2, 29, 33, 40, 46

Monin, A.S. & Yaglom, A.M. (1975). *Statistical Fluid Mechanics*. Vol. II MIT Press, Cambridge. 26, 29

Mydlarski, L. & Warhaft, Z. (1996). On the onset of high-Reynolds-number grid-generated wind tunnel turbulence. *J. Fluid Mech*, **320**, 331–368. 2, 33

Nagata, K., Wong, H., Hunt, J.C.R., Sajjadi, S.G. & Davidson, P.A. (2006). Weak mean flows induced by anisotropic turbulence impinging onto planar and undulating surfaces. *J. Fluid Mech.*, **556**, 329–360. 96, 97

Nagata, K., Hunt, J.C.R., Sakai, Y. & Wong, H. (2011). Distorted turbulence and secondary flow near right-angled plates. *J. Fluid Mech.*, **668**, 446–479. 23, 34

Nastrom, G.D. & Gage, K.S. (1985). A climatology of atmospheric wavenumber spectra of wind and temperature observed by commercial aircraft. *J. Atmos. Sci.*, **42**, 950–960. 14

Obukhov, A.M. (1941). On the distribution of energy in the spectrum of turbulent flow. *Dokl. Akad. Nauk. SSSR*, **32**, 22–24. 19

Pao, Y.H. (1965). Structure of turbulent velocity and scalar fields at large wavenumbers. *Phys. Fluids*, **8**, 1063–1075. 22

Pearson, B.R., Krogstad, P.Å. & Van de Water, W. (2002). Measurements of the turbulent energy dissipation rate. *Phys. Fluids*, **14**, 1288–1290. 17

Proudman, I. & Reid, W.H. (1954). On the decay of a normally distributed and homogeneous turbulent velocity field. *Phil. Trans. Roy. Soc. Lond. A*, **247**, 163–189. 17

Ribner, H.S. & Tucker, M. (1953). Spectrum of turbulence in a contracting stream. *NACA Rept.*, **1113**. 102

Robertson., H.P. (1940). The invariant theory of isotropic turbulence. *Math. Proc. Phil. Soc.*, **30**, 209–223. 11

Saffman, P.G. (1967). The large-scale structure of homogeneous turbulence. *J. Fluid Mech.*, **27**, 581–593. 18, 26, 27, 28, 32, 61

Sagaut, P. & Cambon, C. (2008). *Homogeneous Turbulence Dynamics*. Cambridge Univ Press. 2, 5, 22, 23, 25, 26, 49, 99

Sasoh, A., Harasaki, T., Kitamura, T., Takagi, T., Ito, S., Matsuda, A., Nagata, K. & Sakai, Y. (2014). Statistical behavior of post–shock overpressure past grid turbulence. *Shock Waves*, **24**, 489–500. 34, 64, 68

Schedvin, G.R., Stegen, G.R. & Gibson, C.H. (1974). Universal similarity at high grid Reynolds number. *J. Fluid Mech.*, **65**, 561–579. 28, 32

Shin, S. & Nakano, K. (2005). *The illustrated wavelet transform handbook*. Asakura shoten, Tokyo. 75

Simmons, L. & Salter, C. (1934). Experimental investigation and analysis of the velocity variations in turbulent flow. *Proc. Trans. Roy. Soc. A*, **145**, 212–234. 2

Sinhuber, M., Bodenschatz, E. & Bewley, G.P. (2015). Decay of turbulence at high Reynolds numbers. *Phys. Rev. Lett.*, **114**, 034501. 123

Speziale, C.G. & Bernard, P.S. (1992). The energy decay in self-preserving isotropic turbulence revisited. *J. Fluid Mech.*, **241**, 645–667. 27, 46

Sreenivasan, K.R. (1984). On the scaling of the turbulence energy dissipation rate. *Phys. Fluid*, **27**, 1048–1051. 47, 52, 54

Sreenivasan, K.R. (1995). On the universality of the Kolmogorov constant. *Phys. Fluids*, **7**, 2778–2784. 53

Sreenivasan, K.R. & Antonia, R.A. (1997). The phenomenology of small-scale turbulence. *Annu. Rev. Fluid Mech.*, **29**, 435–472. 38, 44, 45

Sreenivasan, K.R. & Narasimha, R. (1978). Rapid distortion of axisymmetric turbulence. *J. Fluid Mech.*, **84**, 497–516. 95, 96

Taylor, G.I. (1935). Statistical theory of turbulence. *Proc. Trans. Roy. Soc. A*, **151**, 421–444. 2, 47

Townsend, A.A. (1951). On the fine-scale structure of turbulence. *Proc. Roy. Soc. Lond. A.*, **208**, 534–542. 22

Townsend, A.A. (1976). *Homogeneous Shear Flow*. Cambridge Univ Press. 23, 25

Townsend, A.A. (1980). The response of sheared turbulence to additional distortion. *J. Fluid Mech.*, **98**, 171–191. 23

Wang, J., Shi, Y., Wang, L.P., Xiao, Z., He, X.T. & Chen, S. (2012). Effect of compressibility on the small–scale structures in isotropic turbulence. *J. Fluid Mech.*, **713**, 588–631. 64

Yoshizawa, A. (1993). Turbulence modeling and compressibility. *J. Jap. Soc. Aero. & Space Sci.*, **41**, 116–123. 4, 124